MAGNETOM Flash

Special Pediatric Edition · 9/2019

siemens.com/magnetom-world

SIEMENS Healthineers

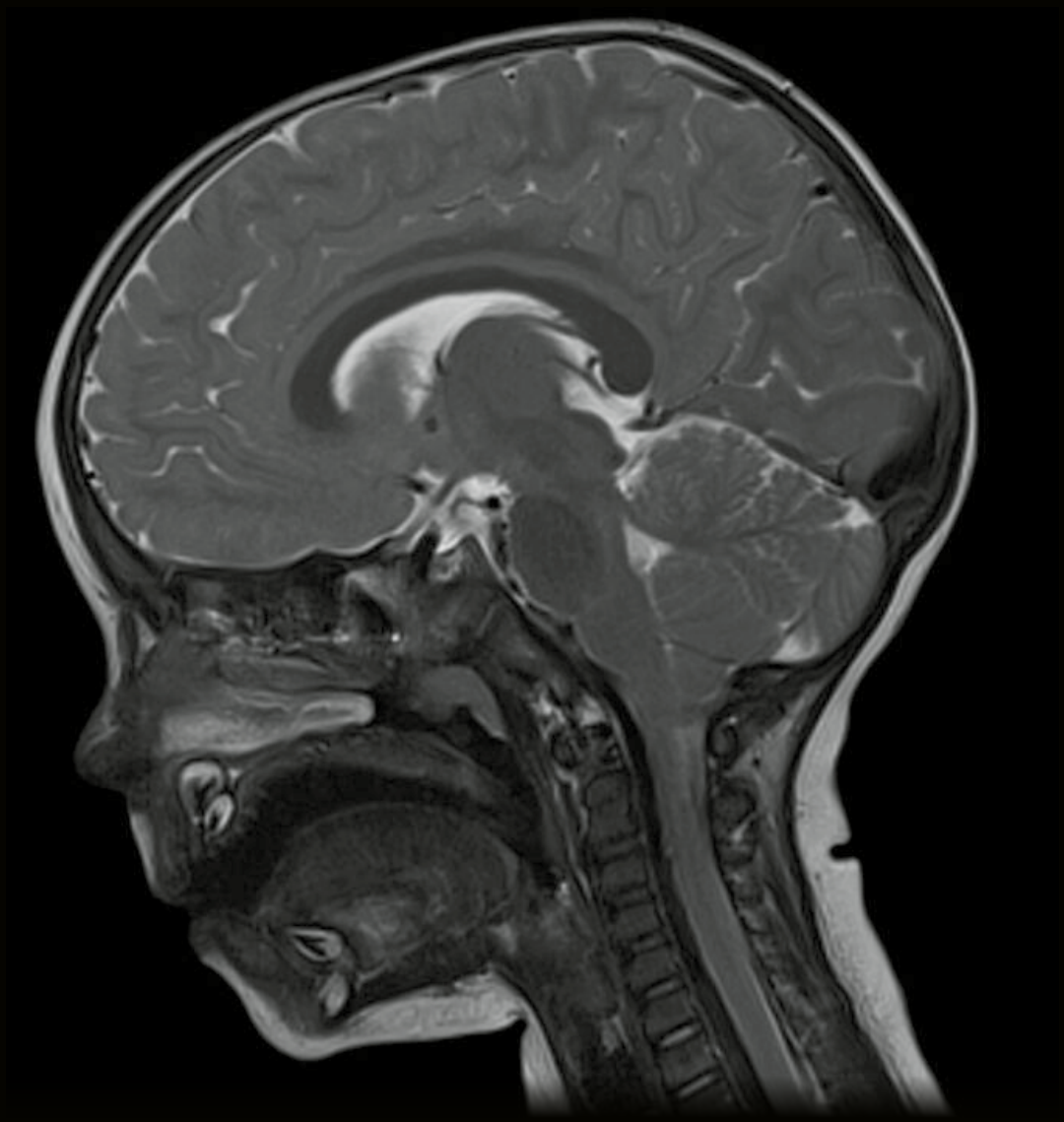

Special Pediatric Edition

MR imaging of children[1] can be challenging. Different disease types, physiology and behavior all can have a direct impact on image quality. Our youngest patients can also be our most vulnerable. Siemens trendsetting solutions can help overcome these challenges to enable high-quality diagnostic imaging of all body regions in a child-friendly environment. This special edition of the Pediatric MAGNETOM Flash addresses various techniques to reduce sedation, overcoming the difficulty of imaging smaller patients and experiences with applications to decrease exam times. The magazine is compiled of relevant pediatric topics and imaging challenges that span across the globe.

[1]The safety of imaging infants under two years of age has not been established. The responsible physician must evaluate the benefits of the MR examination compared to those of other imaging procedures.

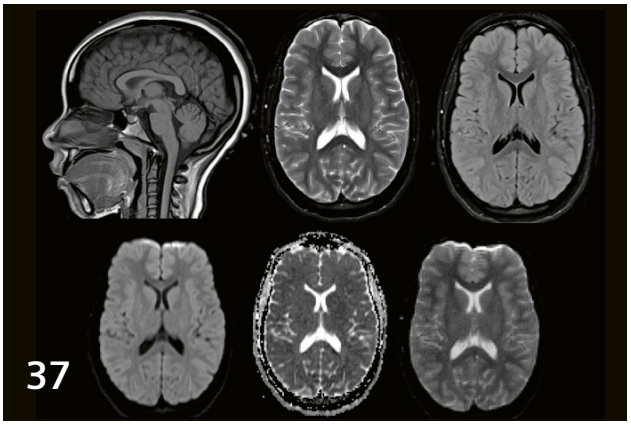

GOBrain 5-Minute MRI in children:
Reducing the need for sedation

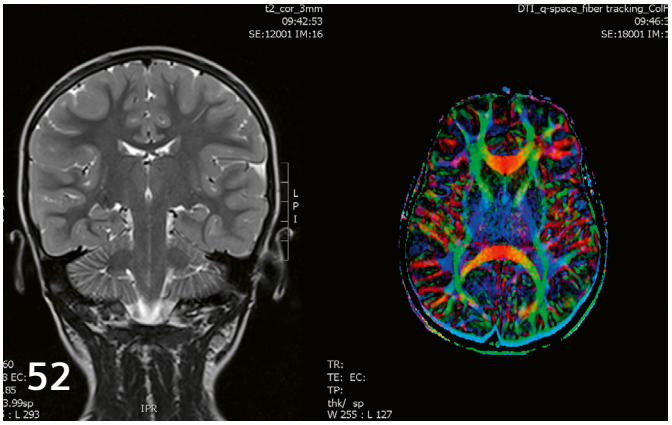

Robust, Efficient, and Comprehensive Pediatric Imaging with BioMatrix Technology and High-End Applications

Special Pediatric Edition

[1]MR scanning has not been established as safe for imaging fetuses and infants less than two years of age. The responsible physician must evaluate the benefits of the MR examination compared to those of other imaging procedures.
[2]Work in progress: the application is currently under development and is not for sale in the US and in other countries. Its future availability cannot be ensured.
[3]syngo.via Frontier is for research only, not a medical device. syngo.via Frontier MR Total Tumor Load is a released research prototype.
[4]syngo Virtual Cockpit is not commercially available in all countries. For regulatory reasons, its future availability cannot be guaranteed. Precondition: Expert-i enabled modality from Siemens Healthineers.

We appreciate your comments.
Please contact us at magnetomworld.team@siemens-healthineers.com

Editorial Board

Review Board

We are looking forward to hearing from you

Founded in 1993 the MAGNETOM Flash magazine has been around almost as long as MAGNETOM MRI scanners.

In times of online media and digitalization we would value your feedback to ensure that the magazine continues to fit your interests and professional needs.

Please take a moment to complete a brief reader survey at
www.siemens.com/magnetom-world

53-18-13339-01-76

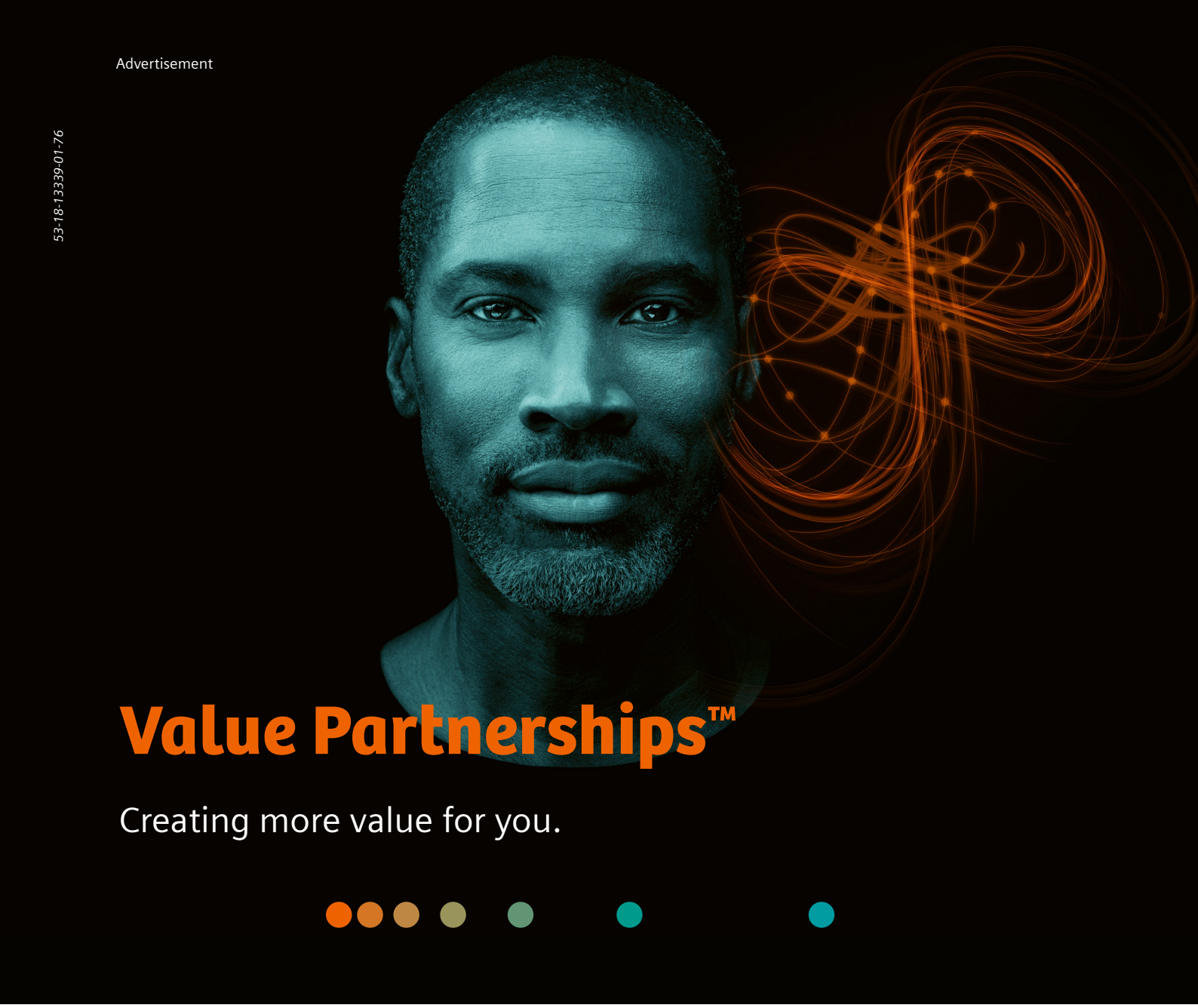

Value Partnerships™

Creating more value for you.

Value Partnerships™ from Siemens Healthineers are enduring, performance-oriented relationships. Our innovative business models help you increase enterprise-wide value in order to meet both your immediate and your future goals. Within the context of a modern, digitally enabled health system, we help you identify and activate three key main engines:

Optimize: enhance processes, streamline operations, and improve patient experience

Expand: add new capabilities and scale up existing ones to transform care delivery while maintaining quality and profitability

Advance: elevate the quality and precision of care delivery by advancing the level of innovation in your organization

Value Partnerships™ optimize care delivery to create more value for you.

siemens-healthineers.com/value-partnerships

SIEMENS Healthineers

Advanced Multi-Parametric Neuroimaging in Pediatric Neurology

Arun Joseph[1]; Steffi Dreha-Kulaczewski[2,3]

[1]Biomedizinische NMR, Max-Planck-Institut für biophysikalische Chemie, Göttingen, Germany
[2]Department of Pediatrics and Adolescent Medicine, Division of Pediatric Neurology, University Medical Center Göttingen, Germany
[3]Department of Cognitive Neurology, MR-Research in Neurology and Psychiatry, University Medical Center Göttingen, Germany

Introduction

MR imaging and spectroscopy play important roles in the management of our neuropediatric patients. While structural assessments of the central nervous system by conventional MRI constitute an essential part of clinical routine, recent technical advances have facilitated insights not only into brain structures but also into function and metabolism as well as into the dynamics of cerebrospinal fluid (CSF) and aspects of myelination as an indicator of brain maturation. Many of these techniques contribute to faster diagnosis and, even more importantly, to evaluation of therapies, e.g., in neurometabolic disorders. Furthermore, novel methods like real-time phase-contrast (PC) flow MRI will be of great importance in unravelling the pathophysiological mechanisms in pediatric patients with disturbed CSF circulation like hydrocephalus, pseudotumor cerebri, as well as spinal cord disorders such as syringomyelia. Pertinent insights promise a basis for new approaches to therapeutic interventions.

^{1}H-MR spectroscopy for diagnostics and therapy monitoring

MRS characterizes brain cellular composition and metabolism and thus offers complementary information to structural MRI. For example, tissue-specific placements of volumes-of-interests may help to differentiate between gray-matter (GM) and white-matter (WM) diseases. The

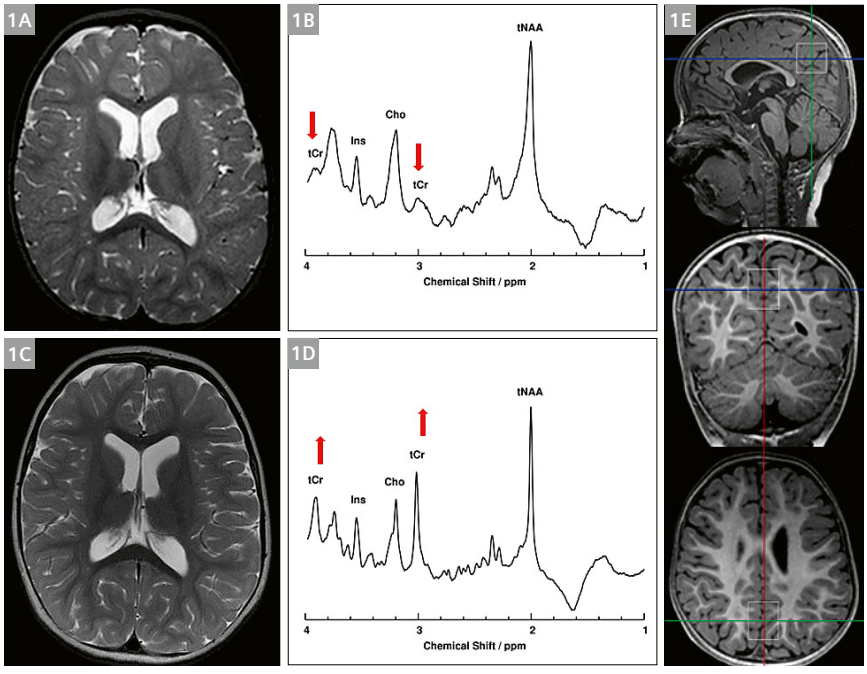

1 **^{1}H-MR spectroscopy in a girl with creatine deficiency syndrome** (caused by guanidinoacetate methyltransferase deficiency).

(1A, B) (Age 1.3 years[1]): (1A) axial T2-weighted image without abnormalities. Myelination is appropriate for the age. (1B) Gray matter (GM) spectrum reveals two significantly reduced tCr peaks indicating cerebral creatine deficiency.

(1C, D) After three months of creatine and ornithine supplementation (age 1.6 years): (1C) Axial T2-weighted image demonstrates physiological advancement of myelination. (1D) tCr peaks have increased, reflecting effective therapy. (1E) Voxel placement in posterior paramedian GM.

tNAA: *N*-acetylaspartate and *N*-acetylaspartylglutamate
tCr: creatine and phosphocreatine
Cho: choline-containing compounds
Ins: *myo*-inositol
ppm: parts per million

neuronal marker *N*-acetylaspartate (NAA) dominates a pediatric brain spectrum from about five months of age and is of significant clinical relevance. Other metabolites accessible by MRS are creatine (Cr), which reflects energy metabolism, choline-containing compounds (Cho) depicting membrane turnover, and *myo*-inositol (Ins) as an astrocytic marker [1]. Postnatal brain development and maturation processes (e.g., myelination) result in considerable biochemical changes and correspondingly altered metabolite patterns [2]. Such knowledge allows for the evaluation of normal and pathological brain development and is one essential feature in pediatric applications. Insights into the "*in vivo* biochemistry" of the brain by MRS may greatly facilitate the diagnostic work-up of patients with neurometabolic or WM diseases, neurodegeneration, or brain tumors. In general, only very few metabolite patterns in a MR spectrum unequivocally point toward a specific diagnosis and hence obviate the need for further diagnostic procedures except for appropriate genetic tests. Prominent examples are the appearance of succinate (2.4 ppm) in succinate dehydrogenase deficiency [3], of succinyladenosine (8.3 ppm) in adenylosuccinate lyase deficiency [4], or the absence of Cr in creatine deficiency syndromes (Fig. 1) [5, 6]. In cases where specific MRS results precede genetic or biochemical confirmation, decisions about therapies can be made earlier in the process. More commonly, MRS patterns reflect general pathophysiologic processes like neurodegeneration (decrease in NAA), astrocytosis (elevation of Ins), hypomyelination (decrease in Cho) or demyelination (increase in Cho). Detection of lactate (doublet at 1.3 ppm) facilitates the diagnosis of a mitochondriopathy and supports the clinical management of those patients (Fig. 2).

In our understanding, MRS techniques will be of increasing relevance for the evaluation and monitoring of future therapies. To date, the effective supplementation of creatine and ornithine in the treatment of a creatine deficiency is monitored by a rise in the intracerebral Cr concentration as measured by MRS (Fig. 1). Sufficient substitution of folinic acid normalizes perturbed brain metabolism in cerebral folate deficiency, which can also be monitored by MRS, as shown in Figure 3 [7].

^{1}H-MR spectroscopy protocol

Our routine MRS protocol is well established and easy to handle in order to allow for comparable and reliable follow-up studies. Currently, we use a 3T MAGNETOM Prisma^{fit} for our patient measurements and a 64-channel receive array. Sometimes we utilize the 20-channel head coil, depending on patient condition. Fully relaxed ^{1}H MR spectra (64 accumulations) are almost consistently acquired using a single-voxel STEAM (stimulated echo acquisition mode) localization sequence with TR/TE/TM = 6000/20/10 ms [8]. Short TE ensures access to a large number of metabolites. Voxel sizes range between 4.1 mL in WM and 12 mL in GM and are routinely placed within frontal or parieto-occipital WM, posterior paramedian GM, basal ganglia and thalamus, or cover a structural lesion. Usually, a manual shim further improves the homogeneity achieved by automated shimming. Absolute concentrations of *N*-acetylaspartate and *N*-acetylaspartylglutamate (tNAA) at 2.01 ppm, creatine and phosphocreatine (tCr) at 3.02 and 3.93 ppm, Cho at 3.22 ppm, Ins at 3.35 ppm, and lactate are determined by LCModel [9] and compared with age-matched controls from our own data base.

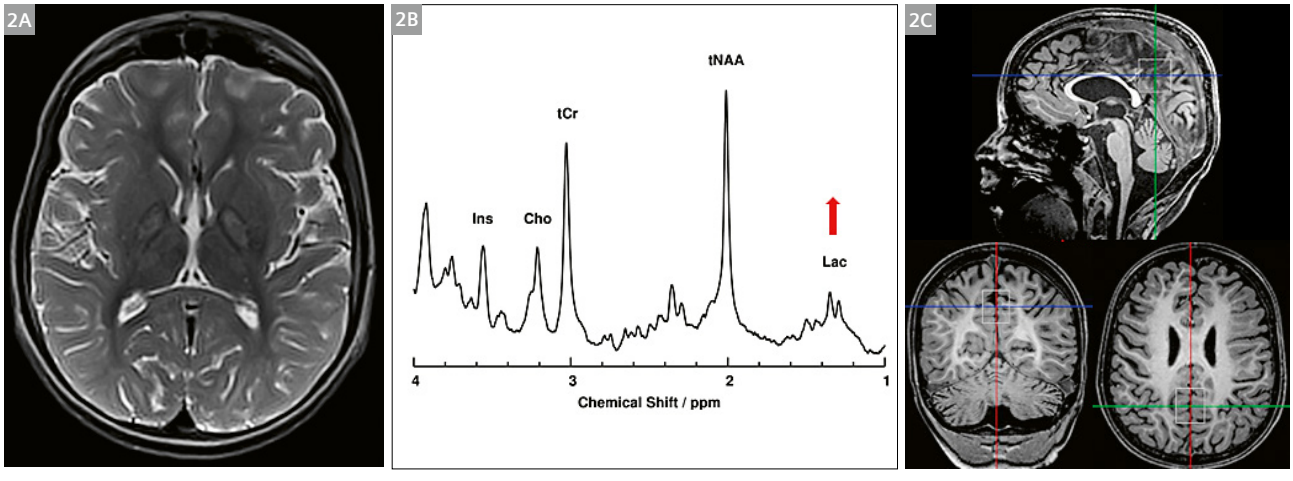

2 **^{1}H-MR spectroscopy in a boy (age 10.5 years) with a mitochondriopathy** (caused by Kearns-Sayre syndrome).
(2A) Axial T2-weighted image with high signal bilateral in the pallidum as well as subcortical occipital. **(2B)** Gray matter (GM) spectrum with lactate doublet at 1.3 ppm indicating increased brain lactate concentration. **(2C)** Voxel placement in posterior paramedian GM. Note the atrophy of the whole brain.

Lac: lactate; other parameters see Fig. 1.

Cerebrospinal fluid dynamics studied by real-time flow MRI

So far, almost all studies investigating CSF flow have employed ECG-synchronized cine PC MRI [10–12]. Thus, CSF dynamics have been thought to mainly follow cardiac-related oscillations as implicitly suggested by the experimental approach. Recent methodological advances toward real-time PC flow MRI now allow for the unique possibility of directly measuring CSF dynamics at high spatial and temporal resolution irrespective of the assumption of any periodicity. These studies have revealed the significant influence of respiration. In particular, forced inspiration has been identified as the dominant regulator of CSF dynamics in all its compartments (Fig. 4D and Fig. 5, left column) [13, 14]. The onset of every forced inspiration prompted an upward surge of CSF from the spinal canal into the head and further into the aqueduct toward the 3rd ventricle (Fig. 5). On the other hand, forced expiration led to a reversal of the flow direction and hence a downward movement, albeit to a variable extent (Fig. 4, column E and Fig. 5, left column). Figure 5 illustrates CSF flow and flow volumes during four cycles of forced respiration (see breathing protocol at the bottom). The occurrence of upward CSF flow into the head and brain in response to forced inspiration has been explained as a necessity to counterbalance the inspiratory-regulated venous flow out of the head/neck region [15]. CSF and venous blood flow appear tightly interconnected and balanced to ensure the Monro-Kellie doctrine of a constant intracranial volume. So far, CSF dynamics has mainly been investigated under normal physiological conditions, as illustrated in Figures 4 and 5 for a healthy eight-year-old boy. We are currently in the process of translating real-time PC flow MRI to clinical applications in pediatrics, which will be of eminent importance to reveal mechanisms of perturbed CSF circulation and open new approaches to therapeutic nterventions. For example, spinal cord malformations and many forms of pediatric hydrocephalus are still poorly understood and therapeutic options often controversially discussed.

Real-time PC flow MRI protocol[2]

Real-time PC flow MRI is based on highly undersampled radial gradient-echo acquisitions in combination with image reconstruction by regularized nonlinear inversion (NLINV). It offers access to high spatial and temporal resolutions [16–18]. Recently, real-time PC flow MRI was extended to a model-based reconstruction technique that jointly estimates an anatomical image, a set of coil sensitivities, and a PC velocity map directly from the flow-encoded raw data [19]. The model-based reconstruction, as seen in Figure 4 (column C, lower parts), provides velocity maps free of phase noise in regions without signal support (e.g., the lungs) thereby improving the spatial acuity of flow regions. A highly parallelized version of the reconstruction algorithm was used to reconstruct the real-time data online on a bypass computer (Sysgen, Bremen, Germany) consisting of two processors (SandyBridge E5-2650, Intel) and eight graphical processing units (GeForce GTX TITAN, Nvidia) [20]. The entire reconstruction process is fully integrated into the MRI system so that the reconstructed magnitude images and

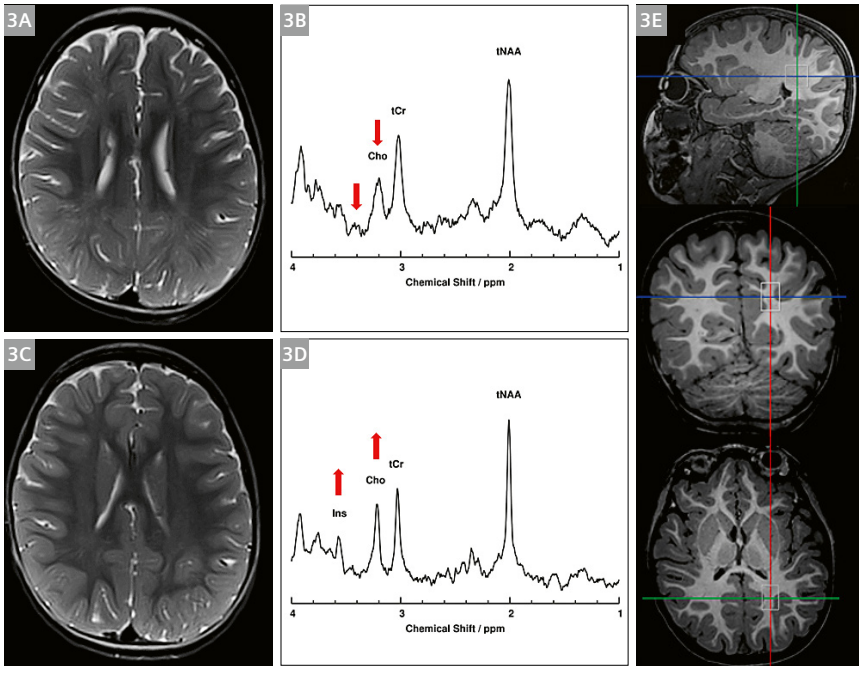

3 **^{1}H-MR spectroscopy in a girl with cerebral folate deficiency** (caused by cerebral folate transporter α deficiency).

(3A, B) (Age 5 years): (3A) Axial T2-weighted image depicts hypomyelination. (3B) White matter (WM) spectrum reveals absence of an Ins peak and a significantly reduced Cho peak.

(3C, D) After two years of folinic acid therapy (age 7 years): (3C) Axial T2-weighted image shows significant advancement of myelination now appropriate for the age. (3D) Ins and Cho peaks have increased, indicating normalization of brain metabolism under therapy.

(3E) Voxel placement in left parieto-occipital WM. Note mild cerebellar atrophy.

Parameters see Fig. 1.

velocity maps can be viewed on the scanner monitor during the measurement.

For CSF flow studies, the scan parameters were optimized to provide images with an in-plane resolution of 0.75 × 0.75 mm^2 and a temporal resolution of 125 ms. The other parameters are TR / TE = 5.68 / 4.61 ms, a flip angle of 10°, and slice thickness of 5 mm. The flow-encoded and flow-compensated acquisitions were each acquired with 11 radial spokes. Quantitative and qualitative analyses of real-time PC flow MRI measurements were performed using CaFur prototype software (Fraunhofer Mevis, Bremen, Germany) especially designed for automatic segmentation tasks using real-time image series [21].

Acknowledgments

We gratefully acknowledge the support and assistance of Prof. Jens Frahm Ph.D. and Jost Kollmeier Ms Sci from the Biomedizinische NMR at the Max-Planck-Institut für biophysikalische Chemie, Goettingen, as well as of Ilona Pfahlert, medical technician, and Dr. Peter Dechent Ph.D. from the MR-Research in Neurology and Psychiatry, University Medical Center, Goettingen.

continued on page 10

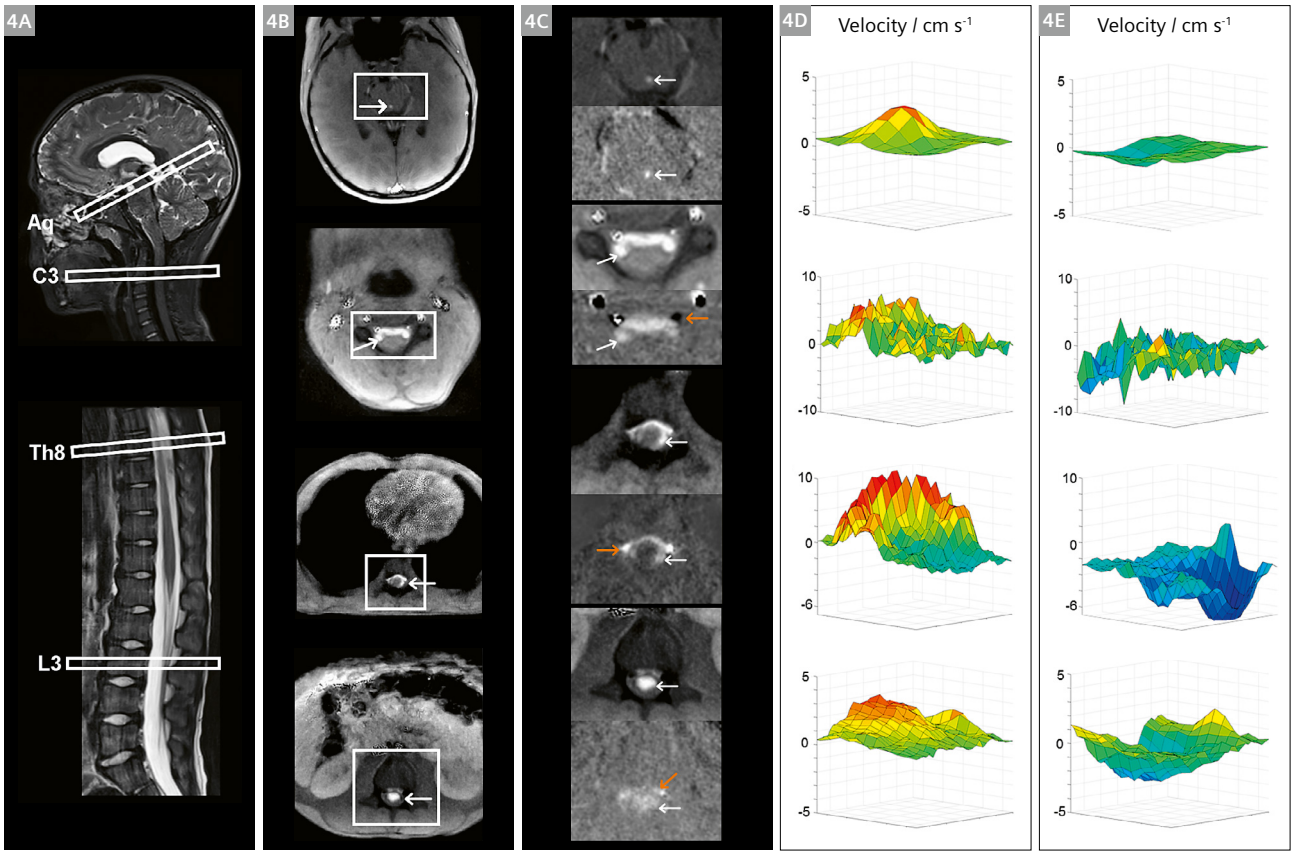

4 **Real-time PC flow MRI of CSF dynamics in spinal canal and aqueduct** (healthy control (age 8.2 years))

(4A) Lower image: Midline sagittal T2-weighted images of lumbar and lower thoracic spine; Upper image: cervical spine and brain. White rectangles indicate placement of ROIs.

(4B): Magnitude images of all ROIs during forced inspiration. Note bright flow signal in the CSF spaces at all levels (white arrows). White rectangles indicate magnified sections displayed in column (C).

(4C): Magnified sections of the magnitude images (upper part) and corresponding velocity maps (lower part) indicating upward fluid flow (bright signal; white arrows) in CSF spaces. Note the dark signal in spinal epidural veins at C3 (orange arrow) reflecting downward venous blood flow (note also phase wrap in right vein). Spinal epidural veins are also visible at Th8 and L3 (orange arrows) showing upward blood flow (bright signal).

(4D): Selected CSF flow velocity profiles during forced inspiration and

(4E): during forced expiration. Color code ranges from -10 to 10 cm/s; blue and red represent minimum and maximum velocities respectively.

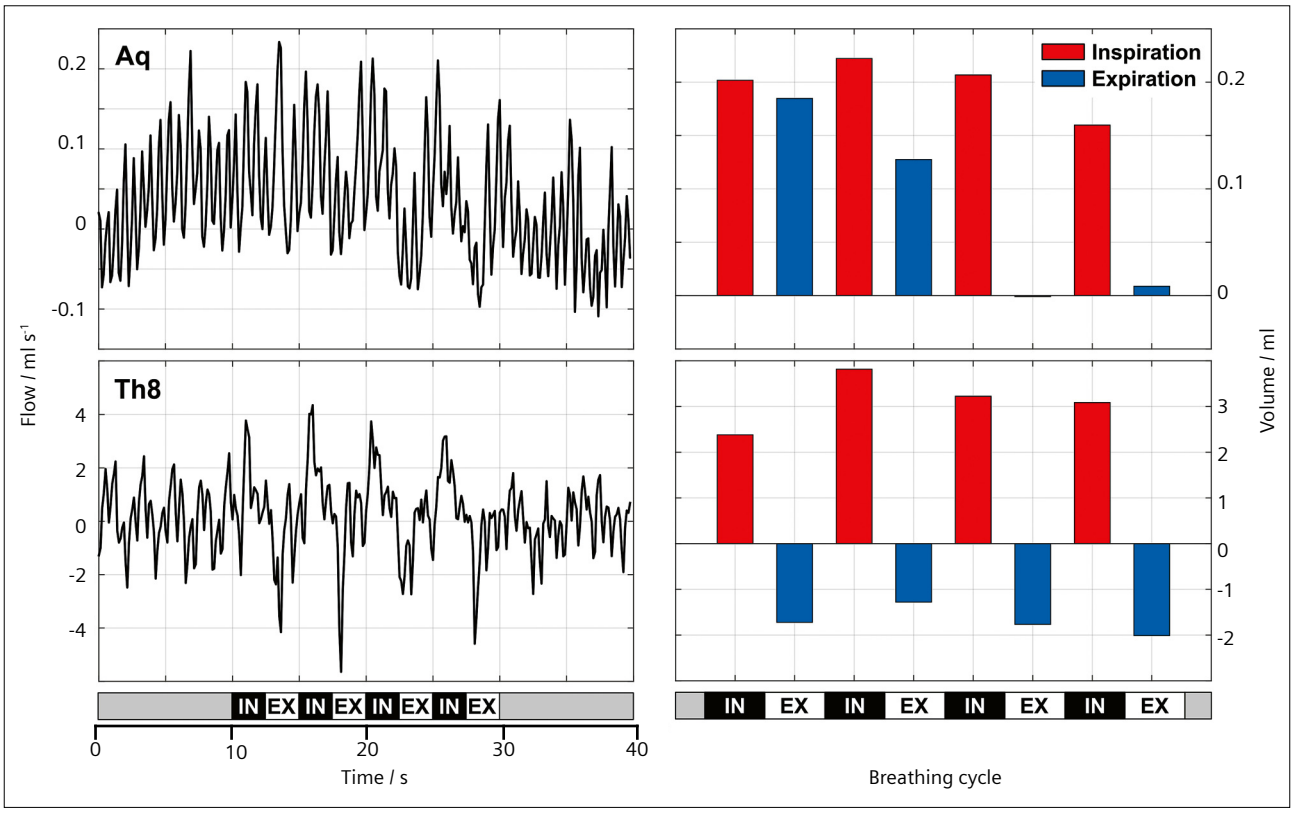

5 **CSF flow and flow volumes before, during, and after 20 sec of forced breathing** (healthy control (age 8.2 years))

Left column: CSF flow in aqueduct (Aq) (upper part) and at thoracic level 8 (Th8) (lower part) for a 40-s period comprising 20 s of forced breathing (see protocol at bottom). Onset of forced inspiration leads to distinct increase in upward CSF flow at both positions, which is reversed during expiration. Cardiac-related flow represents a continuous component of lower amplitude. Note the much smaller flow scale (mL s^{-1}) for the delicate Aq.

Right column: Corresponding CSF flow volumes for every forced inspiration (2.5 s) and expiration (2.5 s) (see breathing cycles at bottom). Inspiratory flow volumes (red) refer to upward motions (positive values) in the Aq (upper part) and at Th8 (lower part). Expiratory flow volumes (blue) were directed downward (negative values) at Th8. Of note are the small flow volumes in the Aq and the continuous positive values pointing to upward (towards the 3rd ventricle) fluid movement over the whole respiratory cycle.

Aq: aqueduct; Th8: thoracic level 8; IN: inspiration; EX: expiration.

[1]MR scanning has not been established as safe for imaging fetuses and infants less than two years of age. The responsible physician must evaluate the benefits of the MR examination compared to those of other imaging procedures. Note: This disclaimer does not represent the opinion of the authors.

[2]The information shown herein refers to products of 3rd party manufacturers and thus are in their regulatory responsibility. Please contact the 3rd party manufacturer for further information.

References

1 Dreha-Kulaczewski SF, Helms G, Dechent P, Hofer S, Gartner J, Frahm J. Serial proton MR spectroscopy and diffusion tensor imaging in infantile Balo's concentric sclerosis. Neuroradiology. 2009 Feb;51(2):113-21.

2 Kreis R, Ernst T, Ross BD. Development of the human brain: in vivo quantification of metabolite and water content with proton magnetic resonance spectroscopy. Magn Reson Med. 1993 Oct;30(4):424-37.

3 Brockmann K, Bjornstad A, Dechent P, Korenke CG, Smeitink J, Trijbels JM, et al. Succinate in dystrophic white matter: a proton magnetic resonance spectroscopy finding characteristic for complex II deficiency. Ann Neurol. 2002 Jul;52(1):38-46.

4 Henneke M, Dreha-Kulaczewski S, Brockmann K, van der Graaf M, Willemsen MA, Engelke U, et al. In vivo proton MR spectroscopy findings specific for adenylosuccinate lyase deficiency. NMR Biomed. 2010 Jun;23(5):441-5.

5 Dreha-Kulaczewski S, Kalscheuer V, Tzschach A, Hu H, Helms G, Brockmann K, et al. A Novel SLC6A8 Mutation in a Large Family with X-Linked Intellectual Disability: Clinical and Proton Magnetic Resonance Spectroscopy Data of Both Hemizygous Males and Heterozygous Females. JIMD Rep. 2014;13:91-9.

6 Almeida LS, Verhoeven NM, Roos B, Valongo C, Cardoso ML, Vilarinho L, et al. Creatine and guanidinoacetate: diagnostic markers for inborn errors in creatine biosynthesis and transport. Mol Genet Metab. 2004 Jul;82(3):214-9.

7 Steinfeld R, Grapp M, Kraetzner R, Dreha-Kulaczewski S, Helms G, Dechent P, et al. Folate receptor alpha defect causes cerebral folate transport deficiency: a treatable neurodegenerative disorder associated with disturbed myelin metabolism. Am J Hum Genet. 2009 Sep;85(3):354-63.
8 Frahm J, Michaelis T, Merboldt KD, Hanicke W, Gyngell ML, Chien D, et al. Localized NMR spectroscopy in vivo. Progress and problems. NMR Biomed. 1989 Dec;2(5-6):188-95.
9 Provencher SW. Estimation of metabolite concentrations from localized in vivo proton NMR spectra. Magn Reson Med. 1993 Dec;30(6):672-9.
10 Enzmann DR, Pelc NJ. Normal flow patterns of intracranial and spinal cerebrospinal fluid defined with phase-contrast cine MR imaging. Radiology. 1991 Feb;178(2):467-74.
11 Greitz D. Cerebrospinal fluid circulation and associated intracranial dynamics. A radiologic investigation using MR imaging and radionuclide cisternography. Acta Radiol Suppl. 1993;386:1-23.
12 Greitz D. Radiological assessment of hydrocephalus: new theories and implications for therapy. Neurosurg Rev. 2004 Jul;27(3):145-65; discussion 66-7.
13 Dreha-Kulaczewski S, Joseph AA, Merboldt KD, Ludwig HC, Gartner J, Frahm J. Inspiration is the major regulator of human CSF flow. J Neurosci. 2015 Feb 11;35(6):2485-91.
14 Chen L, Beckett A, Verma A, Feinberg DA. Dynamics of respiratory and cardiac CSF motion revealed with real-time simultaneous multi-slice EPI velocity phase contrast imaging. Neuroimage. 2015 Nov 15;122:281-7.
15 Dreha-Kulaczewski S, Joseph AA, Merboldt KD, Ludwig HC, Gartner J, Frahm J. Identification of the Upward Movement of Human CSF In Vivo and its Relation to the Brain Venous System. J Neurosci. 2017 Mar 1;37(9):2395-402.
16 Joseph A, Kowallick JT, Merboldt KD, Voit D, Schaetz S, Zhang S, et al. Real-time flow MRI of the aorta at a resolution of 40 msec. J Magn Reson Imaging. 2014 Jul;40(1):206-13.
17 Joseph AA, Merboldt KD, Voit D, Zhang S, Uecker M, Lotz J, et al. Real-time phase-contrast MRI of cardiovascular blood flow using undersampled radial fast low-angle shot and nonlinear inverse reconstruction. NMR Biomed. 2012 Jul;25(7):917-24.
18 Uecker M, Zhang S, Voit D, Karaus A, Merboldt KD, Frahm J. Real-time MRI at a resolution of 20 ms. NMR Biomed. 2010 Oct;23(8):986-94.
19 Tan Z, Roeloffs V, Voit D, Joseph AA, Untenberger M, Merboldt KD, et al. Model-based reconstruction for real-time phase-contrast flow MRI: Improved spatiotemporal accuracy. Magn Reson Med. 2017 Mar;77(3):1082-93.
20 Schaetz S, Voit D, Frahm J, Uecker M. Accelerated Computing in Magnetic Resonance Imaging: Real-Time Imaging Using Nonlinear Inverse Reconstruction. Comput Math Methods Med. 2017;2017:3527269.
21 Chitiboi T, Hennemuth A, Tautz L, Huellebrand M, Frahm J, Linsen L, Hahn H. Context-based segmentation and analysis of multi-cycle real-time cardiac MRI. IEEE Int Symp Biomed Imaging. 2014:943-6.

Contact

Steffi Dreha-Kulaczewski M.D.
Department of Pediatrics and Adolescent Medicine
Division of Pediatric Neurology
University Medical Center Göttingen
37075 Göttingen
Germany
Tel.: +49 551 39 22570
sdreha@gwdg.de

Case Series: Utilization of the Pediatric 16 Coil for 1.5T and 3T Systems

Bac Nguyen, RT (R) (MR)

Oslo University Hospital, Rikshospitalet, Oslo, Norway

Introduction

At our institution we have a high rate of pediatric cases which can be both difficult and challenging. As a University Hospital, we perform pediatric imaging[1] for a wide range of indications including the brain, spine, heart, abdomen, pelvis and whole-body and the imaging of children can involve either general anesthesia or the feed and wrap technique. In all cases, fast and robust workflows for high-resolution imaging are required. In this article, we would like to share our experiences with the Pediatric 16 coil on both 1.5T and 3T to demonstrate what it can help achieve. We had acquired the coils in December 2015 for our 1.5T MAGNETOM Aera and 3T MAGNETOM Skyra. This gives us the opportunity to easily setup our program either with anesthesia or as feed and wrap. It simplifies the setup of our busy daily program and helps us to avoid any dead- or delay time that may arise from these cases.

The Pediatric 16 is a 16-channel receive coil with 16 integrated preamplifiers for head and neck imaging of new-borns and infants up to 18 months of age[1]. There are 13 channels for head imaging and 3 channels for the neck, and these channels can be used independently. The coil is equipped with DirectConnect technology and it connects directly into the scanner table with no connecting cables. Other special features include a recess in the anterior coil for easy positioning of intubation tubes, and a 4 cm aperture at the top of the coil for better ventilation. As a Tim4G Matrix coil, the Pediatric 16 can be combined flexibly with other coils including the Spine, Body, Flex and Special Purpose coils for whole CNS and whole-body imaging and this opens many opportunities for the imaging of infants and small children[1].

While this coil is intended for infants from 0–18 months, we have experienced a few cases where children did not fit. For instance, a 1-year-old infant with hydrocephalus may not fit due to the size of the head. Conversely, a 20-month-old infant may fit perfectly. Obviously, infants vary in size and this needs to be checked in each case.

In our experience, compared to the Head/Neck 20 this dedicated pediatric coil provides much better performance at the same scan times due to the fact that the coil fits more closely to the heads of small infants. Cases 1–4 illustrate the fast and high-resolution imaging we can achieve with this coil across infants of varying ages.

Along with Pediatric 16 comes a cradle with two straps and cushions to help with fixation. This cradle was designed to enable the preparation of infants away from the scanner and to provide safe and efficient transport of the infant to the scanner. This cradle has proven itself to be a true workflow enhancer at our institution, especially for our feed and wrap examinations. Firstly, we can plan our exam in good time with other departments so the patient can come to us in a position ready for examination. We do not lose time preparing the baby at the scanner, and we find that most babies lie much more still when everything is ready. All we need to do at our department is a final check for safety aspects (puls oximetry, ECG etc.). For children requiring only brain or brain and spine scans, the cradle can be slid easily into the Pediatric 16 coil (without the need to remove the anterior part) and the patient can be put into the scanner without further coil management. If the baby requires whole-body imaging, the Body coil can be easily placed on the child. This cradle has high edges, which means that coils can be put directly on these edges for stabilization, rather than laying them directly on top of the child. There are also cases where smaller coils would be needed, such as the small Flex coil. We can position this inside the edges along with cushions. This is much easier compared to the situation where the patient is lying directly on the table with positioning sandbags along the sides. Our use of the cradle has enabled faster, robust and more comfortable examinations for the child so much so that we use the cradle even for patients requiring only body or cardiac imaging.

Cases 5 and 6 are illustrations of our patients who have undergone liver and cardiac examinations where the cradle has helped with the workflow.

[1] *MR scanning has not been established as safe for imaging fetuses and infants less than two years of age. The responsible physician must evaluate the benefits of the MR examination compared to those of other imaging procedures. Note: This disclaimer does not represent the opinion of the authors.*

Case 1

10-day-old infant[1] with left-sided seizure and suspicion of cerebral infarct. The patient weight was approximately 3 kg. Imaging was performed on a 3T MAGNETOM Skyra with the Pediatric 16 coil, as a feed and wrap procedure. There were no findings.

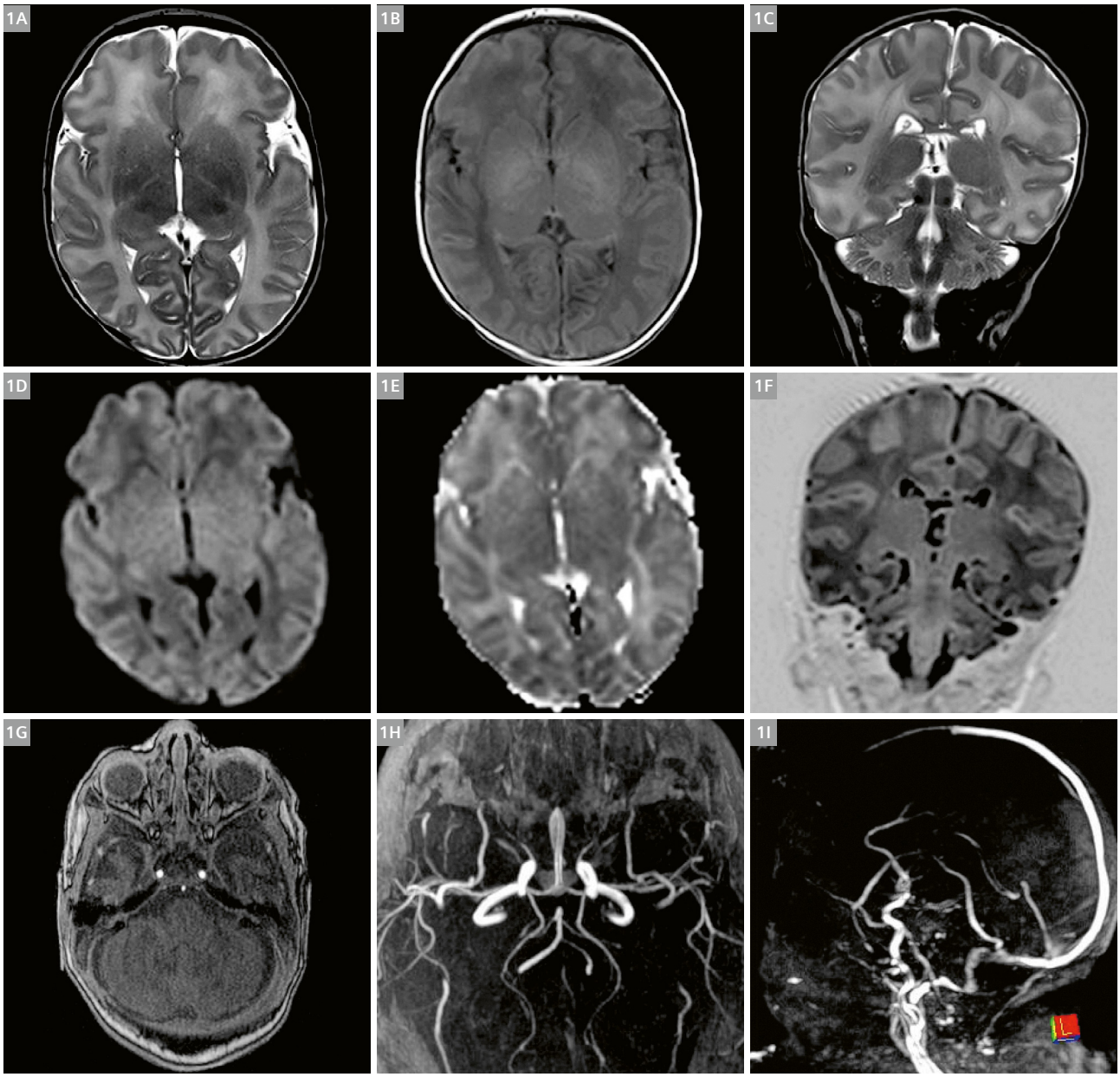

1 **(1A)** T2w TSE transversal, voxel 0.49 x 0.49 x 3 mm, TA: 2 min 12 sec.
(1B) T1w TSE transversal, voxel 0.74 x 0.74 x 3 mm, TA: 2 min 32 sec.
(1C) T2w TSE coronal, voxel 0.49 x 0.49 x 3 mm, TA: 2 min 12 sec.
(1D) Diffusion-weighted imaging (DWI) RESOLVE, b-value 1000 (acquired b0, b500 and b1000), voxel 1.5 x 1.5 x 4 mm, TA: 2 min 30 sec.
(1E) DWI apparent diffusion coefficient (ADC) map.
(1F) T1w SPACE IR coronal, voxel 1.17 x 1.17 x 0.9 mm, TA: 2 min 16 sec.
(1G) Time-of-flight (TOF) transversal, voxel 0.5 x 0.5 x 0.5 mm, TA: 3 min 42 sec.
(1H) TOF maximum intensity projection (MIP).
(1I) Phase contrast (PC) MIP sagittal, voxel 1.3 x 1 x 1 mm, TA: 4 min 37 sec.

Case 2

1-year-old male infant[1] with increasing frequency of epileptic seizures, hemiparesis, fever and a cold. The patient's weight is approximately 10 kg. Imaging was performed on a 3T MAGNETOM Skyra with the Pediatric 16 in combination with the Spine 32. The exam was performed under general anesthesia. The report for this patient indicated slight hypomyelination with a possible small syrinx in the distal medulla.

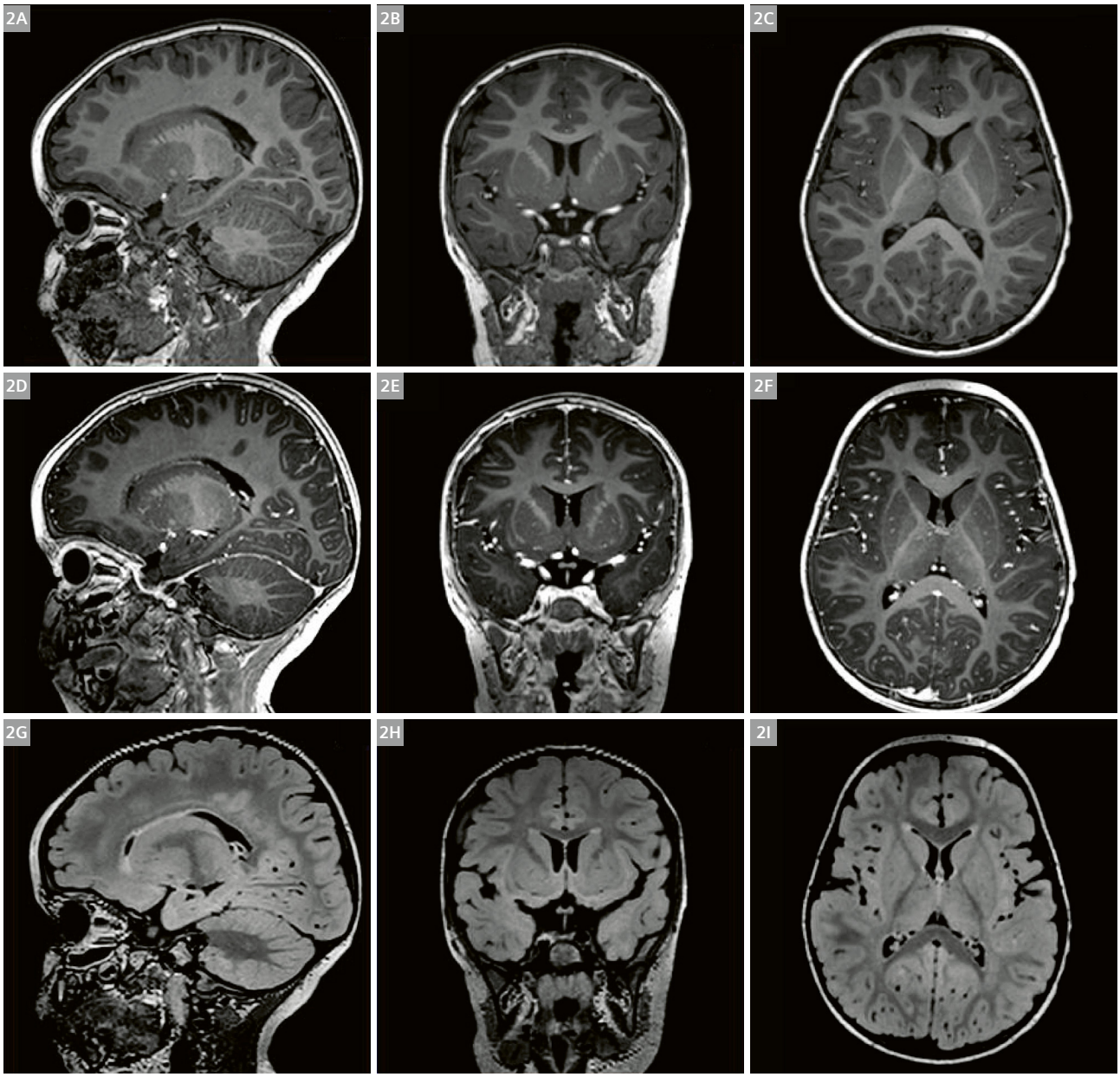

2 **(2A)** T1w 3D MPRAGE acquired in sagittal plane without contrast medium, voxel 1 x 1 x 1 mm, TA: 5 min 5 sec.
(2B) T1w 3D MPRAGE 1 mm coronal multi-planar reconstruction (MPR) without contrast.
(2C) T1w 3D MPRAGE 1 mm transversal MPR without contrast.
(2D) T1w 3D MPRAGE 1 mm acquired in sagittal plane with contrast medium, voxel 1 x 1 x 1 mm, TA: 5 min 5 sec.
(2E) T1w 3D MPRAGE 1 mm coronal MPR with contrast medium.
(2F) T1w 3D MPRAGE 1 mm transversal MPR with contrast medium.
(2G) T2w 3D SPACE FLAIR acquired in sagittal plane, voxel 1 x 1 x 1 mm, TA: 5 min 24 sec.
(2H) T2w 3D SPACE FLAIR 1 mm coronal MPR.
(2I) T2w 3D SPACE FLAIR 1 mm transversal MPR.

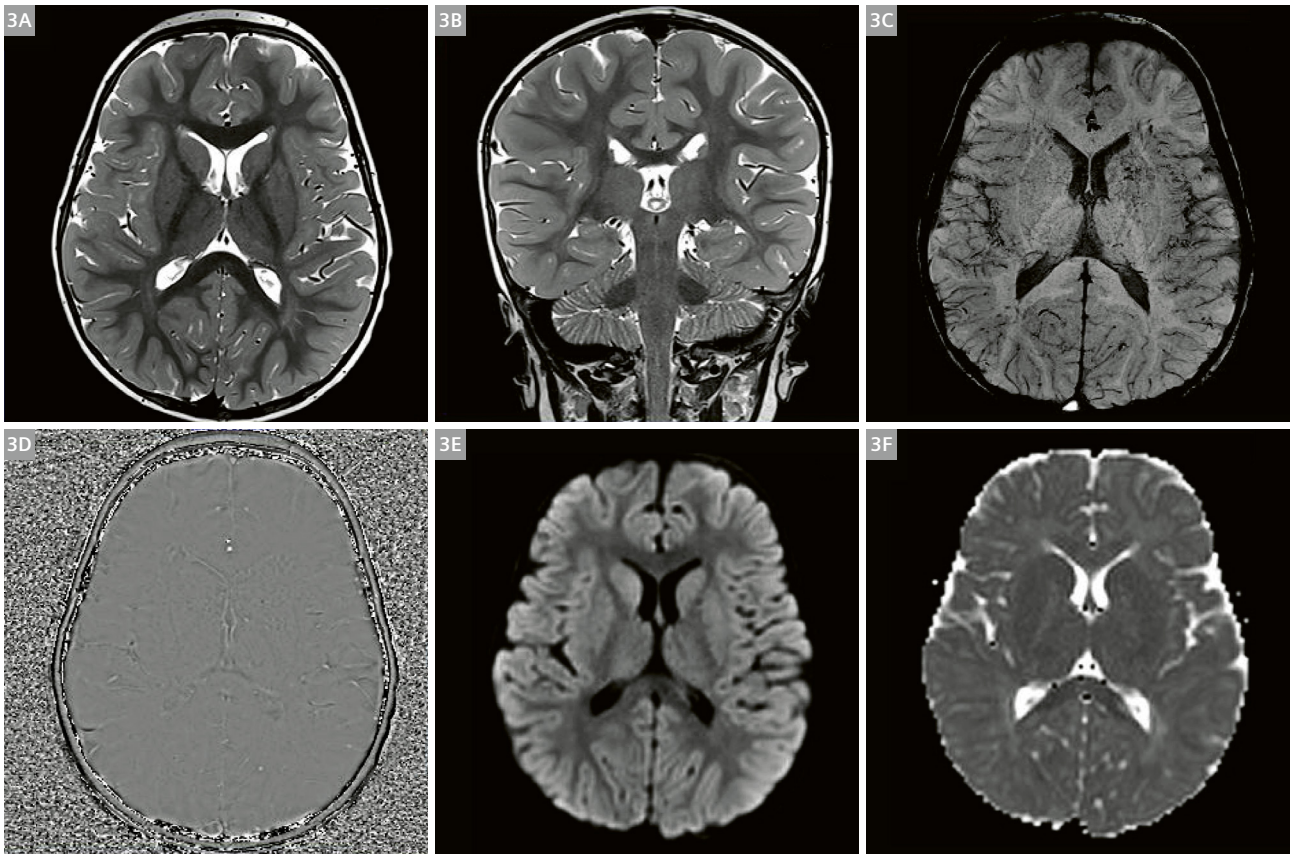

3 **(3A)** T2w TSE transversal, voxel 0.2 x 0.2 x 2 mm, TA: 4 min 32 sec.
(3B) T2w TSE coronal, voxel 0.2 x 0.2 x 2 mm, TA: 4 min 32 sec.
(3C) Susceptibility-weighted imaging (SWI) transversal minIP image, voxel 0.6 x 0.5 x 1.4 mm, TA: 5 min.
(3D) SWI Phase image.
(3E) DWI RESOLVE, b-value 1000 (acquired b0, b500 and b1000), voxel 1.5 x 1.5 x 4 mm, TA: 4 min 21 sec.
(3F) DWI ADC map.

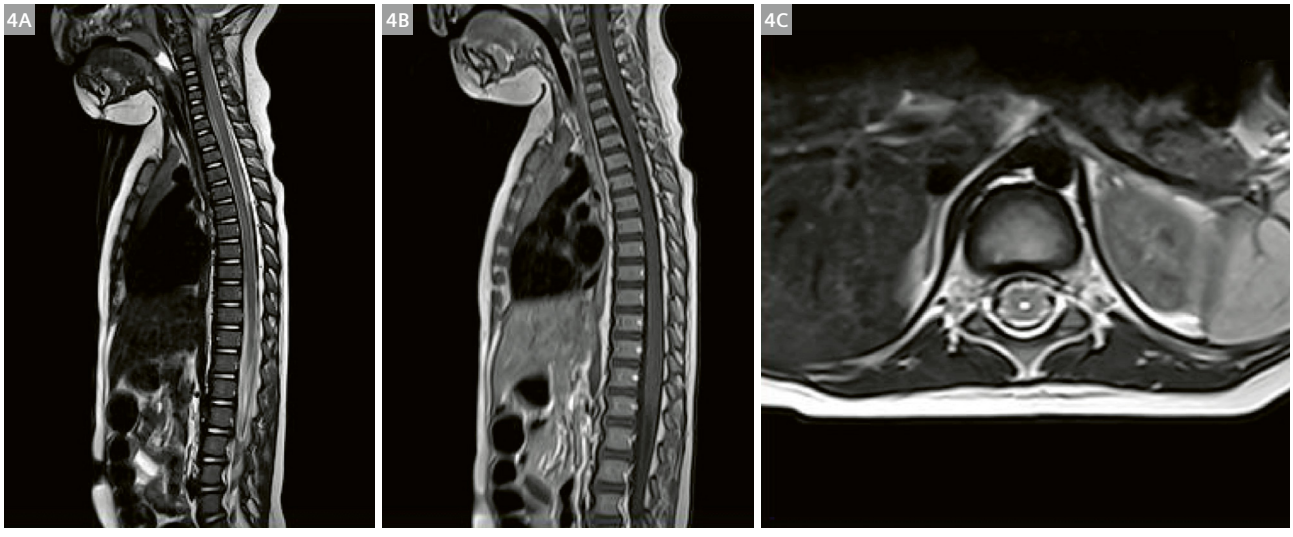

4 **(4A)** T2w TSE sagittal, voxel 0.9 x 0.8 x 2 mm, TA: 2 min 58 sec.
(4B) T1w TSE sagittal, voxel 1 x 0.9 x 2 mm, TA: 3 min 42 sec.
(4C) T2w TSE transversal, voxel 0.8 x 0.6 x 3 mm, TA: 3 min 10 sec.

Case 3

A 2-week-old infant[1] with increased head circumference with suspicion of hydrocephalus. The patient's weight is approximately 4.8 kg. Imaging was performed on the 1.5T MAGNETOM Aera with the Pediatric 16, as a feed and wrap procedure. The report indicated that this infant might have BESS (benign enlargement of the subarachnoid spaces in infancy).

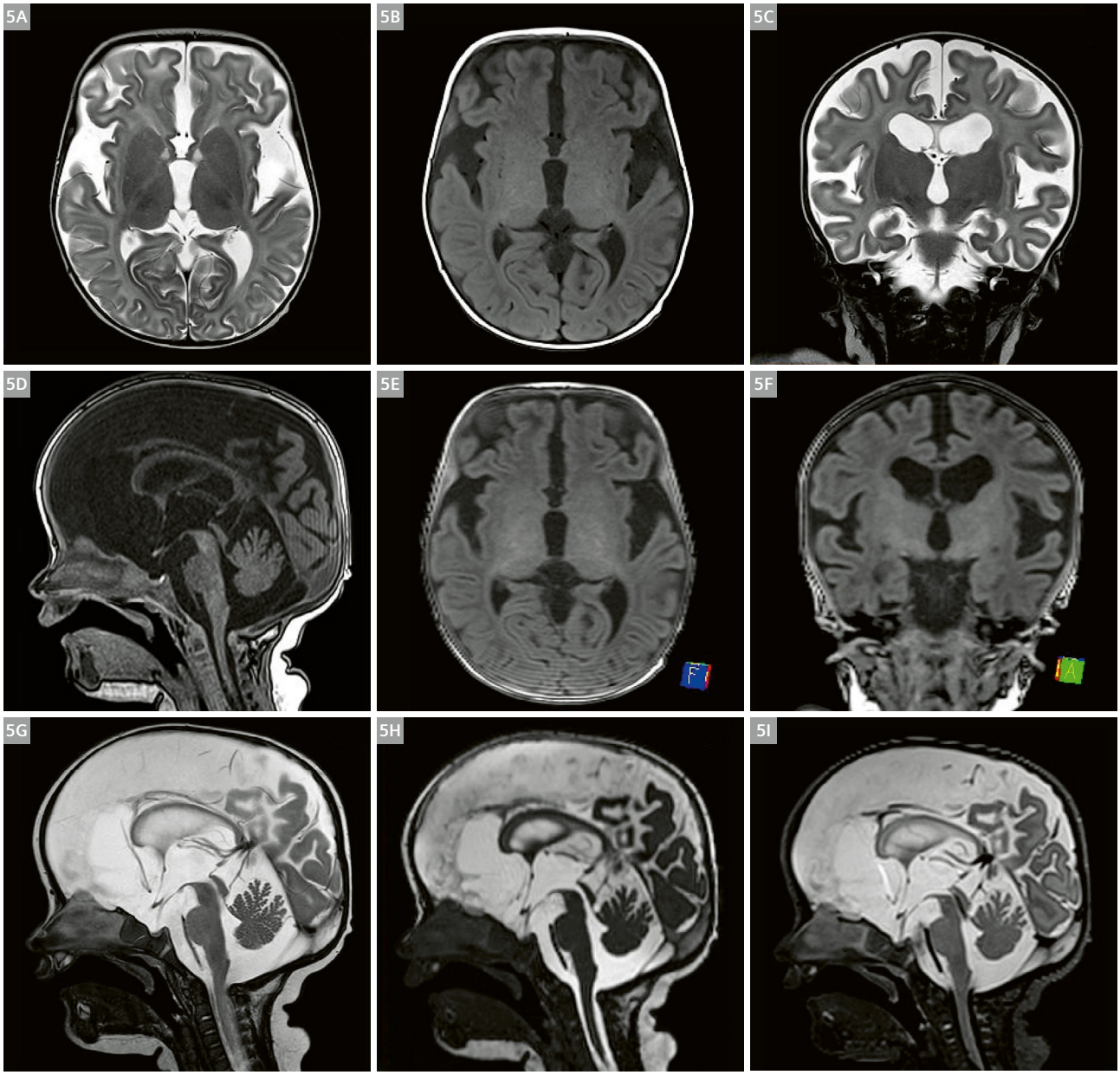

5 **(5A)** T2w TSE transversal, voxel 0.4 x 0.4 x 4 mm, TA: 4 min 32 sec.
(5B) T1w TSE transversal, voxel 0.7 x 0.7 x 4 mm, TA: 3 min 48 sec.
(5C) T2w TSE coronal, voxel 0.4 x 0.4 x 4 mm, TA: 4 min 32 sec.
(5D) T1w 3D MPRAGE, voxel 1 x 1 x 1 mm, TA: 4 min 23 sec.
(5E) T1w 3D MPRAGE 1 mm transversal MPR.
(5F) T1w 3D MPRAGE 1 mm coronal MPR.
(5G) T2w TSE sagittal, voxel 0.5 x 0.4 x 3 mm, TA: 4 min 19 sec.
(5H) CISS sagittal, voxel 0.9 x 0.9 x 0.7 mm, TA: 4 min 8 sec.
(5I) T2w 3D SPACE, voxel 1 x 1 x 1 mm, TA: 4 min 3 sec.

Case 4

2-year-old-child[1] with neuroblastoma of the neck. The patient has been imaged previously with both ultrasound and MR, but has not yet been treated. The patient's weight was approximately 6.8 kg. Imaging was performed on a 3T MAGNETOM Skyra with the Pediatric 16 in combination with Spine 32. The examination was performed under general anesthesia. The report indicated that central parts of the tumor show less contrast-enhancement compared to an earlier MRI exam, and tumor measurements remain the same.

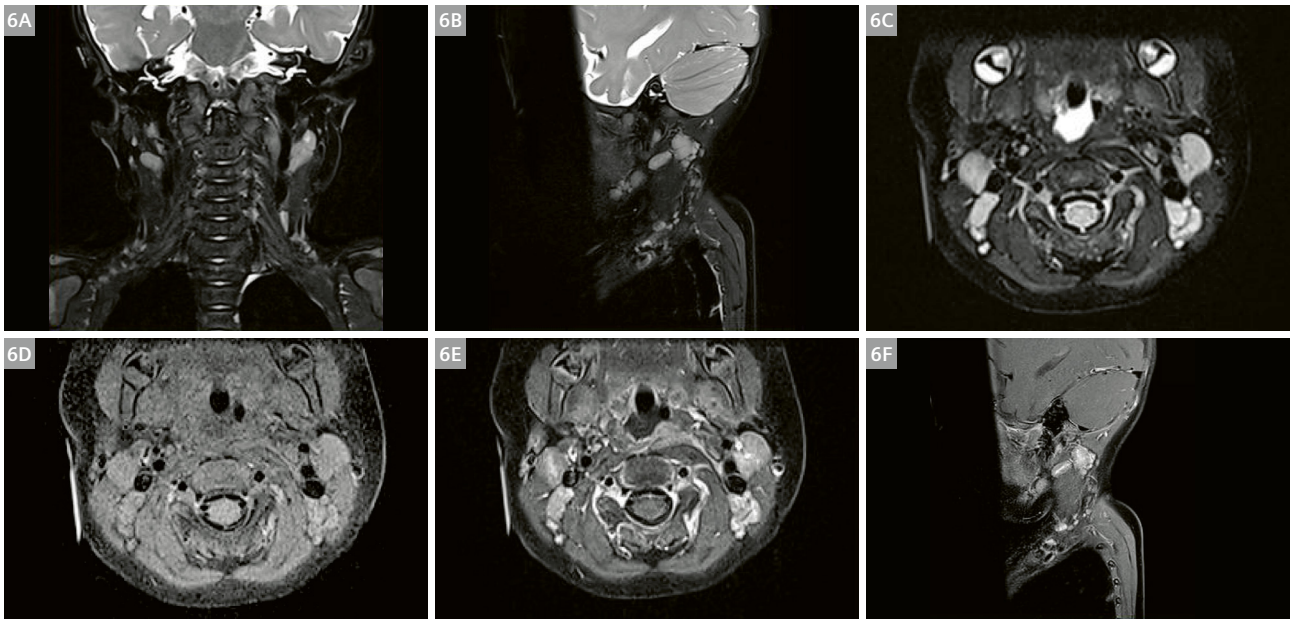

6 **(6A)** T2w TSE Dixon water only, voxel 0.7 x 0.7 x 2.5 mm, TA: 3 min 6 sec.
(6B) T2w TSE Dixon water only, voxel 0.7 x 0.7 x 2.5 mm, TA: 3 min 9 sec.
(6C) T2w TSE Dixon water only, voxel 0.7 x 0.7 x 2.5 mm, TA: 3 min 9 sec.
(6D) T1w TSE Dixon water only, voxel 0.5 x 0.5 x 2.5 mm, TA: 4 min 40 sec precontrast.
(6E) T1w TSE Dixon water only, voxel 0.5 x 0.5 x 2.5 mm, TA: 4 min 40 sec postcontrast.
(6F) T1w TSE Dixon water only, voxel 0.5 x 0.5 x 2.5 mm, TA: 4 min 23 sec postcontrast.

Case 5

A 3-week-old infant[1] with Trisomy 21 with a focal lesion seen on the left liver lobe with ultrasound and suspicion of malignancy. The patient's weight was approximately 5 kg. The examination was performed on a 1.5T MAGNETOM Aera with the Spine 32 in combination with the Flex 4 Small. The cradle of the Pediatric 16 coil was used for the preparation, transport and positioning of the patient for imaging. The examination was performed as a feed and wrap procedure. The report indicated the presence of a hypervascular tumor in the left liver lobe that could be a hemangioma.

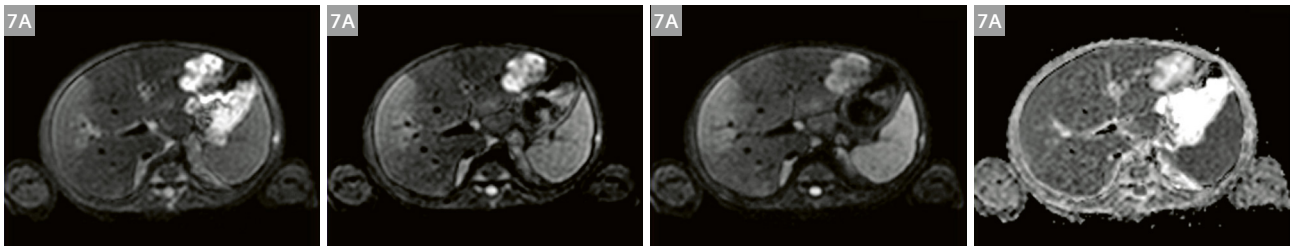

7 DWI free-breathing
(7A) b50, **(7B)** b400, **(7C)** b800, **(7D)** ADC map
voxel 2 x 2 x 3 mm, TA: 3 min.

Case continued on page 18.

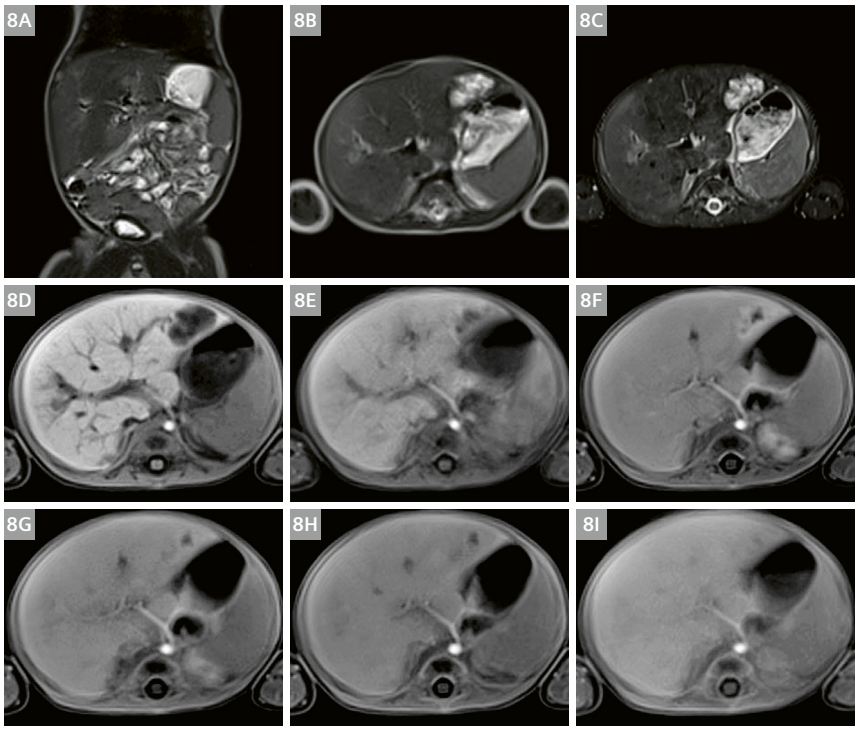

8 **(8A)** T2w HASTE coronal respiratory triggering, voxel 1.3 x 1.3 x 3.5 mm, TA: 44 sec.
(8B) T2w HASTE transversal respiratory triggering, voxel 1.3 x 1.3 x 3.5 mm, TA: 58 sec.
(8C) T2w 3D SPACE with SPAIR fatsat and respiratory triggering, voxel 1 x 1 x 1 mm, TA: approx. 5 min 20 sec.
(8D) T1w StarVIBE precontrast, voxel 1 x 1 x 3 mm, TA: 2 min 20 sec.
(8E–I) Multiple T1w StarVIBE images captured continuously after injection of contrast medium.

Case 6

A 2-year-old child[1] with congenital heart disease. The patient has DORV (double outlet right ventricle) and TGA (transposition of the great arteries). The patient was referred with the question of possible hypertrophy and for pre-operative imaging. The patient's weight was approximately 10 kg. The examination was performed on a 1.5T MAGNETOM Aera with the Spine 32 in combination with the Flex 4 Small. The cradle of the Pediatric 16 coil was used for the preparation, transport and positioning of the patient for imaging. The examination was performed under general anesthesia. The report confirmed the known clinical conditions with no change to anatomy. No hypertrophy was found.

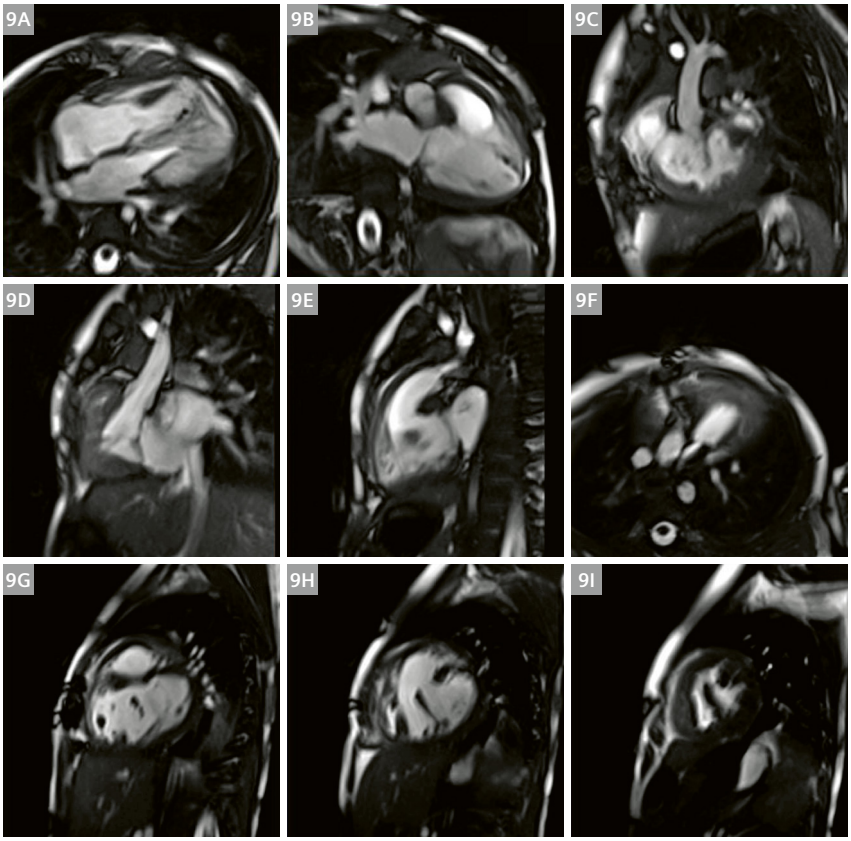

9 All images are CINE TrueFISP done as free-breathing, voxel 1.2 x 1 x 5 mm, TA: 30 sec.

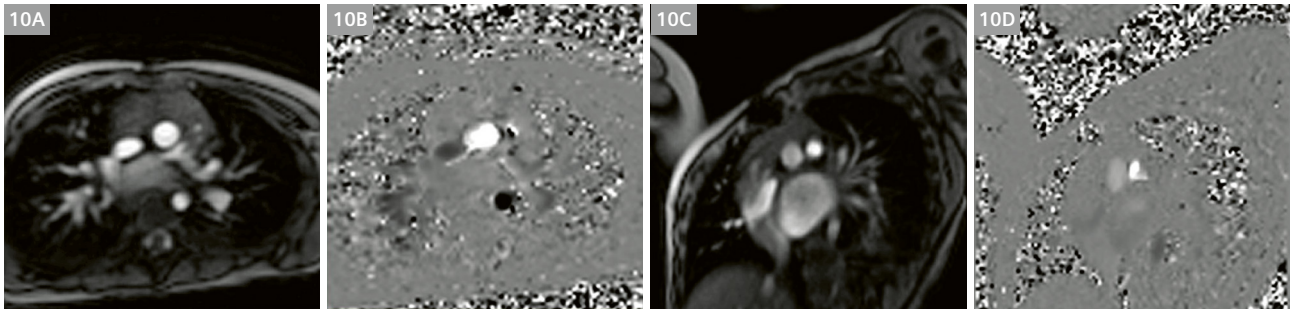

10 **(10A, B)** Flow aorta free-breathing (magnitude and phase images) VENC 120 cm/sec, voxel 1.7 x 1.5 x 5 mm, TA: 40 sec.
(10C, D) Flow pulmonary free-breathing (magnitude and phase images) VENC 400 cm/sec, voxel 1.7 x 1.5 x 5 mm, TA: 40 sec.

Conclusion

If your site does many pediatric cases, I can definitely recommend this coil. For the head imaging of neonates and small children, the size of the coil provides higher signal-to-noise ratio (SNR) which allows us to achieve better imaging in short scan times. After we started using this coil, we had many more successful feed and wrap exams thanks to the cradle itself. Given the complexity and sensitivity of an MR examination for small infants and children, it makes clinical sense to use a coil that is dedicated to their care. With the significant number of such exams that we perform at our site, the workflow benefits are, for us, innumerous.

Acknowledgments

I would like to thank my good friend and MR mentor Rolf Svendsmark. My fellow colleagues at work, and my friend Lisa Chuah.

References

1 Siemens Healthineers: https://www.healthcare.siemens.com/magnetic-resonance-imaging/options-and-upgrades/coils/pediatric-16
2 Chavhan, G., et al. Diffusion-weighted Imaging in Pediatric Body Imaging: Principles, Technique, and Emerging Applications. Radiographics 2014; 34:E73-E88.
3 Verschuuren, S., et al. Susceptibility-Weighted Imaging of the Pediatric Brain. AJR 2012;198:W440-W449.
4 Mitchell, C., et al. An Approach to Pediatric Liver MRI. AJR 2011; 196:W519-W526.
5 Panigrahy, A., et al. Basic Principles and Concepts Underlaying Recent Advances In MRI of the Developing Brain. Semin Perinatol. 2010 Feb;32(1):3-19.
6 Tong, K.A., et al. Susceptibility- Weighted MR Imaging: A Review of Clinical Applications in Children. AJR 2008.

Contact

Bac Nguyen, RT (R) (MR)
Senior MR Radiographer
Oslo University Hospital,Rikshospitalet
Sognsvannsveien 20
0372 Oslo, Norway
Phone: +47 97702111
og_23@hotmail.com

Redefining the MRI experience with Innovision

siemens-healthineers.com/innovision

Improving patient experience

Noisy and monotonous MRI exams are a thing of the past. Redefine the MRI experience with Innovision[1], the revolutionary in-bore infotainment solution. Patients are greeted by an impressive audio and video experience as soon as they lie on the table. The patient display keeps patients informed about the remaining scan time and displays predefined or custom content. Furthermore, the patient display makes the bore appear larger, helping to calm those who are anxious or claustrophobic. Innovision includes comfort pillows made of memory foam and specialized ear plugs that reduce scan noise and deliver clear audio signals to the patient. With Innovision, patients can hear their favorite music and voice commands from the technologist in excellent sound quality.

Planned benefits of Innovision at a glance:

- Enhance the patient experience with customizable video content
- Address claustrophobia and anxiety with a patient display that creates a virtually larger bore
- Keep the patient informed by displaying the remaining scan time
- Exceptional sound quality for voice commands and entertainment
- Effective noise reduction with a unique memory foam pillow and specialized ear plugs

[1]*Innovision is still under development and not yet commercially available. Its future availability cannot be guaranteed.*

SIEMENS Healthineers

Deep Cervical Infantile Hemangioma Identified by Time-Resolved Magnetic Resonance Angiography

Nicole Seyfried[1]; Vikas Gulani[2]; Verena Carola Obmann[3]

[1] School of Medicine, Case Western Reserve University, Cleveland, OH, USA
[2] Case Western Reserve University and University Hospitals Case Medical Center, Cleveland, OH, USA
[3] Department of Diagnostic, Interventional and Pediatric Radiology (DIPR), Inselspital, Bern University Hospital, University of Bern, Switzerland

Abstract

Infantile hemangiomas are the most common benign vascular tumors of infancy. We present a case report of a 5-month-old[1] female presenting with a posterior neck mass that was later diagnosed as an infantile hemangioma. We describe the application of time-resolved MR angiography in the evaluation of a pediatric vascular anomaly.

Introduction

Infantile hemangiomas (IHs) are common, benign tumors of vascular origin. Often arising shortly after birth, these lesions demonstrate a proliferative phase followed by an involution phase that may last several years [1]. Although generally self-limited in nature, potential complications of IH include scarring and disfigurement, airway obstruction, congestive heart failure and vision loss [2]. The majority of infantile hemangiomas may be diagnosed clinically, although deep lesions and those presenting without cutaneous involvement warrant further investigation to rule out other vascular malformations, especially high flow lesions that may require different treatment [1]. Furthermore, due to the risks of complications such as airway obstruction, imaging is indicated for suspected pediatric vascular anomalies of the head and neck [3]. Ultrasound imaging with spectral Doppler plays a strong role in imaging vascular anomalies in pediatric patients [4]. MRI including T1 and T2-weighted images and MR angiography are used for diagnosis and to evaluate the extent of the lesion [5]. Time-resolved MR angiography with technologies such as 3D time-resolved imaging of contrast kinetics (TRICKS) or contrast-enhanced time-resolved MR angiography (MRA) with interleaved stochastic trajectories (TWIST) technique allows dynamic evaluation of pediatric head and neck vascular anomalies

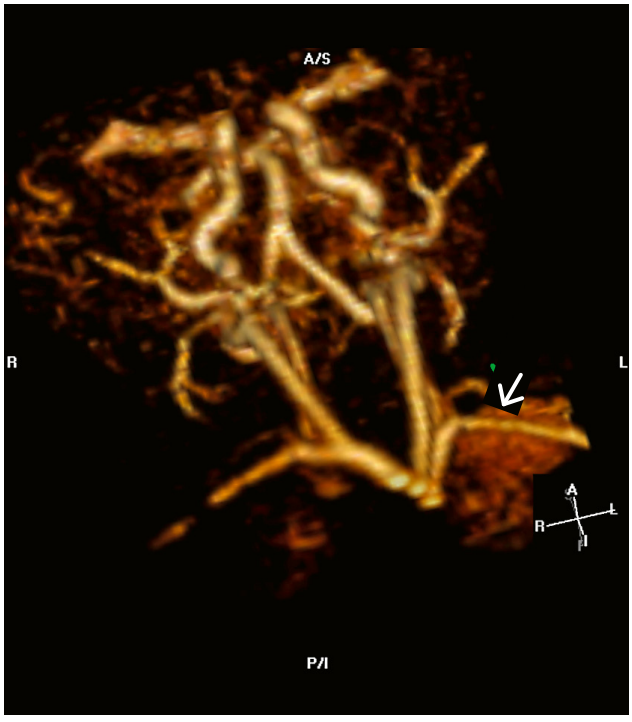

1 Capture from a rotated arterial phase MIP from a frame showing the tortuous vessel filling the lesion in this phase of enhancement. *Access the .avi clip at: www.siemens-healthineers.com/TWIST*

[1] *MR scanning has not been established as safe for imaging fetuses and infants less than two years of age. The responsible physician must evaluate the benefits of the MR examination compared to those of other imaging procedures. Note: This disclaimer does not represent the opinion of the authors.*

while preserving both temporal and spatial resolution and eliminating the need for breath-holds and specific timing of the contrast bolus [3, 6, 7, 8]. A Keyhole-like acceleration scheme is employed [9]. Central portions of *k*-space are updated more often, while peripheral portions of *k*-space are updated less frequently, sharing information across multiple frames. This allows dynamic contrast imaging with a high frame rate that is governed principally by the update rate of the center of *k*-space. Very small boluses of gadolinium can be employed along with a dynamic free breathing acquisition, allowing imaging of even very small children[1] without general anesthesia.

Case report

A 5-month-old[1] female patient presented in 2009 with a left posterior shoulder mass. The mass had been enlarging in size since one month of age. Additionally, a right lateral brow cyst was present since birth and had been noted to be enlarging in proportion to the patient. There were no other peripheral anomalies and past medical history was otherwise unremarkable. Evaluation was performed to determine the extent of the lesion and to assess whether this was a high flow abnormality. Images were obtained with a 3 plane localizer, a contrast-enhanced 4D dynamic time-resolved MRA technique using the TWIST sequence, and coronally reconstructed and axially reconstructed fat-saturated 3D VIBE pre- and post-contrast. Imaging was performed on a 3T MAGNETOM Verio (Siemens Healthcare, Erlangen, Germany). Slice thickness was 1.1 mm, frame rate was 2 seconds per frame, FOV was 195 x 272, resolution 1.1 x 1.1 x 1.1 mm^3, FA 25 degrees, GRAPPA factor 2 x 2, for a total acceleration of 4. The central "A" region of *k*-space that is updated with every frame was set at 14% and the 33% of the outer "B" region was updated with each frame. Dynamic subtraction images along with time-resolved subtraction MIPs in three planes were obtained, along with 3-dimensional reformats from selected planes. The patient received moderate sedation with the assistance of the Pediatric Sedation Unit at our institution, which specializes in sedation of children. General anesthesia was not administered. Per a protocol developed at our institution for dynamic imaging of very small children, a small amount of Propofol was hand-injected into the intravenous line just prior to injection of Gadolinium contrast, in order to minimize patient motion in response to contrast injection. 1.2 ml of gadolinium-based contrast (Magnevist, Bayer, Leverkusen, Germany) and a subsequent saline flush were hand-injected. Imaging revealed a 3.5 x 2.0 x 2.1 cm mass in the posterior cervical soft tissue. The mass demonstrated high signal intensity in T2-weighted images and low signal intensity in T1-weighted images. On dynamic post-contrast imaging the lesion was observed to fill in the arterial phase from a tortuous vessel arising from the proximal left subclavian artery (Fig. 1). Venous phase imaging demonstrated two draining veins, which fed into the distal left subclavian vein (Fig. 2). Time resolved subtracted MIP images, as well as single frame movies from the arterial phase and venous phase are also shown. *To access the .avi's please visit www.siemens-healthineers.com/TWIST*.

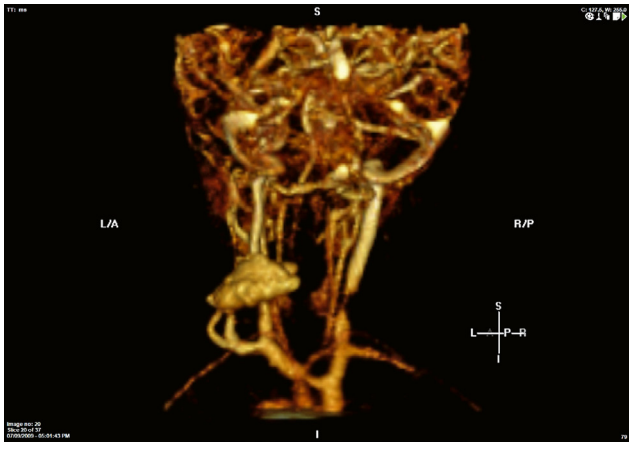

2 Capture from a venous phase MIP showing the two veins draining from the lesion.
Access the .avi clip at: www.siemens-healthineers.com/TWIST

One month after imaging revealed the vascular lesion, the patient was referred to plastic surgery for evaluation of both the right lateral brow cyst, thought to be a dermoid cyst, and the left cervical vascular lesion. On physical exam, the cervical lesion was compressible and non-tender. Cardiac and pulmonary findings were unremarkable. The decision was made to schedule a surgical excision of both the lateral brow cyst and the cervical vascular lesion. Due to the well-circumscribed nature of the lesion, this was attempted without additional radiologic intervention. The surgery was performed when the patient was 10 months of age. The entire cervical vascular lesion was surgically excised and sent to pathology for evaluation. Immunostaining for GLUT1 was positive and an infantile hemangioma was diagnosed.

Discussion

Brief case summary

A 5-month-old female patient with a left posterior cervical mass and a right lateral brow cyst presented for imaging evaluation. Contrast-enhanced 4D dynamic time-resolved MRA using the TWIST sequence was performed, revealing a vascular lesion in the deep cervical soft tissue with prominent arterial filling of a feeder vessel originating from the proximal subclavian artery and two draining veins leading into the left subclavian vein. Surgical excision of the infantile hemangioma was performed 6 months later with good results.

Infantile hemangioma:
Etiology, diagnosis and treatment

Infantile hemangioma is an extremely common vascular tumor of infancy. The incidence has been shown to be 4–5%. The lesions consist mainly of capillaries and endothelial cells and may be superficial, deep or compound [1]. The etiology of IH is not well understood, although several theories have been considered. Associated risk factors for IH include low birth weight, female gender, Caucasian race and advanced maternal age. Familial associations have also been reported [10]. Mechanisms of pathogenesis have been debated and one suggested mechanism is that tissue hypoxia, which results in an upregulation in transcription of genes including GLUT1, contributes to endothelial proliferation and formation of IH [10]. GLUT1 immunostaining has been shown to be positive in 95% of IHs. Normal vascular endothelial cells do not express GLUT1 [12].

Diagnosis of infantile hemangioma can be made clinically in 93% of cases. Clinical diagnosis is made using the classification system of Mulliken and Glowacki, which distinguishes hemangiomas from vascular malformations [13]. Further classification has been delineated by the International Society for the Study of Vascular Anomalies (ISSVA) [3]. The 7% of cases of IH that cannot be diagnosed clinically warrant further investigation, including ultrasonography or MRI [5]. Additionally, imaging may be used in cases of soft tissue vascular anomalies in order to determine the extent of the lesion. Multiple MRI sequences are typically used to evaluate the lesion. T1-weighted images show anatomic detail while T2-weighted images with fat saturation demonstrate the lesion. Gadolinium-based contrast is often administered and post-contrast sequences are obtained. Time-resolved MR angiography can be utilized in order to visualize dynamic filling of the lesion in the arterial phase and the venous phase [5]. Time-resolved MR angiography with interleaved stochastic trajectories (TWIST) has many advantages in the imaging diagnosis of pediatric soft tissue vascular lesions. Dynamic contrast-enhanced images can be acquired with a high spatial resolution in a short period of time as described above. This eliminates the need for specific timing of the contrast bolus, a challenge in the pediatric population. High spatial and temporal resolution allows for significant anatomic detail of vessels. The necessity of cessation of breathing during imaging acquisition is negated, allowing for the imaging of pediatric patients for which a breath-hold is not possible. TWIST has been shown to have a higher sensitivity and a comparable specificity to conventional contrast-enhanced MRI in the diagnosis of infantile hemangioma [3, 14]. Many additional applications of time-resolved MR angiography have been described [8, 14].

Infantile hemangiomas often do not require treatment and will involute over time. High risk lesions may be treated with oral or topical beta blockers [2]. Surgical resection has been argued to be a first line treatment to prevent permanent disfigurement caused by rapid and unpredictable high rates of growth of these lesions [15].

Conclusion

Infantile hemangioma is a common benign vascular tumor of infancy. IHs are often diagnosed clinically and are self-limiting in nature, however lesions localized to the head and neck warrant further investigation with imaging to rule out malignant causes and to evaluate risk of complications. Time-resolved MR Angiography with stochastic interleaved trajectories (TWIST) provides a non-invasive imaging modality for evaluation of IH while allowing for dynamic visualization of the lesion with high temporal and spatial resolution.

To access the .avi clips please visit
www.siemens-healthineers.com/TWIST

References

1 Adams DM, Ricci KW. Infantile Hemangiomas in the Head and Neck Region. Otolaryngol Clin North Am. 2018 Feb;51(1):77-87. doi: 10.1016/j.otc.2017.09.009. Review. PubMed PMID: 29217069.

2 Smith CJF, Friedlander SF, Guma M, Kavanaugh A, Chambers CD. Infantile Hemangiomas: An Updated Review on Risk Factors, Pathogenesis, and Treatment. Birth Defects Res. 2017 Jul 3;109(11):809-815. doi: 10.1002/bdr2.1023. Epub 2017 Apr 12. Review. PubMed PMID: 28402073; PubMed Central PMCID: PMC5839165.

3 Higgins LJ, Koshy J, Mitchell SE, Weiss CR, Carson KA, Huisman TA, Tekes A. Time-resolved contrast-enhanced MRA (TWIST) with gadofosveset trisodium in the classification of soft-tissue vascular anomalies in the head and neck in children following updated 2014 ISSVA classification: first report on systematic evaluation of MRI and TWIST in a cohort of 47 children. Clin Radiol. 2016 Jan;71(1):32-9. doi: 10.1016/j.crad.2015.09.006. Epub 2015 Oct 21. PubMed PMID: 26474946.

4 Johnson CM, Navarro OM. Clinical and sonographic features of pediatric soft-tissue vascular anomalies part 1: classification, sonographic approach and vascular tumors. Pediatr Radiol. 2017 Aug;47(9):1184-1195. doi: 10.1007/s00247-017-3885-y. Epub 2017 Aug 4. Review. PubMed PMID: 28779195.

5 Navarro OM. Magnetic resonance imaging of pediatric soft-tissue vascular anomalies. Pediatr Radiol. 2016 May;46(6):891-901. doi: 10.1007/s00247-016-3567-1. Epub 2016 May 26. Review. PubMed PMID: 27229506.

6 Korosec Fr, Frayne R, Grist TM, Mistretta CA. Time-resolved contrast-enhanced 3D MR angiography. Magn Reson Med 1996; 36:345-351.

7 Laub G. Kroeker R. *syngo* TWIST for dynamic time-resolved MR angiography. MAGNETOM Flash 2006; 3;92-95.
8 Blackham KA, Passalacqua MA, Sandhu GS, Gilkeson RC, Griswold MA, Gulani V. Applications of time-resolved MR angiography.AJR Am J Roentgenol. 2011 May;196(5):W613-20. doi: 10.2214/AJR.10.4227. Review. PubMed PMID: 21512053.
9 Van Vaals J, Brummer M, Dixon W, et al. 'Keyhole' method for accelerating imaging of contrast agent uptake. J Magn Reson Imaging 1993; 3:671-5.
10 Castrén E, Salminen P, Vikkula M, Pitkäranta A, Klockars T. Inheritance Patterns of Infantile Hemangioma. Pediatrics. 2016 Nov;138(5). pii: e20161623. Epub 2016 Oct 12. PubMed PMID: 27940781.
11 Janmohamed SR, Madern GC, de Laat PC, Oranje AP. Educational paper: Pathogenesis of infantile haemangioma, an update 2014 (part I). Eur J Pediatr. 2015 Jan;174(1):97-103. doi: 10.1007/s00431-014-2403-6. Epub 2014 Aug 26. Review. PubMed PMID: 25156689.
12 van Vugt LJ, van der Vleuten CJM, Flucke U, Blokx WAM. The utility of GLUT1 as a diagnostic marker in cutaneous vascular anomalies: A review of literature and recommendations for daily practice. Pathol Res Pract. 2017 Jun;213(6):591-597. doi: 10.1016/j.prp.2017.04.023. Epub 2017 Apr 27. Review. PubMed PMID: 28552538.
13 MacFie CC, Jeffery SL. Diagnosis of vascular skin lesions in children: an audit and review. Pediatr Dermatol. 2008 Jan-Feb;25(1):7-12. doi: 10.1111/j.1525-1470.2007.00573.x. Review. PubMed PMID: 18304145.
14 Obmann VC, Chalian M, Mansoori B, Sanchez E, Gulani V. Advantages of time-resolved contrast-enhanced 4D MR angiography in splenic arterial steal syndrome. Clin Imaging. 2018 May - Jun;49:169-173. doi: 10.1016/j.clinimag.2018.03.003. Epub 2018 Mar 7. PubMed PMID: 29558712.
15 Boyd VC, Bui D, Naik B, Levy ML, Hicks MJ, et al. Surgery: The Treatment of Choice for Hemangiomas. Seminars in Plastic Surgery. 2006 August; 20(3):163-168.

Contact

Vikas Gulani, M.D.
Department of Radiology
Case Western Reserve University
University Hospitals Case Medical Center
11100 Euclid Ave
Bolwell Building, Room B120
Cleveland, OH 44106
USA
vxg46@case.edu


Vikas Gulani


Nicole Seyfried


Verena Obmann

Fetal MR Imaging: An Overview

Xianyun Cai[1]; Xin Chen[1]; Cong Sun[1]; Tuantuan Wang[1]; Hong Tang[1]; Jinxia Zhu[2]; Guangbin Wang[1]

[1]Department of MR, Shandong Medical Imaging Research Institute, Shandong University, China
[2]Siemens Healthineers, MR Collaboration, Beijing, China

The primary objective of prenatal diagnosis is to obtain genetic, anatomical, biochemical, and physiological information about the fetus that will allow the detection of any abnormalities that may have implications for the fetal and postnatal periods. This will make it possible to offer the family information, genetic counseling, and therapeutic alternatives. The main imaging method used for routine fetal examinations is ultrasonography (US). It is noninvasive, inexpensive, widely available, and can provide real-time studies without ionizing radiation. However, in cases of advanced gestational age, patient obesity, oligohydramnios, improper fetal position, and interposition of intestinal gas or pelvic acoustic shadows, US might have technical limitations and be unable to confirm findings. In our department, we consider using MRI when the US findings are equivocal or when the US images are difficult to interpret due to factors such as late pregnancy or an inaccessible fetal position. Fetal MR imaging[1] is regarded as a valuable adjuvant imaging tool for dedicated cases at field strengths of 3T or less. In general, with appropriate sequence adaptations, examinations of the fetus at 3T are comparable with images obtained at 1.5T. Also, because of the higher image resolution and signal-to-noise ratio (SNR), finer structures and lesions can be delineated at 3T. However, a major drawback is that examinations at 3T are more prone to artifacts, which complicates imaging the fetus for traditional referrals (maternal obesity, polyhydramnios). It is therefore important to decide which system might be better suited to address certain indications [1]. Investigation of normal organ development with fetal MRI has been described by Prayer et al. [2]. Maturational processes in utero are characterized by changes in the shape, size, and content/composition of organs, and by their relationship to each other.

In our institution, all the MRI examinations were performed on a 1.5T MAGNETOM Amira (Siemens Shenzhen Magnetic Resonance, Shenzhen, China) with spine and body array coils positioned over the lower pelvic area. Since our department introduced fetal MRI in June 2006, a total of 15,000 pregnant women with various anomalies (screened by ultrasonography) have been referred for fetal MRI examinations at our institution. The cases include brain, spine, chest, and abdominal anomalies. A placental MRI scan was performed for the first time in 2009, and 1,102 such scans have been performed to date. A total of 235 fetal spine scans have been performed since 2015, when susceptibility-weighted imaging (SWI) – a technique developed by Siemens [3], which conventionally uses the BOLD mechanism to generate venograms of the brain and to quantify venous oxygenation levels [4] – was first modified for fetal spine imaging with fast data acquisition by Robinson et al. [5]. In recent years, the development of MR sequences has led to major changes in fetal MRI imaging in our unit.

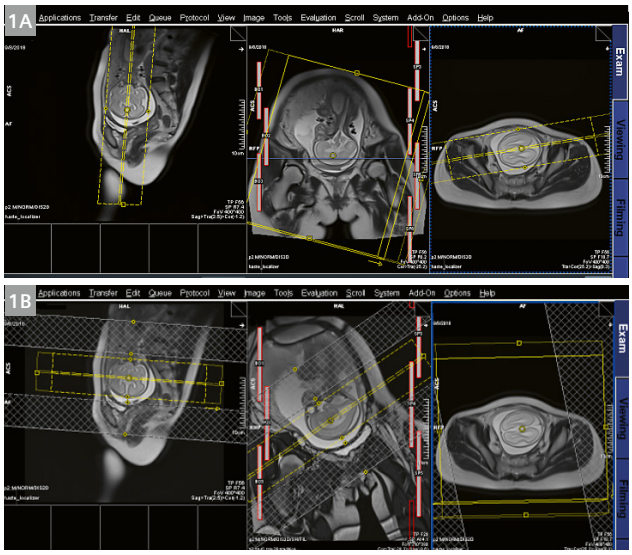

1 Sagittal and coronal localizer images of the fetal brain.

[1]*Siemens Healthineers disclaimer does not represent the opinion of the authors: MR scanning has not been established as safe for imaging fetuses and infants less than two years of age. The responsible physician must evaluate the benefits of the MR examination compared to those of other imaging procedures.*

The rise and development of fetal magnetic resonance imaging

Origins

Since fetal MR imaging was first used in 1983 [6], no consistent or convincing evidence has emerged to suggest that briefly exposing a fetus to the changing electromagnetic fields of MR imaging has any harmful effects. In the early days, however, the acquisition time was too long and the motion artifacts were severe, which resulted in poor image quality and hindered the development of fetal MRI. With the development of ultrafast sequences in the 1990s, such as single-shot steady-state free precession (SSFP), half-fourier acquisition single-shot turbo spin echo (HASTE), fast T1-weighted gradient echo, and echo planar imaging, MR imaging became a noninvasive modality that could complement US in detecting fetal abnormalities, establishing prognoses, and assisting in perinatal management.

Safety

With fetal MRI, safety considerations such as exposure times, gradient field switching, noise, and radiofrequency power deposition should be kept in mind while following established guidelines [5–9]. No documented indications exist for using contrast agents in fetal MR imaging. Generally speaking, fetal MR imaging should be avoided in the first trimester, since the fetal cells are rapidly dividing and differentiating, and the influence of MRI on organogenesis is still unclear. Also, it is difficult to obtain good-quality images in very young fetuses.

Another important issue to consider in fetal MRI concerns gadolinium-based intravenous contrast media. These agents have been shown to cross the placenta and may appear in the fetal bladder, which means they are reabsorbed from the amniotic fluid by swallowing. The use of gadolinium-based contrast agents for MR imaging in pregnant women remains controversial. Recently, an animal experiment was conducted to determine whether gadolinium remains in juvenile nonhuman primate tissue after maternal exposure to intravenous gadoteridol during pregnancy. The study concluded that gadoteridol could cross the placenta. Given the similarities between human and nonhuman primate placental physiology, the study suggests there could be relatively little deposition in human fetal tissues after maternal gadoteridol injection. However, the long-term risk of such low levels of gadolinium deposition is still unknown. At our institution, no intravenous injection (of gadolinium agents or sedation agents) was used for any of the examinations, and specific absorption rate limits were in keeping with departmental protocols.

Moreover, maternal indications for prenatal MRI also need to be taken into account.

Fetal MR imaging

All the patients were imaged in supine or left-lateral position, depending on what was most comfortable. Fetal images are obtained in three orthogonal planes in the mother to plan the sagittal, coronal, and axial views of the fetus. The last sequence is used as a reference for planning the next sequence to compen-sate for fetal movement. All sequences are performed in all three planes through the fetus. Additional imaging planes, such as oblique sagittal or coronal positions, were obtained as needed. An axial T2-weighted sequence may be performed through the fetal brain for purposes of gestational dating. In recent years, ultrafast MR imaging sequences have provided short image acquisition times and usually prevent fetal motion from degrading image quality.

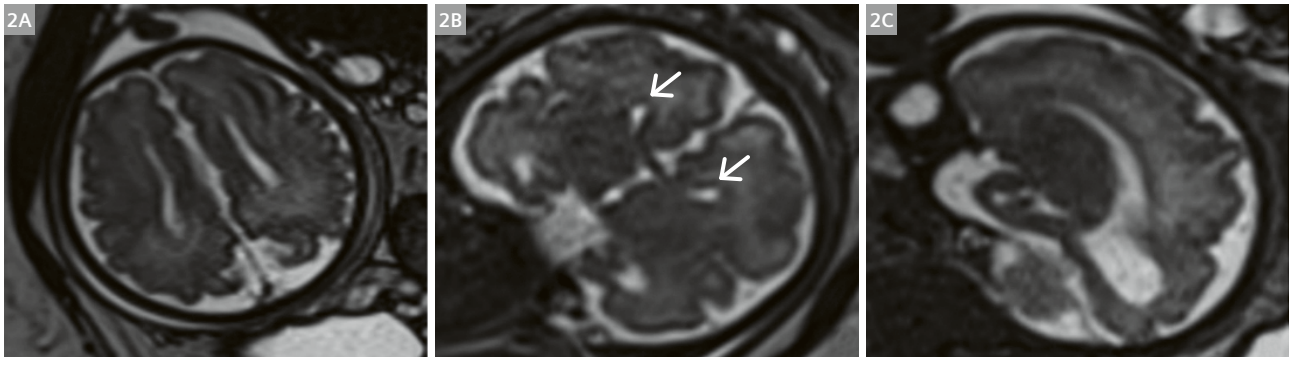

2 **Corpus callosum agenesis**
Sagittal HASTE **(2C)** shows complete absence of the corpus callosum. Axial TrueFISP **(2A)** shows parallel orientation of lateral ventricles. Coronal TrueFISP **(2B)** shows steer-horn-shaped frontal horns (arrows) resulting from the impression of Probst bundles.

1. **T2-weighted sequences**
   T2-weighted imaging (T2WI) includes single-shot, and half-Fourier single shot turbo spin echo (SSTSE, HASTE) T2-weighted sequences, and balanced sequences such as true fast imaging with steady-state precession (TrueFISP), which produces high tissue contrast and highlights the hyperintense amniotic fluid. At our institution, T2 HASTE and T2 TrueFISP were the most frequently used sequences for evaluating fetal anatomy. The TrueFISP sequence also allows vascular studies that require no intravenous contrast agent and can reveal hyperintense fetal vessels (vessels appear hypointense on SSTSE T1-weighted and T2-weighted images).

2. **T1-weighted sequences**
   T1-weighted imaging (T1WI), including 3D dual gradient echo (GRE), 2D fast spoiled GRE (FISP), and 3D liver acquisition and volume acquisition (3D VIBE), show less tissue contrast than T2WI sequences. T1WI sequences are primarily used to identify subacute bleeding, calcification, and lipoma, which appear as hyperintense loop structures in studies of congenital diaphragmatic hernia (CDH). T1WI sequences are also used to assess the presence and distribution of meconium, which enables accurate diagnosis of gastrointestinal abnormalities, reveals the size and location of the fetal liver, and can identify fetal, placental, or maternal hemorrhage.

3. **Susceptibility-weighted imaging**
   Susceptibility-weighted imaging (SWI) uses the intrinsic nature of local magnetic fields to enhance image contrast and thereby improve the visibility of various susceptibility sources and facilitate diagnostic interpretation [7]. It is worth mentioning that calcification is strongly diamagnetic and therefore decreases the magnetization in bone compared to the applied magnetic field. The technique results in a high contrast between bone and soft tissue, but a low contrast between different types of soft tissue. The low-signal bone is therefore easily distinguishable from the surrounding soft tissue.

4. **Diffusion-weighted imaging**
   As well as being used to diagnose cerebral infarction, diffusion-weighted imaging (DWI) sequences are currently being developed for fetal applications. The technique is already being used to study the maturity of lung parenchyma.

Fluid-sensitive short T1 inversion recovery (STIR), intravoxel incoherent motion imaging (IVIM), MR hydrography, and other sequences are not part of the routine fetal protocol but may be performed in specific cases where necessary.

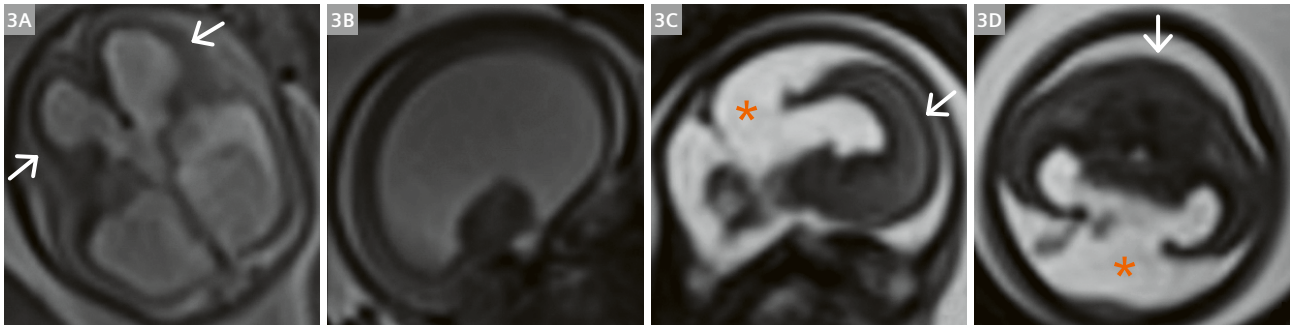

3 **Severe hydrocephalus (3A, B) and alobar holoprosencephaly (3C, D)**
Axial and coronal **(3A)** T2 HASTE imaging shows the marked dilation of the cerebral bilateral ventricle stenosis with only a thin mantle of overlying cerebral cortex (arrows). Sagittal **(3C)** and coronal **(3D)** T2 TrueFISP imaging shows only minimal frontal cerebral mantle (white arrows in 3A and B) and replacement of the majority of the brain with CSF (star). Coronal **(3C)** and axial **(3D)** T2 TrueFISP show a complete absence of falx, an interhemispheric fissure, and corpus callosum. Also visible is a horseshoe-shaped monoventricle communicating with a dorsal cyst (star).

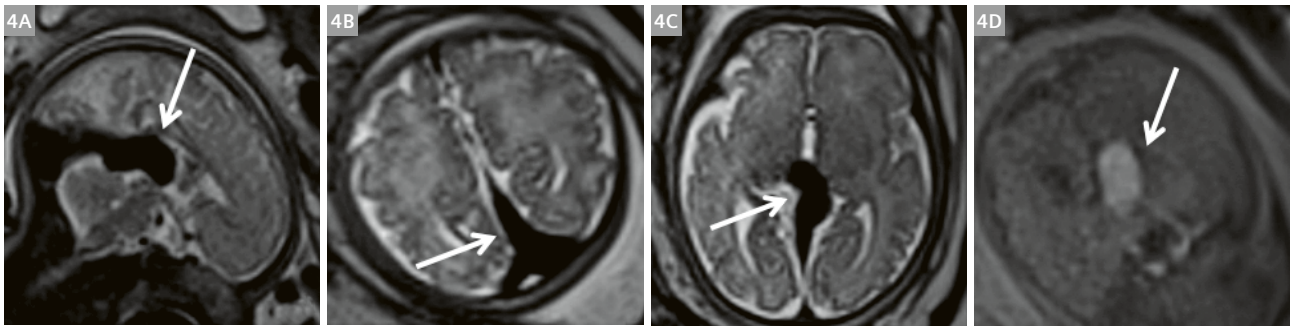

4 **Galen vein malformation**
Sagittal **(4A)** and coronal and axial **(4B)** T2 HASTE show a large varix (arrow) replacing the Galen vein, which exhibits hyperintensity on T1WI (**4D**, arrow).

The anatomy and anomalies in fetal MRI

Brain and spine

Imaging the central nervous system (CNS) anatomy and relevant pathology is clinically important for the early identification of cranial and spinal malformations and anomalous development. Fetal MRI has been shown to have higher contrast resolution and SNR than ultrasonography when it comes to illustrating the morphological changes in cranial and spinal brain abnormalities [8]. Most of the literature describing the results of MRI in large series of fetuses with CNS abnormalities deals with cerebral pathology. Spinal anomalies are usually described using examinations of smaller groups of patients or in case reports.

MR images of the developing fetal brain reflect changes in histogenesis and myelination. Subsequent changes are seen in the brain volume, surface configuration (sulcation), and internal configuration. Detailed information provided by MRI is necessary to evaluate the differentiation of white and gray matter, migration and myelination disorders, brain morphology and pathologies, and cranial posterior fossa and midline structures. Here, localizer brain scans (Fig. 1) provide the basis for images demonstrating different developmental deformities (Figs. 2–4).

The spinal canal and cord anomalies are among the CNS abnormalities which occur as a result of disruptions in formation and maturation. During the first three to five weeks of gestation (neurulation period), the neural tube, notochord, spine, and cranium develop. Disorders that occur at this stage of gestation (i.e., most spinal canal defects) are called "dorsal induction abnormalities". The dysraphic spinal canal and spinal cord disorders are divided into three groups: open dysraphic abnormalities, occult dysraphic abnormalities, and latent dysraphic abnormalities (e.g., diastematomyelia, hydromyelia, syringomyelia, dorsal dermoid sinus, teratoma, hamartoma, lipoma, dermoid/epidermoid cyst, and caudal regression syndrome).

Congenital anomalies of the spine occur at four to six weeks of gestation due to abnormal vertebral development that causes asymmetric growth of the spine. Anomalies in the ossification center of the fetal vertebral body result in bony defects such as hemivertebrae, butterfly vertebrae, and block vertebrae, which cause congenital scoliosis. MRI of fetuses diagnosed with osseous anomalies of the spine remains largely unexplored. Recently, we adapted and improved a clinically available SWI sequence for fetal spine imaging to evaluate vertebral malformations and anomalous vertebral development (in bony structures). We also typically used T2 TrueFISP and HASTE sequences to evaluate the recognition of the fetal spinal canal and spinal cord pathologies, as described in previous studies [9].

For MR imaging of the fetal spine, the protocol first involved a scout imaging sequence to gather information about the orientation of the fetus. Subsequent routine clinical sequences included T1WI, DWI, HASTE, T2-weighted TrueFISP, and SWI sequences. The HASTE, TrueFISP, and SWI sequences were obtained in the axial, coronal, and sagittal planes. The axial plane is best for assessing the neural arches, the coronal plane allows an additional assessment of the ribs and of pedicular widening in cases of spina bifida, and the sagittal plane is best for assessing the whole spine lengthways. The SWI sequence is best run immediately after routine HASTE or TrueFISP sequences, depicting the required anatomy by simply copying the slice parameters and thereby minimizing the time between sequences and reducing the chance of fetal motion. Here, localizer spine scans (Fig. 5) provide the basis for demonstrating various developmental deformities as follows (Figs. 5–9).

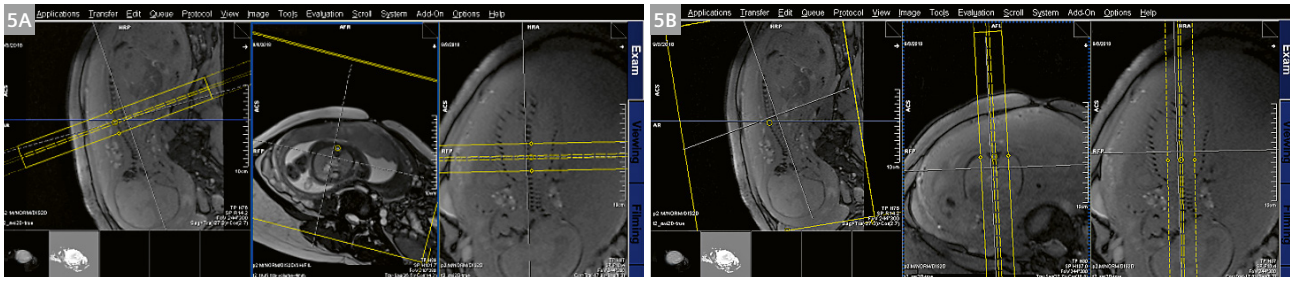

5 Axial, sagittal, and coronal localizer images of the fetal spine.

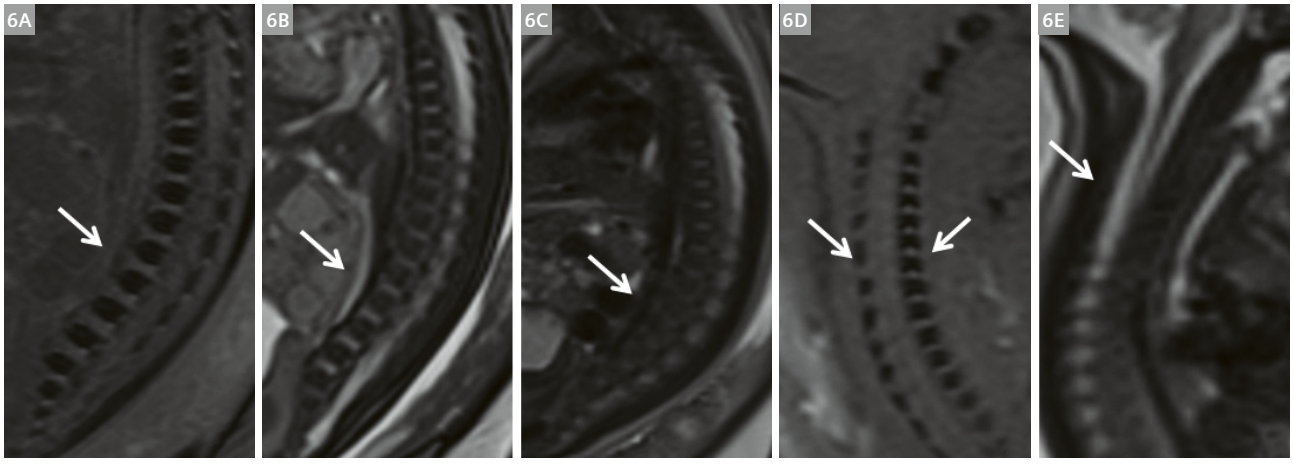

6 Images at 32 weeks' gestation (6A–C) and 26 weeks' gestation (6D–E) with normal fetal spine structures. Sagittal view of the thoracolumbar spine, MR images including SWI (6A), TrueFISP (6B), and HASTE (6C). The SWI **(6A, D)** clearly shows the vertebral bodies and the posterior elements (arrows). On a similar plane in the same position using TrueFISP **(6B, E)** and HASTE **(6C)**, the vertebral column (arrows) is shown poorly but could reveal the structures of the intraspinal canal.

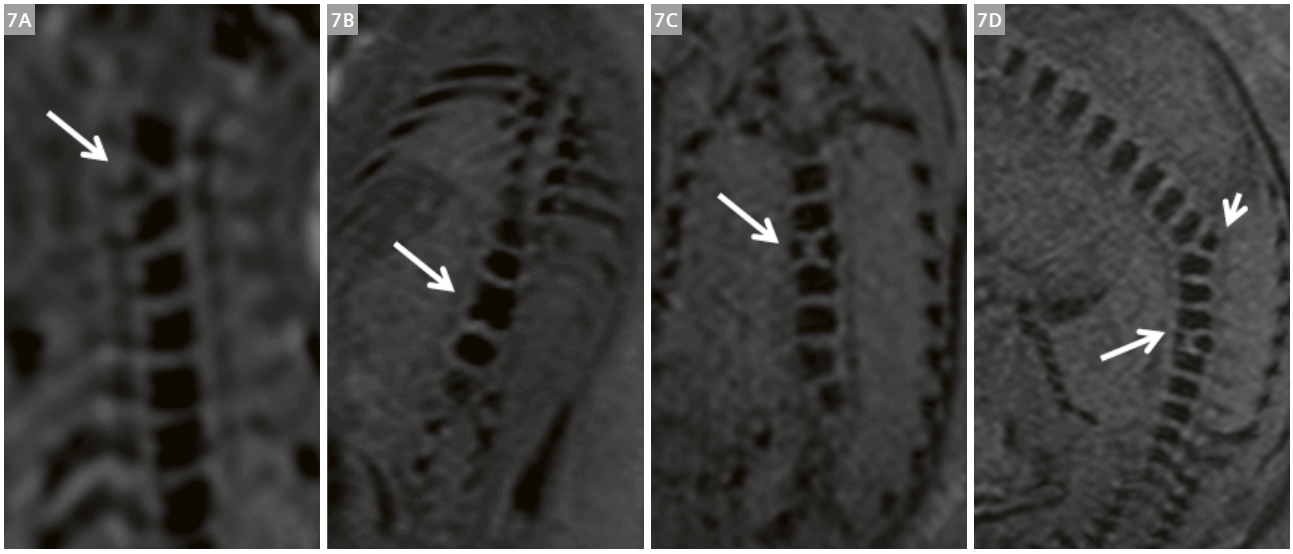

7 SWI images at 26 weeks' gestation (7A), 25 weeks (7B), 33 weeks (7C), and 34 weeks with fetal vertebral anomalies. Coronal views of the cervical **(7A)**, lumbar **(7B)**, and thoracic **(7C)** spine show hemivertebrae, block vertebrae, and butterfly vertebrae. Multiple vertebral anomalies with hemivertebrae (short arrows) and butterfly vertebrae (long arrows) are clearly visible in coronal 2D SWI **(7D)**.

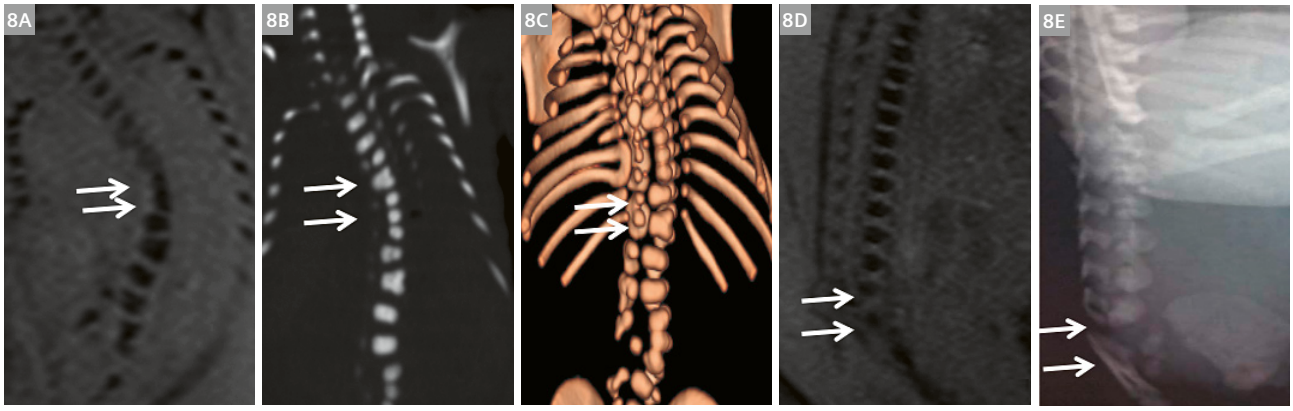

8 Images at 24 weeks' gestation (8A–E) with multiple vertebral anomalies (8A–C) and at 32 weeks' gestation (8D–E) with caudal regression syndrome. SWI **(8A)** shows multiple vertebral anomalies (arrows) that were consistent with the postmortem CT (**8B**, **C**, arrows). SWI shows dysplasia of the sacrococcygeal vertebrae (arrows) that was consistent with the postmortem X-ray (**8E**, arrows).

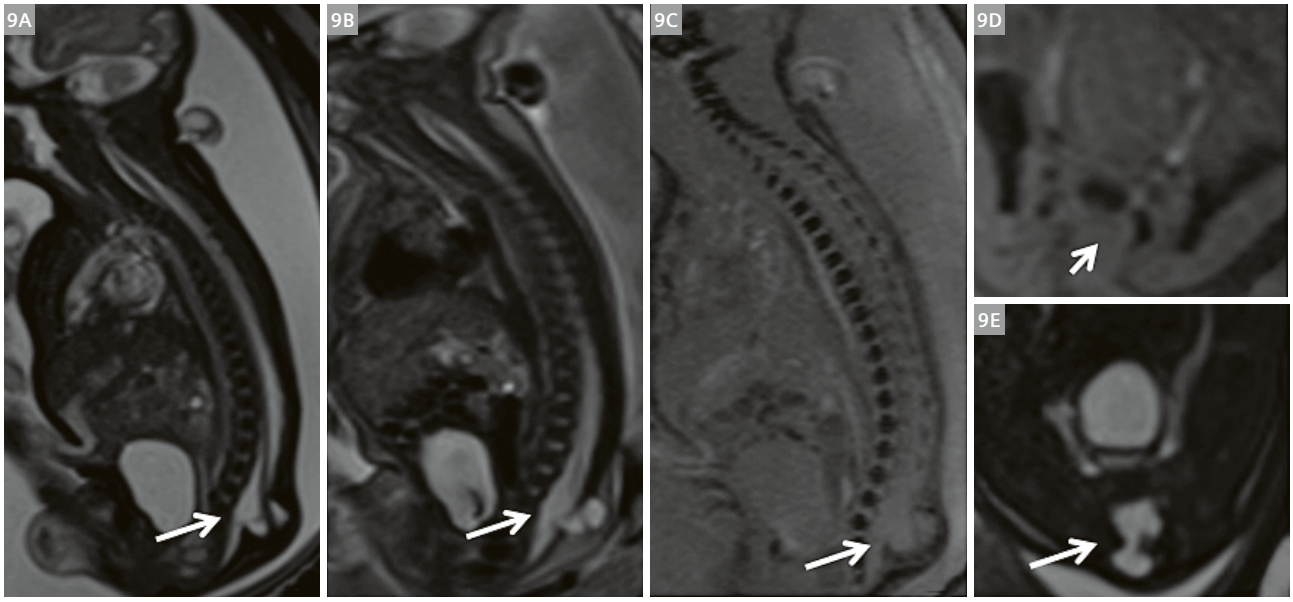

9 Images at 32 weeks' gestation with spinal dysraphism (9A–E). Sagittal view of the MR images include HASTE **(9A)**, TrueFISP **(9B, E)**, and SWI **(9C, D)**. The pocket-like processes protruding from the sacrococcygeal spinal canal were all visible, and the spinal cord was found to extend from the spinal canal to the dilated dural capsule (9A, B, E, long arrow), which could not be seen with SWI (9C, D). However, SWI showed excellent osseous spinal structures and demonstrates the pedicular widening (9C, long arrow; 9D, short arrow).

Chest

At present, ultrasound and MRI are the only diagnostic tools that can examine fetal lungs noninvasively. MRI provides additional biochemical and functional information that cannot be obtained by ultrasound as well as detailed structural information. This therefore makes it a valuable diagnostic adjunct for assessing fetal lung development [10]. Congenital chest malformations can range from small and asymptomatic entities to large, space-occupying masses that require immediate surgical treatment. An understanding of fetal chest masses is essential for appropriate monitoring during pregnancy, and for treatment recommendations and delivery management. The most common congenital chest anomalies include congenital cystic adenomatoid malformation (CCAM), congenital diaphragmatic hernia (CDH), bronchopulmonary sequestration (BPS), congenital hydrothorax, and congenital lobar emphysema. Less common entities include congenital high airway obstruction syndrome (CHAOS), congenital bronchogenic cyst, bronchial atresia, pulmonary arteriovenous malformation (PAVM), congenital pulmonary lymphangiectasia, pulmonary hypoplasia-aplasia, mediastinal teratoma, and mediastinal lymphangioma. These pulmonary abnormalities are not mutually exclusive; they frequently occur together as hybrid conditions.

The MRI sequences used to evaluate the fetal chest include HASTE, fast single-shot echo, and TrueFISP. In our unit, HASTE and TrueFISP images are the most useful for evaluating the lung anatomy. The lungs typically contain a significant amount of alveolar fluid, which is homogeneously hyperintense relative to the chest wall muscle on T2-weighted images.

Congenital diaphragmatic hernia and extralobar pulmonary sequestration were demonstrated as follows (Figs. 10, 11).

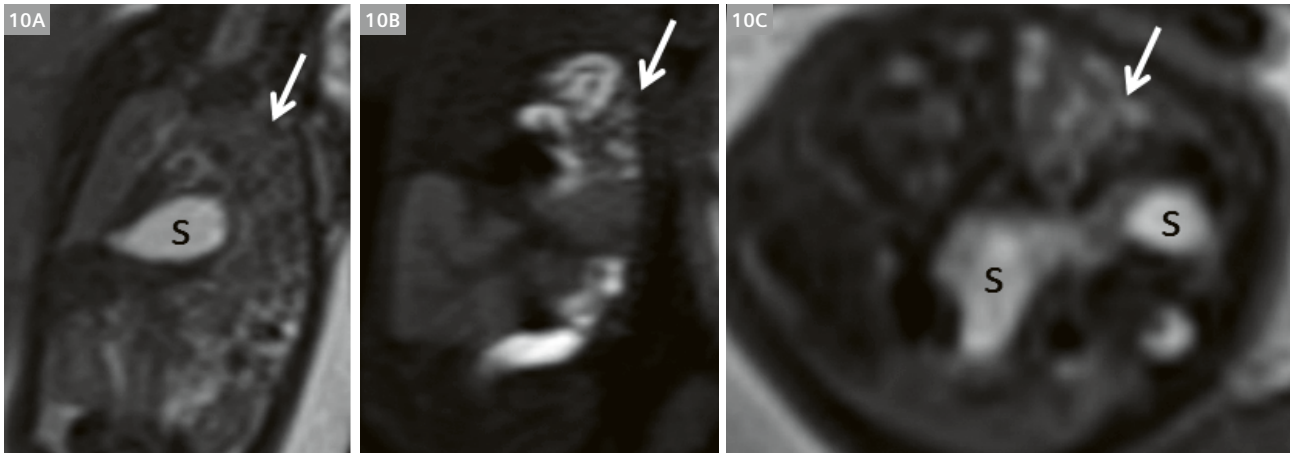

10 **Congenital diaphragmatic hernia at 28 weeks' gestation**
Coronal **(10A)** and axial **(10C)** T2 HASTE, and T1w imaging **(10B)** show herniated content (arrow) displacing the heart and compressing the unilateral lung and portions of the bowel (10B, arrow) and stomach (S) occupying the unilateral hemithorax.

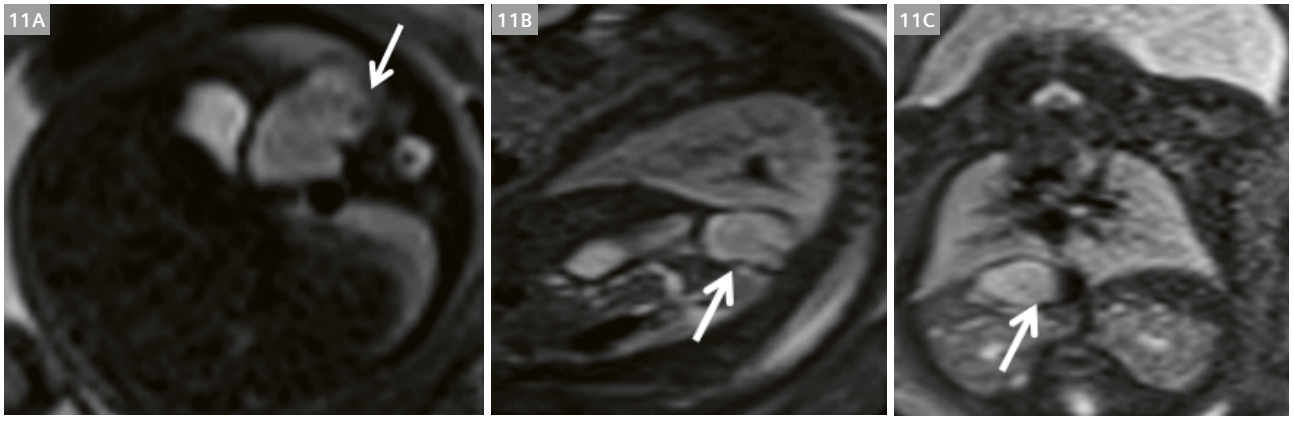

11 **Extralobar pulmonary sequestration at 32 weeks' gestation**
Axial **(11A)**, sagittal **(11B)**, and coronal **(11C)** T2 HASTE show a homogeneous, high T2WI signal between the left subphrenic space and left kidney with a clear boundary (arrow). Postnatal CT (not shown) enhancement shows a vascular shadow connected to the aorta.

Abdominal abnormalities and tumors

Fetal abdominal deformities and tumors vary in their location, and can be derived from the gastrointestinal tract, liver, kidney, and retroperitoneum. Congenital tumors are defined as those that are present during the fetal stage or at birth. In some cases, MRI can provide important information and even add important findings to prenatal US for perinatal management by visualizing fetal tumors with common tumor-related complications and other exceptional congenital abnormalities [11]. Common indications for fetal gastrointestinal (GI) MRI include suspected esophageal, small bowel, and large bowel obstruction, bowel malrotation, and bowel perforation resulting in meconium peritonitis or meconium pseudocyst. MRI is also particularly useful for evaluating rare GI abnormalities, such as megacystis microcolon intestinal hypoperistalsis syndrome (MMIHS), cloacal exstrophy, and cloacal malformation. Although US remains the modality of choice for investigating fetal anomalies, the findings are often nonspecific and may relate to transient normal variants [12]. In addition, urine and fluid in the colon beyond 24 weeks may have a similar sonolucent appearance on US and opposite appearances on MR images, allowing better identification and discrimination. In our department, a T1-weighted breath-hold sequence is completed in the coronal plane and, if necessary, in the sagittal and axial planes.

Different developmental deformities in the abdomen were demonstrated as follows (Figs. 12–16).

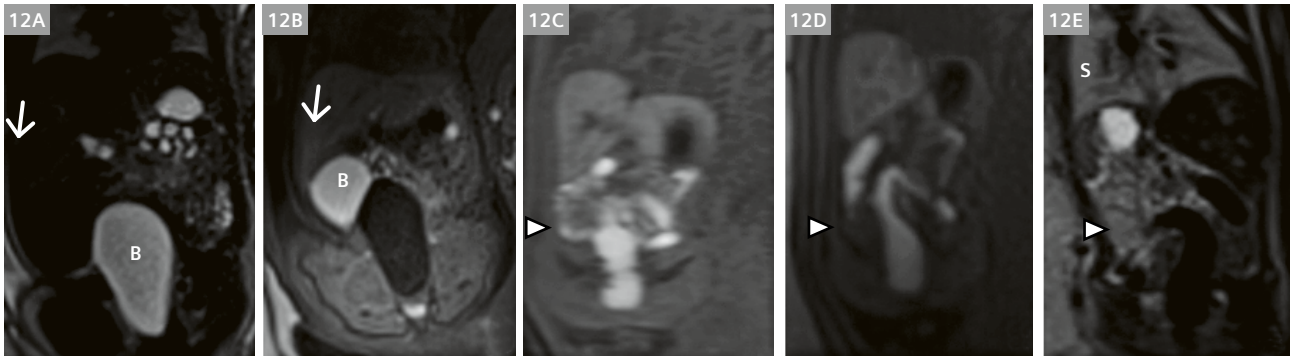

12 **Localized intestinal dilatation at 30+4 weeks' gestation, and imperforate anus at 28 weeks' gestation**
Coronal T2 HASTE **(12A)** and T1w **(12B)** images show the dilated loops of one part of the gastrointestinal tract. It is markedly hyperintense on T1WI (arrow) and hypointense on T2WI (arrow). Coronal T1WI **(12C, D)** and T2 TrueFISP **(12E)** images show a prominent rectum (arrowhead) with high T1 signal intensity and low T2 signal intensity. The abnormality of the large bowel was identified and diagnosed as rectal atresia during a postnatal physical examination. B = urinary bladder, S = stomach

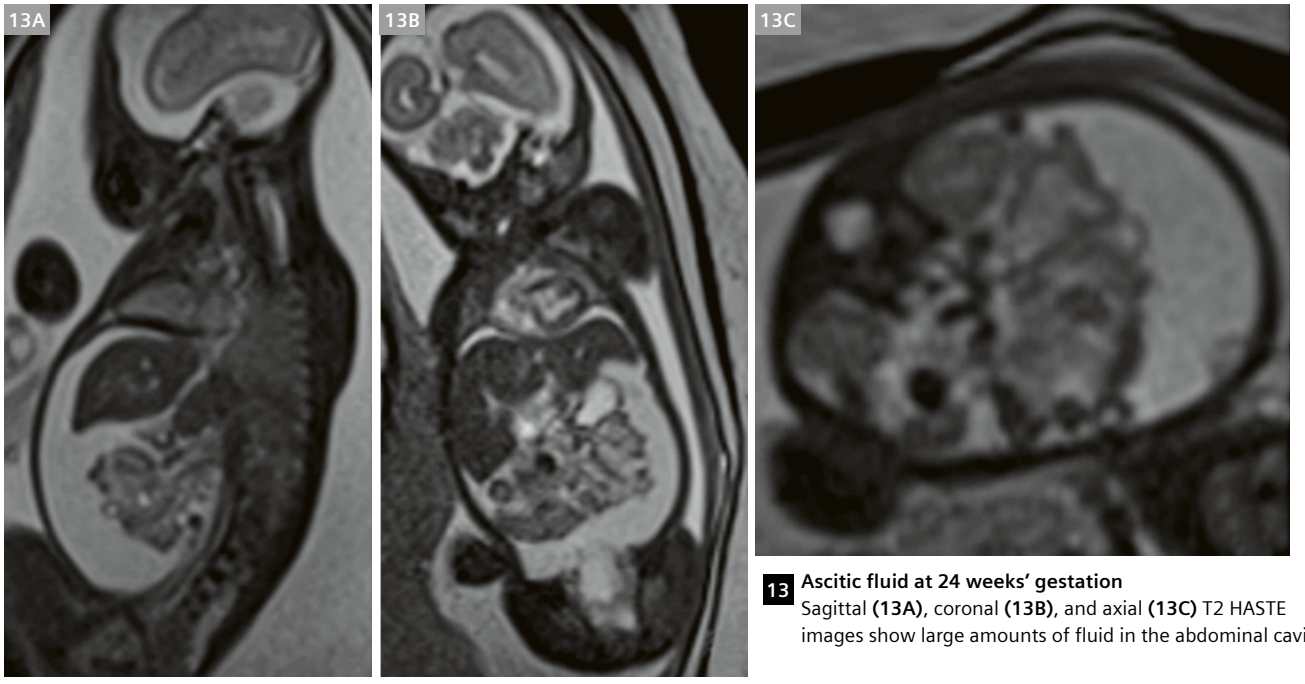

13 **Ascitic fluid at 24 weeks' gestation**
Sagittal **(13A)**, coronal **(13B)**, and axial **(13C)** T2 HASTE images show large amounts of fluid in the abdominal cavity.

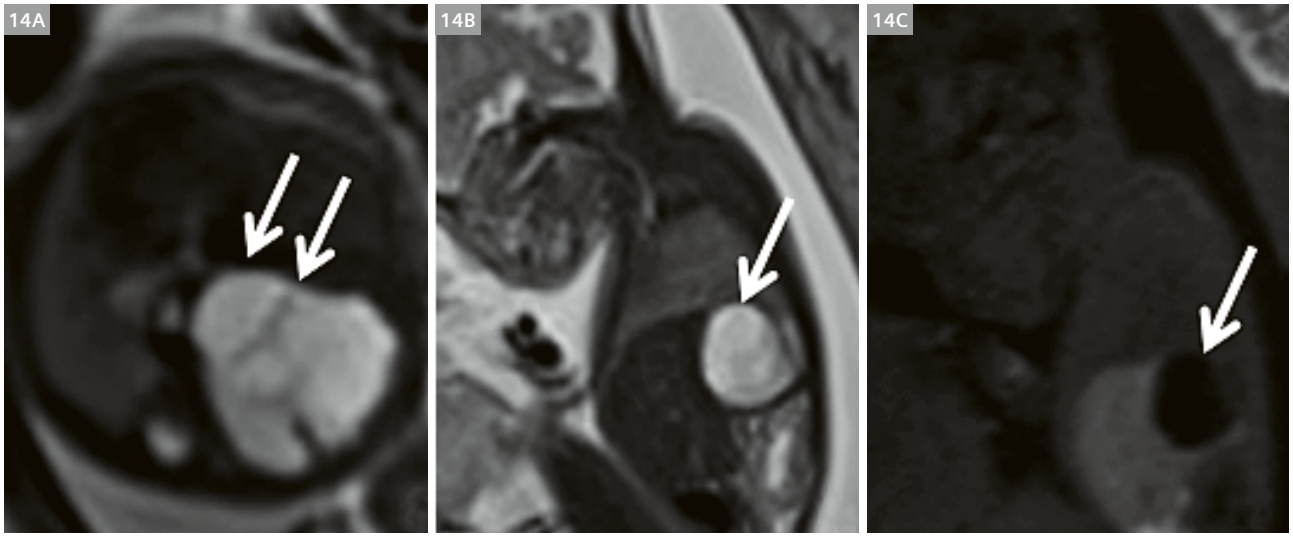

14 **Neuroblastoma at 28 weeks' gestation**
Axial **(14A)**, sagittal **(14B)**, and coronal **(14C)** T2 HASTE images show a solid mass with a clear boundary above a lateral kidney that is hyperintense on a T2-weighted sequence (arrow) and was found to be neuroblastoma after birth.

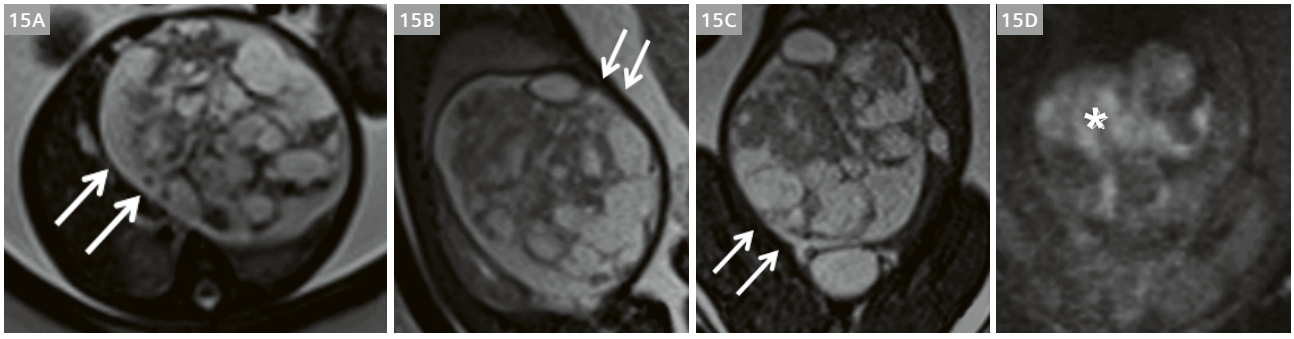

15 **Teratoid tumors at 30 weeks' gestation**
Axial T2 HASTE **(15A)**, sagittal **(15B)**, and coronal **(15C)** T2 TrueFISP images show a heterogeneous solid cystic mass with a high-intensity heterogeneous signal (arrows), and surrounding tissue that was markedly squeezed. The giant lesions showed restricted diffusion with DWI (**15D**, star). A histopathological diagnosis of teratoid tumors was made after birth.

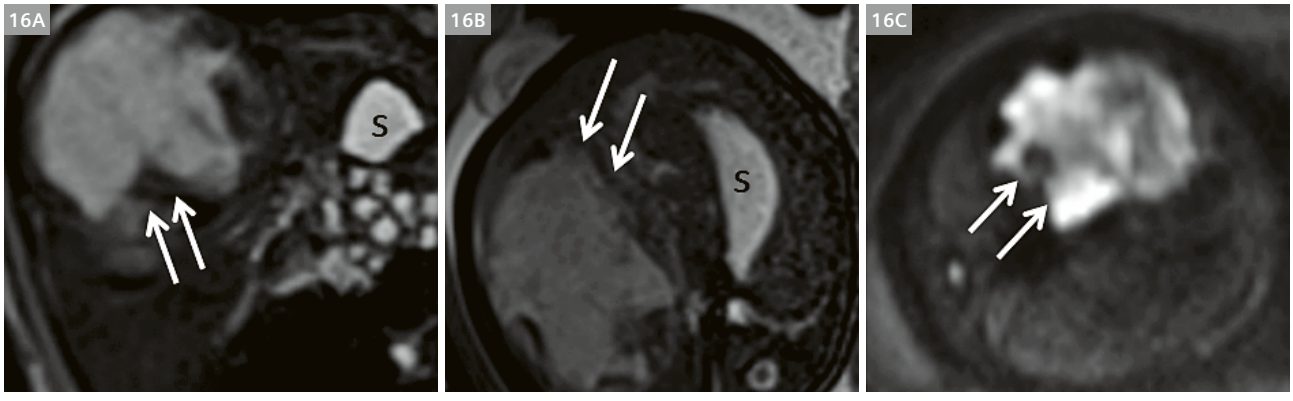

16 **Hepatic hemangioendothelioma at 32 weeks' gestation**
Coronal T2 HASTE **(16A)** and axial T2 TrueFISP **(16B)** images show a large heterogeneous and high-signal mass in the liver parenchyma, and highly restricted diffusion with DWI **(16C)**. A histopathological diagnosis of hepatic hemangioendothelioma was made after birth.

Maternal indications for prenatal MRI

In addition to fetal indications, there are several maternal indications for prenatal MR imaging. They include the possibility of uterine rupture, the need to differentiate between placenta accreta and percreta, a large myoma interfering with the pregnancy, and MR pelvimetric measurements. In our unit, the technique of placental MRI and the diagnostic level are increasingly convincing and compelling.

Abnormal invasive placenta (AIP) is a disease with a spectrum of severity characterized by abnormal, firmly adherent placental implantation into the uterus at varying depths. It is typically referred to as placenta accreta, increta, and percreta [13]. When AIP occurs, the placenta may not be completely separated from the uterus at the time of delivery, resulting in potentially life-threatening intrapartum or postpartum massive hemorrhage and associated morbidity such as multisystem organ failure, disseminated intravascular coagulation, and even death. Placenta percreta (PP) is the most dangerous type of AIP. It is characterized by trophoblasts fully penetrating the myometrium and in some cases extending to or breaching the serosa and even invading surrounding structures [14]. An accurate prenatal diagnosis of PP is therefore imperative.

In 2017, our team published an article on placenta accreta [15] that aimed to identify specific MRI features for differentiating PP from placenta accreta (PA), and to characterize the features of invasive placenta previa. Our studies showed a series of MRI features, including myometrial thinning, interrupted myometrium, loss of the placental-myometrial interface, marked placental heterogeneity, dark intraplacental bands, abnormal intraplacental vascularity, abnormal uterine bulge, placental bulge (type I and type II, Fig. 2), uterine serosal hypervascularity, bladder wall nodularity, and extrauterine placental extension. Our results suggest that type II placental bulge and uterine serosal hypervascularity are useful MRI features for differentiating PP from PA. Profoundly abnormal vessels are associated with greater blood loss during caesarean section. Our results could contribute to accurate prenatal diagnosis of PP and help minimize the risk of massive hemorrhage [15].

In our center, all the patients with suspected invasive placenta previa (IPP) were imaged in the supine or left-lateral position with bladders moderately full. T2-weighted HASTE and T2-weighted TrueFISP images were obtained without breath-hold in the axial, coronal, sagittal, and oblique sagittal planes. Additional imaging planes perpendicular to the placenta-uterus interface or uterus-bladder interface were obtained in the region of the suspected AIP.

Several placenta increta and placenta percreta were demonstrated as follows (Figs. 17–20).

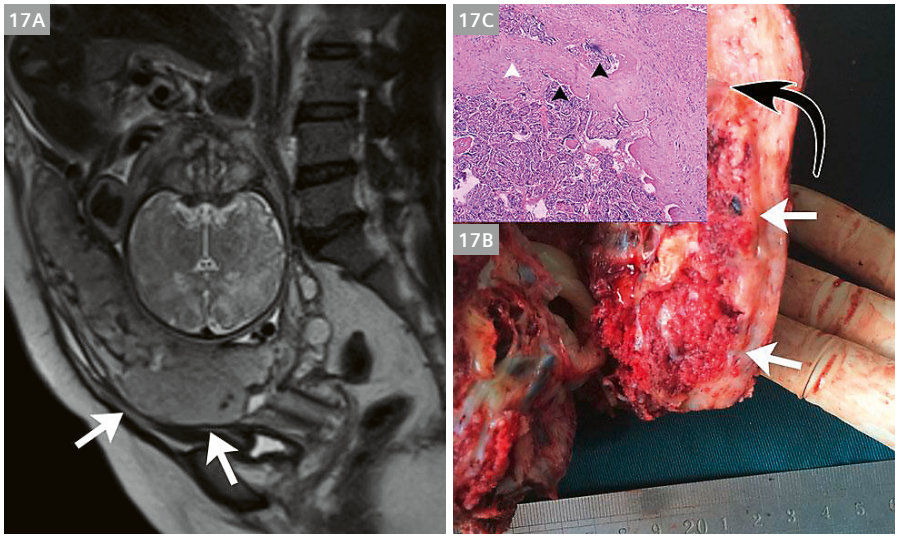

17 Placenta increta (PI) in a 40-year-old woman at 35 weeks' gestation A sagittal T2 HASTE MR image **(17A)** demonstrates type I placental bulge (white arrows) with an intact uterine outline. A photograph **(17B)** of gross specimens after hysterectomy shows that the placenta has invaded the myometrium (white arrows) with intact uterine serosa, consistent with PI. A photomicrograph (**17C**, magnification x 400, hematoxylin and eosin stain) shows chorionic villi (black arrowheads) implanted in the myometrium (white arrowhead), consistent with PI.

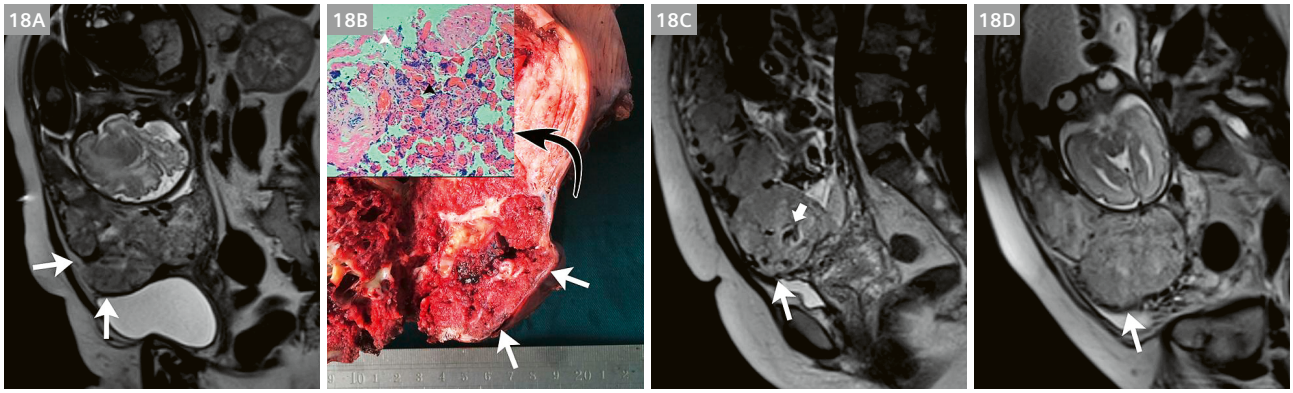

18 **Placenta percreta (PP, 18A, B) in a 39-year-old woman at 30 weeks' gestation**
A sagittal T2 HASTE MR image **(18A)** shows type II placental bulge (white arrows) protruding from the uterine outline. A photograph **(18B)** of gross specimens after hysterectomy shows placental invasion (white arrows) through the uterine wall, consistent with PP. A photomicrograph (magnification: x 400, hematoxylin and eosin stain) shows chorionic villi (black arrowhead) penetrating the myometrium (white arrowhead), consistent with PP. Sagittal T2 HASTE MR images show a type IIa placental bulge (long arrow, a focal outward bulge protruding from the uterine outline) with bridging vessels (short arrow) in a 31-year-old woman at 35 weeks' gestation with PP **(18C)** and type IIb placental bulge (long arrow) without bridging vessels in a 29-year-old woman at 32 weeks' gestation with PP **(18D)**.

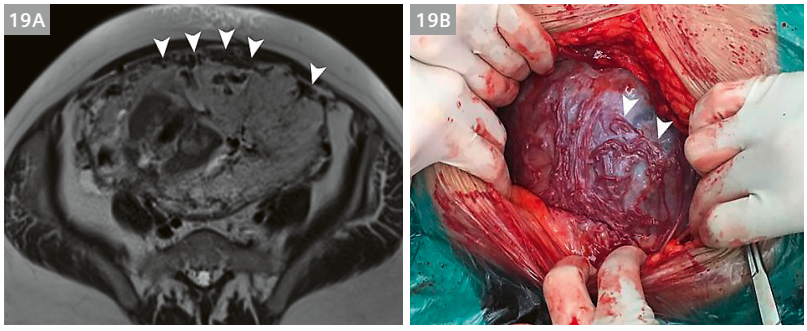

19 **Placenta percreta (PP) in a 35-year-old woman at 29 weeks' gestation**
An axial T2 HASTE image **(19A)** shows uterine serosal hypervascularity (arrowheads, tortuous and closely packed vessels along the uterine serosa) in the lower uterine segment.
A photograph **(19B)** taken during cesarean delivery shows the tortuous abnormal vessels in the uterine serosa (arrowheads), consistent with their appearance on MR images.

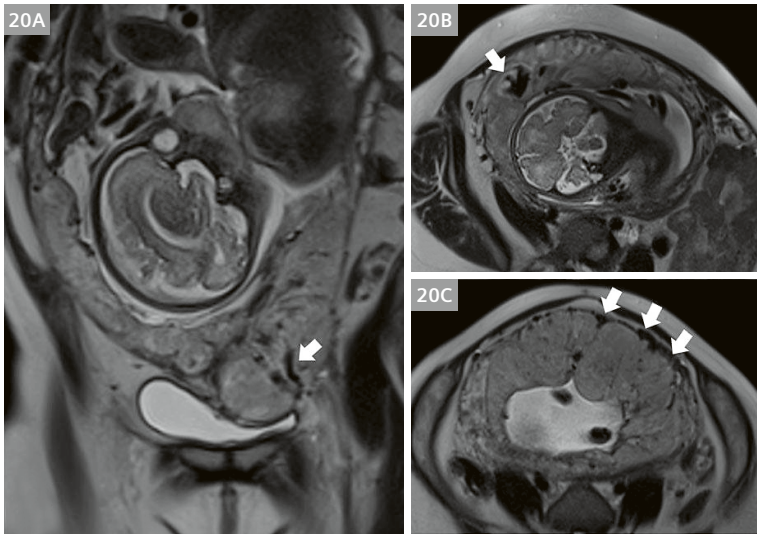

20 A coronal T2 HASTE MR image **(20A)** shows bridging vessels (arrow) through the bulging placenta in a 25-year-old woman at 32 weeks' gestation with placenta percreta (PP). An axial T2 HASTE MR image **(20B)** shows abnormal intraplacental vascularity (arrow) in a 28-year-old woman at 30 weeks' gestation with placenta increta (PI). An axial T2 HASTE MR image **(20C)** demonstrates uterine serosal hypervascularity (arrows) in a 34-year-old woman at 35 weeks' gestation with PP.

As outlined in this article, fetal MR imaging is playing an increasingly important role in prenatal diagnostics. Nevertheless, US will and should remain the first choice for prenatal screening due to its low cost, ease of availability, and superb safety profile. Advances in fetal MRI have given clinicians powerful tools to identify fetal pathologies. These can range from small and symptomatic abnormalities to large, space-occupying masses that require immediate surgical treatment. The information obtained with fetal MR imaging can be helpful and allow early planning of prenatal management.

References

1 Weisstanner C, Gruber GM, Brugger PC, et al. Fetal MRI at 3T – ready for routine use? Br J Radiol. 2017; 90(1069):20160362.
2 Prayer D, Brugger PC. Investigation of normal organ development with fetal MRI. Eur Radiol. 2007; 17(10):2458-2471.
3 Haacke EM, Xu Y, Cheng YC, et al. Susceptibility weighted imaging (SWI). Magn Reson Med. 2004; 52(3):612-618.
4 Reichenbach JR, Jonetz-Mentzel L, Fitzek C, et al. High-resolution blood oxygen-level dependent MR venography (HRBV): a new technique. Neuroradiology 2001; 43(5):364-369.
5 Robinson AJ, Blaser S, Vladimirov A, et al. Foetal "black bone" MRI: utility in assessment of the foetal spine. Br J Radiol. 2015; 88(1046):20140496.
6 Smith FW, Adam AH, Phillips WD. NMR imaging in pregnancy. Lancet. 1983; 1(8314-5):61-62.
7 Reichenbach JR, Venkatesan R, Schillinger DJ, et al. Small vessels in the human brain: MR venography with deoxyhemoglobin as an intrinsic contrast agent. Radiology. 1997; 204(1):272-277.
8 Coakley FV, Glenn OA, Qayyum A, et al. Fetal MRI: a developing technique for the developing patient. AJR Am J Roentgenol. 2004; 182(1):243-252.
9 Duczkowska A, Bekiesinska-Figatowska M, Herman-Sucharska I, et al. Magnetic resonance imaging in the evaluation of the fetal spinal canal contents. Brain Dev. 2011; 33(1):10-20.
10 Kasprian G, Balassy C, Brugger PC, et al. MRI of normal and pathological fetal lung development. Eur J Radiol. 2006; 57(2):261-270.
11 Nemec SF, Horcher E, Kasprian G, et al. Tumor disease and associated congenital abnormalities on prenatal MRI. Eur J Radiol. 2012; 81(2):e115-e122.
12 Veyrac C, Couture A, Saguintaah M, et al. MRI of fetal GI tract abnormalities. Abdom Imaging. 2004; 29(4):411-420.
13 Belfort MA. Placenta accreta. Am J Obstet Gynecol. 2010; 203(5):430-439.
14 Silver RM, Barbour KD. Placenta accreta spectrum: accreta, increta, and percreta. Obstet Gynecol Clin North Am. 2015; 42(2):381-402.
15 Chen X, Shan R, Zhao L, et al. Invasive placenta previa: Placental bulge with distorted uterine outline and uterine serosal hypervascularity at 1.5T MRI – useful features for differentiating placenta percreta from placenta accreta. Eur Radiol. 2018; 28(2):708-717.

Contact

Guangbin Wang
Department of MR
Shandong Medical Imaging Research Institute
Shandong University
324, Jingwu Road, Jinan
Shandong 250021
China
wgb7932596@hotmail.com

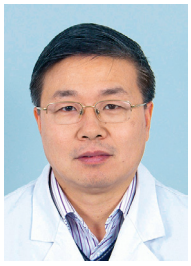

Guangbin Wang

Xianyun Cai

GOBrain 5-Minute MRI in Children: Shown to Reduce the Need for Sedation

Nadja Kadom, M.D.[1,2]; Anna Trofimova[1], M.D.

[1] Emory University School of Medicine, Department of Radiology and Imaging Sciences, Atlanta, GA, USA
[2] Children's of Atlanta (CHOA-Egleston), Department of Radiology, Atlanta, GA, USA

Abstract

Shorter MR imaging protocols can be very valuable in pediatrics[1], specifically when they reduce the need for sedation. In a pilot assessment of children under the age 8 years undergoing a 5-minute brain MR for primary headache, we found that the need for sedation was reduced by 70%. A current barrier to wide adoption of this imaging protocol is the lack of data directly comparing diagnostic quality between a 5-minute brain MRI protocol and a conventional MRI brain protocol.

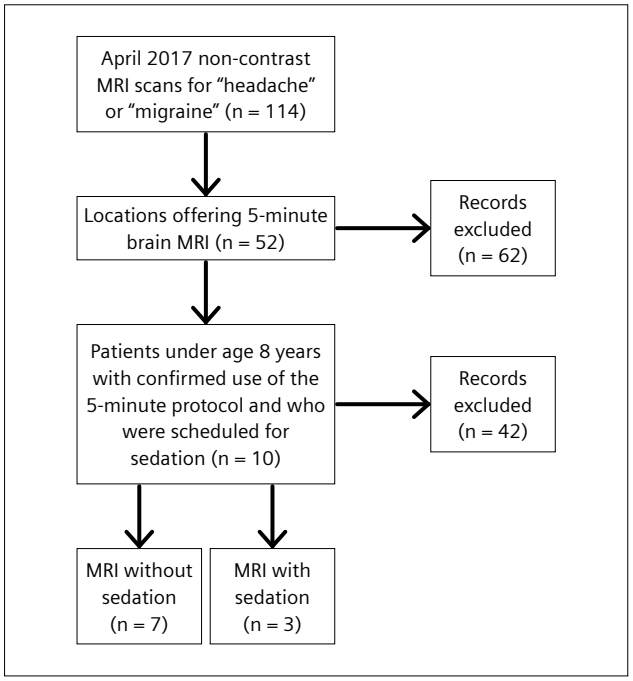

1 Study setup.

Background

The number of MRI studies requiring sedation in children increases at a rate of 8.5% annually, slightly exceeding the growth rate of CT and MRI imaging studies (8.1%) [1]. While sedation of children for imaging studies has been shown to be extremely safe, there has been some concern regarding potential neurotoxicity of certain anesthetics [2]. Sedation also adds cost to an MRI study, driving up health care expenses for individuals and for society [2]. From the patient and family perspective, use of sedation signifi-cantly increases the amount of time spent at the imaging facility and children may experience side effects post-sedation, such as motor imbalance, gastrointestinal symptoms, agitation, and restlessness [3].

Several strategies have been proposed to decrease the use of sedation in children. Child-life specialists can coach patients through MRI exams without sedation, but this may require training on 'mock' scanners, which are expen-sive and not widely available. Child-life coaching may lead to frequent interruptions during the scan, which could disrupt the MRI schedule. Video and audio technologies have been successful in serving this purpose and resulted in up to 45% decrease in sedation utilization [4]. In infants, feeding and bundling can be used to reduce motion artifacts, although this could result in overheating and respiratory compromise [5].

Here, we collected pilot data on using a 5-minute brain MRI protocol and its effect on the need for sedation in children with presumed primary headaches under the age of 8 years.

[1] *MR scanning has not been established as safe for imaging fetuses and infants less than two years of age. The responsible physician must evaluate the benefits of the MR examination compared to those of other imaging procedures. Note: This disclaimer does not represent the opinion of the authors.*

Material and methods

The pilot assessment was performed at a freestanding pediatric hospital that serves as a level I trauma center. We used a software application (Montage Health Solutions Inc, Philadelphia, PA, USA) to search radiology reports for any patients with an imaging indication containing the words "headache" or "migraine" and who underwent a non-contrast brain MRI. The study period was April 1–30, 2017. We excluded any patients 9 years or older assuming that they would be able to undergo MRI brain imaging without sedation. We also excluded two locations within our health care system that do not offer the 5-minute brain MRI protocol. We included only patients in whom we could confirm that the 5-minute brain MRI protocol had been used. For patients meeting inclusion criteria, we checked the medical records to determine whether they were scheduled as a sedated MRI and whether they were completed as a sedated or a non-sedated MRI.

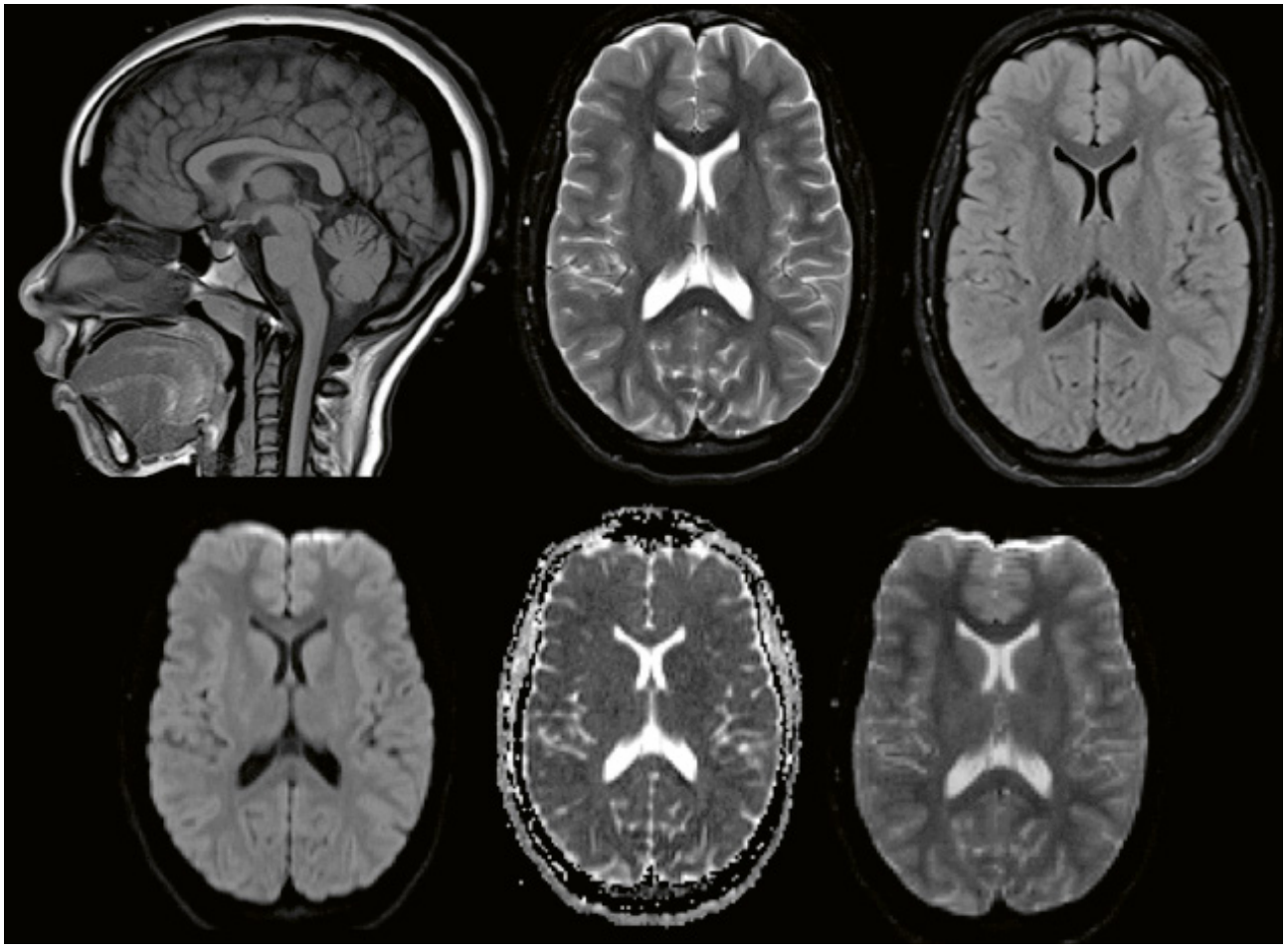

2 GOBrain 5-minute protocol.

Results

In the study period April 1–30, 2017 we found 114 non-contrast brain MRI studies done for indications containing the words "headache" or "migraine", 52 were done at locations that offer the 5-minute brain MRI protocol, and, of these, there were 10 patients under the age of 8 years in whom we confirmed that the 5-min brain protocol was used and who were scheduled to undergo the MRI with sedation. Of these, 7 were able to complete the MRI without sedation and 3 patients were imaged with sedation (Fig. 1). The percentage of patients converted to a non-sedated exam was 70% (7/10), which equals 6% of the entire cohort (7/114).

Discussion

By using the GOBrain 5-minute protocol we were able to reduce the number of sedated MRI's in the target cohort by 70%. This effect is stronger than the 45% reduction that can be achieved through use of audio-visual distraction. There is potential for increasing the cohort that can benefit from the GOBrain 5-minute protocol by > 50% if this protocol was offered at other locations within our network. While the focus of this pilot data assessment was to observe the impact of a 5-minute brain MRI protocol on sedation requirements, we observed other benefits: given that the MRI slots are still 30 minutes long, the conversion of a full brain MRI to a 5-minute protocol opened up time on the MRI schedule that could be used for inpatient imaging or catching up on schedule delays.

The image quality of the 5-minute protocol was good (Fig. 2), but may not meet diagnostic quality standards for certain imaging findings. For example, small parenchymal lesions or small blood products may not be as readily visible given the constraints of the image acquisition in order to achieve short scan times. For this reason, we are limiting the use of this MRI protocol to a patient cohort with "headache" or "migraine" as the sole indication, where most patients are presumed to be screened in the setting of a primary headache with low probability of underlying structural pathology of the brain. Future studies will be needed to compare the diagnostic perfor-mance of short MRI protocols in direct comparison to MRI protocols with conventional exam length.

Contact

Nadja Kadom, M.D.
Director of Pediatric Neuroradiology, Children's Healthcare of Atlanta (Egleston)
Associate Professor, Emory University School of Medicine
Department of Radiology and Imaging Sciences
1405 Clifton Rd NE
Atlanta, GA 30322
USA
Cell/text: +1 703 585 6554
nkadom@emory.edu

Nadja Kadom

Dr Anna Trofimova

Acknowledgement

We would like to thank the MRI technologists at CHOA-Egleston and CHOA-Towncenter for their help with data collection and for their enthusiasm and engagement towards the goal of minimizing sedation for children, without compromising the quality of care: Nicole Chin, Melissa Weisel, Jennifer Bagley, and Shane Stewart.

References:

1 Wachtel RE, Dexter F, Dow AJ (2009) Growth rates in pediatric diagnostic imaging and sedation. Anesth Analg 108:1616–1621.
2 Barton K, Nickerson JP, Higgins T, Williams RK. Pediatric anesthesia and neurotoxicity: what the radiologist needs to know. Pediatr Radiol. 2017 May 3.doi: 10.1007/s00247-017-3871-4. [Epub ahead of print] Review. PubMed PMID: 28470388.
3 Malviya S, Voepel-Lewis T, Prochaska G, Tait AR. Prolonged recovery and delayed side effects of sedation for diagnostic imaging studies in children. Pediatrics. 2000 Mar;105(3):E42. PubMed PMID: 10699144.
4 Khan JJ, Donnelly LF, Koch BL et al (2007). A program to decrease the need for pediatric sedation for CT and MRI. Appl Radiol 36:30–33.
5 Antonov NK, Ruzal-Shapiro CB, Morel KD, Millar WS, Kashyap S, Lauren CT, Garzon MC. Feed and Wrap MRI Technique in Infants. Clin Pediatr (Phila). 2016 Nov 20. pii: 0009922816677806. [Epub ahead of print] PubMed PMID: 27872353.

The results by the Siemens' customer described herein are based on results that were achieved in the customer's unique setting. Since there is no "typical" hospital and many variables exist (e.g., hospital size, case mix, level of IT adoption) there can be no guarantee that other customers will achieve the same results.

MAGNETOM Altea with BioMatrix

Confidence to deliver

siemens-healthineers.com/altea

Scan up to 50 % faster in clinical routine[1]

MAGNETOM Altea is the new 1.5T Open Bore system that gives you full confidence to deliver the productivity, reproducibility, and patient satisfaction that you demand in MRI. Powered by our premium MR technology, MAGNETOM Altea combines our unique BioMatrix technology, the new *syngo* MR XA software platform, and our exclusive Turbo Suite to fundamentally transform care delivery.

[1] *Data on file.*

SIEMENS Healthineers

Musculoskeletal and Body MRI in Children

Sarah D. Bixby, M.D.; Reid C. Nichols, RT (R) MR; Ali Gholipour, Ph.D.

Department of Radiology, Boston Children's Hospital, Boston, MA, USA

MRI imaging in pediatric patients is as much about the process as it is about the result. While high-quality images are the ultimate goal, for children an imaging study is a success if diagnostic images are obtained while minimizing the risk to the patient, which includes reducing the risk of anesthesia [1–2]. There are many ways to improve spatial resolution and gain signal-to-noise ratio (SNR) in MRI, though most strategies cost time. In clinical practice there are limitations on patient cooperation and magnet utilization that require a practical approach to imaging. While working with children is enormously satisfying, there are also challenges that come with pediatric imaging which require minimizing exam times, eliminating labor-intensive breath-holding instructions, and imaging through motion (respiratory and gross motion). Motion is a major obstacle when it comes to imaging young children. In many instances, the difference between a non-diagnostic exam and a successful exam may simply require reducing sequence time by half. While this used to require unacceptable compromise in image quality, this is no longer true. With increased field strength magnets (i.e. 3T), appropriate selection of multichannel phased array coils, and parallel imaging techniques, scan times have decreased considerably from where they started. With a few additional strategies it is not only possible, but more than likely that a complete exam can be performed in a young child[1] without sedation.

Advanced protocol planning, sequence prioritization, real-time exam monitoring, and skilled patient handling are also critical elements of a successful MRI examination in a young child.

A fundamental principle in imaging pediatric patients is to limit sequences to only those that are necessary, acquiring the most high yield sequences first. Patient cooperation is limited and young patients often have tolerance for two or three sequences. Radiologists should assume the most critical diagnostic information must be obtained in the first ten minutes of an exam. If those first sequences are diagnostic, the patient will be spared a follow-up exam under anesthesia. MRI is increasingly being used to screen patients with certain symptoms for presence or absence of disease, such as fracture detection in limping toddlers, evaluation for infection in children with fever of unknown origin, or appendicitis screening in patients with right lower quadrant pain. MRI may be the best means of detecting fractures in certain locations when the bones have not yet ossified (Fig. 1), and for localizing disease when patients are unable to verbalize symptoms.

[1] *MR scanning has not been established as safe for imaging fetuses and infants less than two years of age. The responsible physician must evaluate the benefits of the MR examination compared to those of other imaging procedures. Note: This disclaimer does not represent the opinion of the authors.*

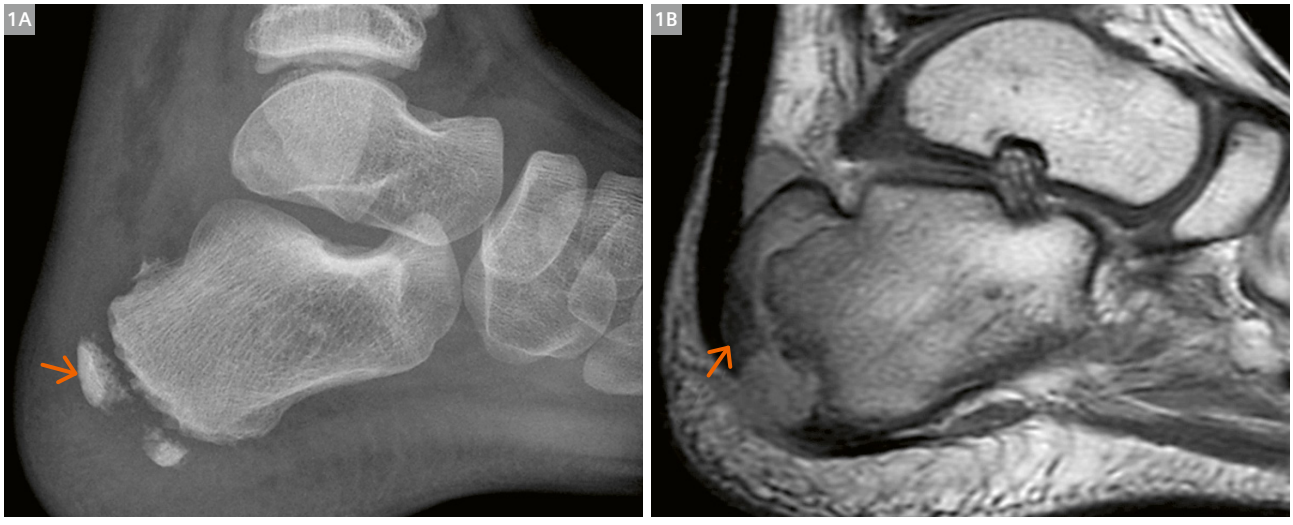

1 6-year-old female with calcaneal apophyseal fracture **(1A)** Lateral radiograph of the ankle reveals a normal-appearing apophysis (orange arrow). **(1B)** Sagittal PD-weighted TSE sequence reveals avulsion of the calcaneal apophysis, not appreciated on radiographs secondary to the lack of ossification.

It is more important to acquire images quickly to allow actionable diagnosis, rather than spending additional time enhancing imaging quality at the expense of patient cooperation.

Monitoring MRI examinations in real-time allows for adjustment of imaging parameters as the study unfolds [3]. As toddlers are often unable to articulate the location and nature of their symptoms, imaging requires looking far and wide initially and focusing down on an abnormality once identified. Setting up an MRI in a toddler with an unexplained limp, for example, often requires using one or more body matrix coils (depending on the child) to perform initial sequences with a large field of view (FOV) from the pelvis to the feet (Fig. 2). These sequences can be performed quickly, with need for additional sequences determined by the presence or absence of abnormal findings. Without real-time radiologist supervision, these protocol modifications would not be possible and the examination may need to be repeated.

While vigilant exam monitoring, careful protocoling, and adept patient handling are critical to successful imaging of children, these efforts may still fall short of the goal without additional sequence advancements. Accelerated acquisitions and motion robust sequences are, therefore, particularly valuable in pediatric imaging. Acceleration techniques allow for substantial reductions in imaging times so that they may be tolerated by young patients; in our experience this generally means shorter than two minutes per sequence. In pediatric musculoskeletal imaging, MRI protocols rely heavily on turbo spin-echo (TSE) sequences which include proton density (PD), intermediate weighted (IW), and T2-weighted images. Accelerated TSE acquisitions can be obtained through *k*-space undersampling in parallel imaging [4]; however a reduction or acceleration factor of R comes with a reduction of $1/\sqrt{R}$ in (SNR). In addition, SNR is also reduced by the noise amplification factor, or the *g*-factor (geometry factor) penalty that varies by the location in an image depending on the number of aliased replicates per voxel based on coil sensitivities [5]. The *g*-factor penalty depends on the receive coil design and coverage, and the geometry of imaging and can vary between 1 and 2 across the image. Simultaneous multi-slice (SMS) is another technique to accelerate imaging that excites multiple spatially distributed slices simultaneously by using a multi-band radiofrequency pulse and techniques to control aliasing and reduce the *g*-factor penalty [5–11]. Data obtained from receive coils from simultaneously excited slices are separated to reconstruct images. When parallel imaging and SMS are both applied, imaging times can be reduced 4- to 8-fold over traditional methods. In our routine knee MRI protocol we compared an accelerated T2-weighted TSE sequence using a parallel imaging iPAT factor of 2 with an SMS factor of 2 to achieve 4-fold acceleration against our traditional sequence without the SMS acceleration (Figs. 3, 4). We found both the SMS TSE and the TSE were equivalent in identifying pertinent imaging findings [12]. Compared to the traditional sequence, the SMS accelerated sequence is nearly twice as fast (Table 1). Further reduction in imaging time can be gained by increasing the SMS factor, with incremental cost to SNR. In our patient population we found that 4-fold acceleration is sufficient for most patients, and additional acceleration can be reserved for patients who are extremely nervous or fidgety, given the modest reduction in SNR.

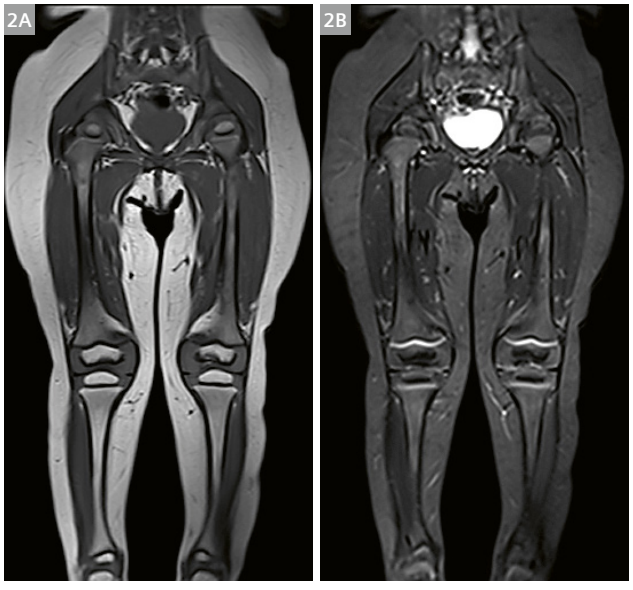

2 2-year-old female with limp. Coronal T1 **(2A)** and STIR **(2B)** sequences through the entire pelvis and lower extremities were performed using a body matrix coil as an initial screen to identify areas of pathology. No abnormality was identified.

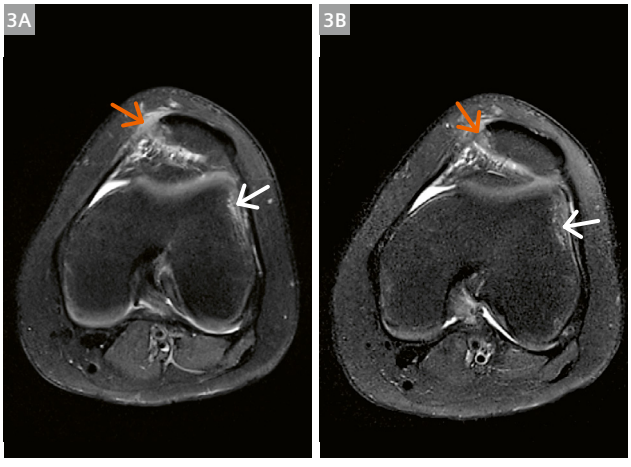

3 11-year-old female with patellar dislocation. **(3A)** Axial T2-weighted TSE image with fat suppression and **(3B)** corresponding axial T2-weighted SMS TSE image demonstrates a tear of the medial retinaculum (orange arrow) and a bone contusion at the lateral femoral condyle (white arrow).

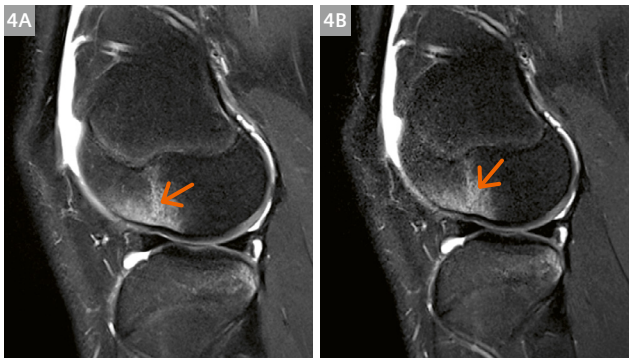

4 14-year-old boy with lateral femoral contusion (orange arrow) undergoing MRI. **(4A)** Sagittal T2-weighted TSE sequence and **(4B)** corresponding sagittal T2-weighted SMS TSE sequence for comparison.

The 3D TSE volumetric SPACE (Sampling Perfection with Application optimized Contrasts using different flip angle Evolution) acquisition is integral for imaging of large joints (knee and ankle) in children [13–18]. The three-dimensional, high-spatial resolution, isotropic images can be reconstructed into any imaging plane from a single volumetric data set, making it helpful for identifying subtle cartilage defects or ligamentous injuries. The imaging time, however, is relatively long which makes it particularly vulnerable to motion. The standard PD-weighted SPACE sequence in the knee protocol at our institution is 7 minutes and 40 seconds. Parallel imaging techniques can be applied to the acquisition but may cause aliasing artifacts and increase noise. CAIPIRINHA "Controlled Aliasing in Parallel Imaging Results in Higher Acceleration" [19] is a parallel imaging strategy that uses *k*-space sampling patterns designed to reduce aliasing and overlap on reconstructed images. While aliasing artifacts are still present, they are shifted to the corners of the image space.

Parameters	T2-weighted TSE	T2-weighted SMS TSE
Plane	Sagittal	Sagittal
Acquistion time (min:sec)	2:45	1:50
TR (ms)	4500	3000
TE (ms)	53	53
Echo train length	34	33
Matrix	384	384
Parallel imaging acceleration factor and reconstruction	2 (GRAPPA)	2 (GRAPPA)
FOV (mm)	140	140
Voxel dimension (mm)	0.4 x 0.4 x 3.0	0.4 x 0.4 x 3.0

Table 1: MRI parameters for T2-weighted TSE sequence versus T2-weighted SMS TSE sequence in the knee.

Parameters	PD-weighted 3D SPACE	PD-weighted 3D CAIPIRINHA SPACE
Plane	Sagittal	Sagittal
Acquistion time (min:sec)	7:40	4.00
TR (ms)	1000	1000
TE (ms)	49	49
Echo train length	41	41
Flip angle (°)	120	120 (variable)
Matrix	320 x 320 x 240	320 x 320 x 240t
Parallel imaging acceleration factor and reconstruction	2 (GRAPPA)	2 (GRAPPA)
FOV (mm)	162 x 249	162 x 249
Voxel dimension (mm)	0.54 x 0.54 x 1	0.54 x 0.54 x 1

Table 2: MRI parameters for Proton Density (PD)-weighted 3D SPACE sequence versus PD-weighted 3D CAIPIRINHA SPACE sequence in the knee.

Combined CAIPIRINHA and SPACE allows for 4-fold acceleration through undersampling in both the phase and partition encoding directions [14]. We compared the standard PD-weighted SPACE sequence in the knee with the CAIPIRINHA PD-weighed SPACE sequence (Table 2). Applying CAIPIRINHA to SPACE reduced our scan time from 7:40 minutes to 4:00 minutes without compromise in image quality (Figs. 5, 6). We reserve this sequence for slightly older patients (above the age of 8) who are able to cooperate for the 4 minute long acquisitions. In the younger patients, 2D sequences are still generally preferred. Anticipated pathologies in our youngest patients do not typically require such fine spatial resolution, and these patients reap greatest benefit from short acquisitions that require periodic opportunities for breaks.

Motion robust imaging alternatives are highly valuable in pediatric patients, particularly for abdominal and pelvic imaging [20]. Examinations that require breath-held sequences often require the child to be anesthetized and intubated to allow for periods of suspended respiration. With the aim of reducing need for anesthesia and/or the depth of anesthesia, free-breathing imaging capabilities are imperative. In the abdomen, 3D volumetric interpolated breath-hold examination (VIBE) imaging offers the most robust approach to acquiring T1-weighted imaging. VIBE allows for high spatial resolution with relatively fast imaging acquisitions of the entire abdomen [21, 22]. Depending on parameter selection, it is possible to acquire images through the entire field of view in approximately 20 seconds in a cooperative patient. Even adult patients may have difficulty breath-holding for a 20 second sequence [23], and children are even less likely to manage this. Cartesian VIBE obtained during free-breathing produces motion artifact within the image (Fig. 7) which limits the diagnostic quality of the sequence [24, 25]. T1-weighted images can be acquired with respiratory navigation, though this is less developed than navigated T2-weighted sequences, and image quality is inferior to the conventional breath-hold sequences [26–28]. Additionally, navigated T1-weighted imaging is not possible with fat suppression, which limits its utility for post-contrast imaging. A modified version of the VIBE sequence is a radial VIBE sequence that uses rectilinear sampling in the *z*-direction and radial sampling in the *xy* plane [24]. This sequence can be performed during free-breathing, and the radial sampling of *k*-space mitigates the effect of respiratory motion such that image quality is superior to the traditional breath-hold Cartesian VIBE [24]. The product version of this sequence is called StarVIBE, which is our standard for T1-weighted imaging in pediatric patients. Although the acquisition time is longer than a traditional VIBE sequence, the respiratory motion is distributed throughout the image such that there is little perception of the motion within the image. This technique is especially helpful for post-gadolinium enhanced imaging in the liver, kidneys, and bowel (Fig. 8). The ability to obtain high spatial-resolution, motionless imaging in patients who are freely breathing has dramatically altered our approach to sedating patients. We utilize the StarVIBE sequence in any child undergoing abdominopelvic imaging, for both pre and post-contrast fat-suppressed imaging.

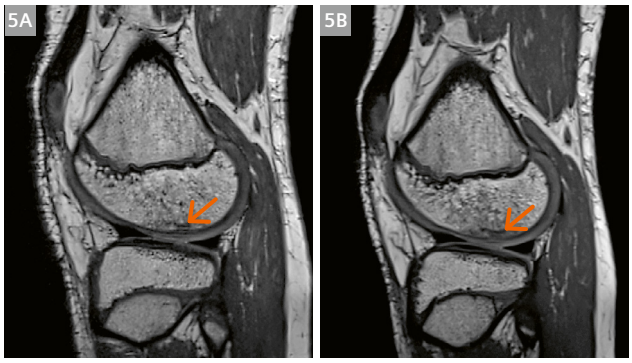

5 11-year-old female with lateral femoral condylar impaction fracture (orange arrow) seen on both **(5A)** sagittal PD-weighted SPACE sequence, and **(5B)** corresponding sagittal PD-weighted CAIPIRINHA SPACE sequence for comparison.

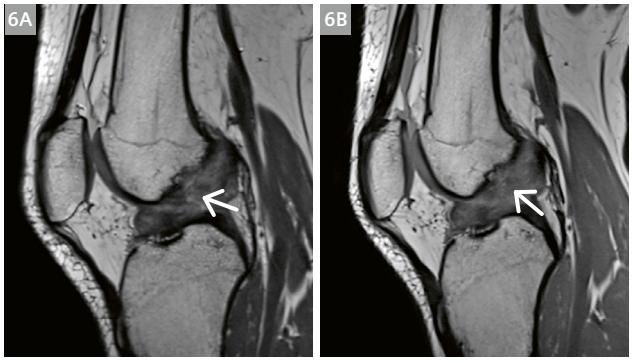

6 15-year-old female with ACL tear (white arrow). **(6A)** Sagittal PD-weighted SPACE sequence and **(6B)** corresponding sagittal PD-weighted CAIPIRINHA SPACE sequence through the ruptured ACL for comparison.

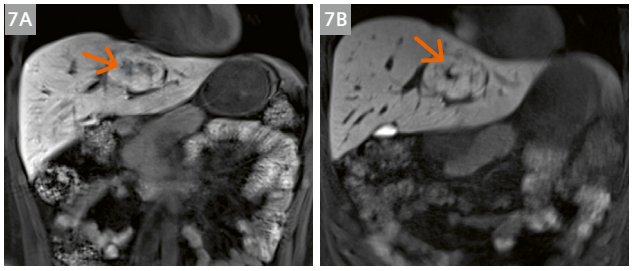

7 20-year-old female with FNH-like liver lesion. **(7A)** Coronal T1 VIBE with breath-holding after administration of Eovist contrast media reveals delayed uptake in a liver lesion (orange arrows), though images are degraded by motion. **(7B)** Sequence repeated with StarVIBE sequence with free-breathing demonstrates reduced motion artifact with better depiction of the lesion.

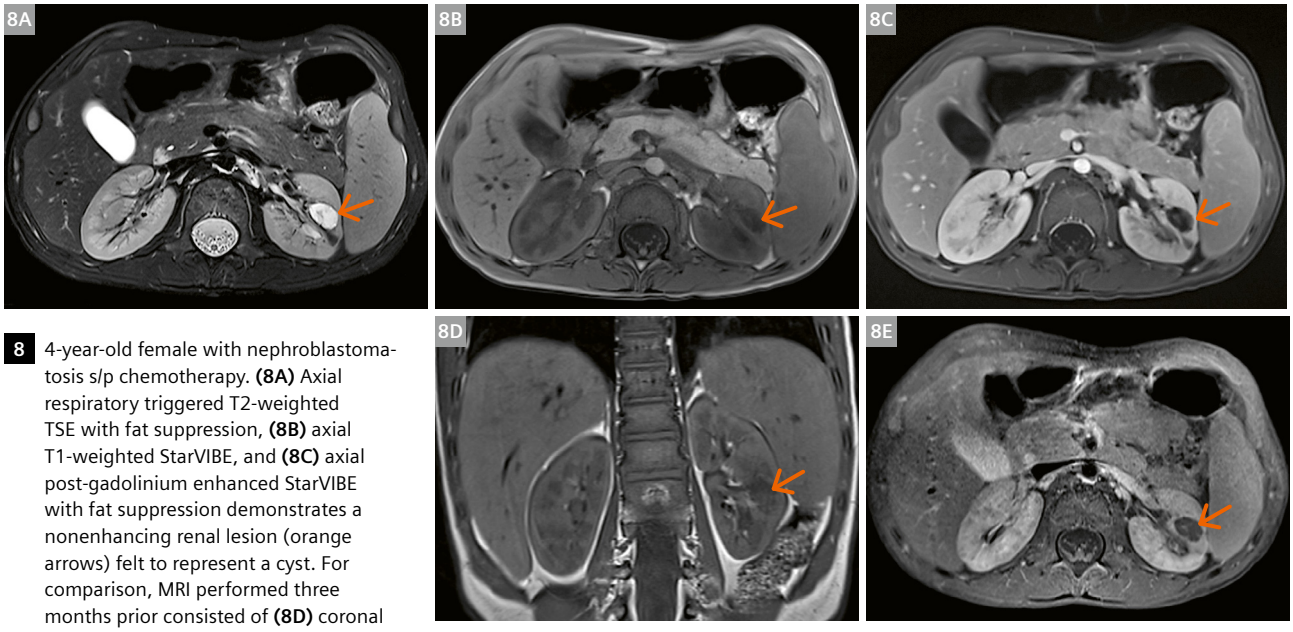

8 4-year-old female with nephroblastomatosis s/p chemotherapy. **(8A)** Axial respiratory triggered T2-weighted TSE with fat suppression, **(8B)** axial T1-weighted StarVIBE, and **(8C)** axial post-gadolinium enhanced StarVIBE with fat suppression demonstrates a nonenhancing renal lesion (orange arrows) felt to represent a cyst. For comparison, MRI performed three months prior consisted of **(8D)** coronal respiratory triggered T1-weighted TSE, **(8E)** axial post-gadolinium enhanced T1 TSE with fat suppression. Motion artifact is noted in the image from respiration.

The lack of breath-holding as a requirement for imaging obviates the requirement for endotracheal intubation, unless there are other reasons for which it would be required. A dynamic StarVIBE sequence is also available which allows for both high temporal resolution in addition to high spatial resolution images during dynamic contrast injection [29, 30], using compressed sensing techniques as a means to vastly undersample the data and reduce imaging times [20]. We are currently investigating this technique in the pediatric population, particularly with regard to renal, hepatic and bowel wall imaging.

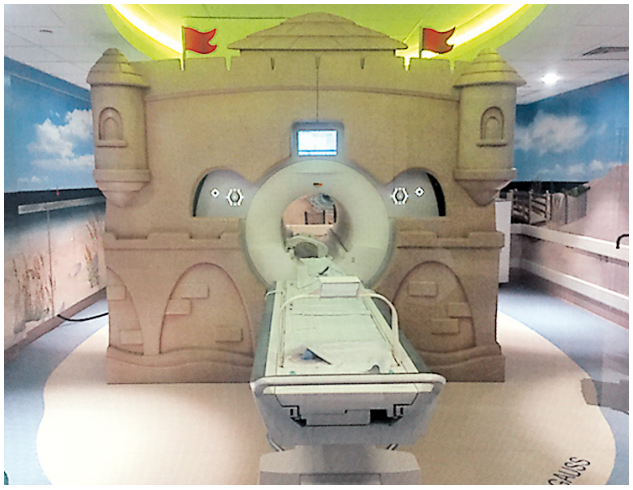

9 3T MAGNETOM Prisma MR scanner embedded in a sandcastle design. The room is decorated with decals in the theme of an ocean scene.

MR imaging in pediatric patients requires a team approach and collective efforts toward reducing our dependency upon sedation as a mechanism to acquire diagnostic, motion-free images. These include tailored protocoling, real-time monitoring, and utilization of accelerated or motion robust sequences. With the use of SMS TSE and CAIPIRINHA SPACE, MSK imaging examinations in children can be dramatically shortened without compromising image quality. StarVIBE imaging in the abdomen allows for high-resolution, free-breathing, T1-weighted imaging thereby eliminating requirement for endotracheal intubation for abdominal MRI in sedated patients. Reducing the anxiety and apprehension around the scanner and the scan room is also important in achieving patient cooperation. This can be achieved through embedding the scanner in a structure, such as a sandcastle, train, or boat (Fig. 9), decorating the room with colorful designs, distracting the patient with a movie during the scan, or preparing prior to the scan at a mock scanner or simulating the experience with virtual reality headsets. All of these strategies are currently employed at our hospital, oftentimes in combination. Further developments in prospective motion correction using motion cameras embedded in the magnet and sensors on the patient are currently being developed through collaborations with KinetiCor (Honolulu, HI, USA), with broad applications in the pediatric population. Our hope is that through these collective efforts we will drastically reduce the number of children requiring sedation for MRI, and improve the patient experience by reducing exam lengths and delays.

References

1 Callahan MJ, MacDougall RD, Bixby SD, Voss SD , Robertson RL, Cravero JP. Ionizing radiation from computed tomography versus anesthesia for magnetic resonance imaging in infants and children: patient safety considerations. Pediatr Radiol 2018; 48(1):21-30.
2 Paterson N, Waterhouse P. Risk in pediatric anesthesia. Paediatr Anaesth 2011; 21:848-857.
3 Robertson RL, Silk S, Ecklund K, Bixby SD, Voss SD, Robson CD. Imaging optimization in children. J Am Coll Radiol 2018; 15(3 Pt A):440-443.
4 Griswold MA, Jakob PM, Heidemann RM, Nittka M, Jellus V, Wang J, Kiefer B, Haase A. Generalized autocalibrating partially parallel acquisitions (GRAPPA). Magn Reson Medicine 2002 Jun; 47(6):1202-1210.
5 Breuer FA, Kannengiesser SA, Blaimer M, Seiberlich N, Jakob PM, Griswold MA. General formulation for quantitative G-factor calculation in GRAPPA reconstructions. Magn Reson Med 2009 Sep; 62(3):739-746.
6 Setsompop K, Gagoski BA, Polimeni JR, Witzel T, Wedeen VJ, Wald LL. Blipped-controlled aliasing in parallel imaging for simultaneous multislice echo planar imaging with reduced g-factor penalty. Magn Reson Med 2012 May 1; 67(5):1210-1224.
7 Barth M, Breuer F, Koopmans PJ, Norris DG, Poser BA. Simultaneous multislice (SMS) imaging techniques. Magn Reson Med 2016 Jan; 75(1):63-81.
8 Feinberg DA, Setsompop K. Ultra-fast MRI of the human brain with simultaneous multi-slice imaging. J Magn Reson 2013; 229:90-100.
9 Fritz J, Fritz B, Zhang J, Thawait GK, Joshi DH, Pan L, Wang D. Simultaneous multislice accelerated Turbo Spin Echo magnetic resonance imaging comparison and combination with in-plane parallel imaging acceleration for high-resolution magnetic resonance imaging of the knee. Invest Radiol 2017; 52:529-537.
10 Poser BA, Anderson RJ, Guerin B, Setsompop K, Deng W, Mareyam A, Serano P, Wald LL, Stenger VA. Simultaneous multislice excitation by parallel transmission. Magn Reson Med 2014; 71:1416-1427.
11 Gagoski BA, Bilgic B, Eichner C, Bhat H, Grant PE, Wald LL, Setsompop K. RARE/Turbo Spin Echo imaging with simultaneous multislice wave-CAIPI. Magn Reson Med 2015; 73:929–938.
12 Benali S, Johnston PR, Gholipour A, Dugan ME, Heberlein K, Bhat H, Bixby SD. Simultaneous multi-slice accelerated turbo spin echo of the knee in pediatric patients. Skeletal Radiol 2018 Jun; 47 (6):821-831.
13 Fritz J, Fritz B, Thawait GG, Meyer H, Gilson WD, Raithel E. Three-Dimensional CAIPIRINHA SPACE TSE for 5-Minute High-Resolution MRI of the Knee. Invest Radiol 2016; 51:609-617.
14 Fritz J, Ahlawat S, Fritz B, Thawait GK, Stern SE, Raithel E, Klyce W, Lee RJ. 10-min 3D Turbo Spin Echo MRI of the knee in children: arthroscopy-validated accuracy for the diagnosis of internal derangement. J Magn Reson Imaging 2018; doi: 10.1002/jmri.26241. epub ahead of print.

Contact

Sarah D. Bixby, M.D.
Associate Professor of Radiology
Department of Radiology
Boston Children's Hospital
300 Longwood Avenue,
Main Building, 2nd Floor
Boston, MA 02115
USA
Tel.: +1 857 218 4006
sarah.bixby@childrens.harvard.edu

15 Fritz J, Raithel E, Thawait GK, Gilson W, Papp DF. Six-fold acceleration of high-spatial resolution 3D SPACE MRI of the knee through incoherent k-space undersampling and iterative reconstruction – first experience. Invest Radiol 2016; 51:400–409.
16 Fritz J, Ahlawat S, Thawait GK, Raithel E, Gilson W, Lee RJ. 3D MRI of knee in pediatric patients with CAIPIRINHA SPACE: diagnostic performance assessment with arthroscopic correlation. Proc Intl Soc Mag Reson Med 2017; 25:1151.
17 Kalia V, Fritz B, Johnson R, Gilson WD, Raithel E, Fritz J. CAIPIRINHA accelerated SPACE enables 10-min isotropic 3D TSE MRI of the ankle for optimized visualization of curved and oblique ligaments and tendons. Eur Radiol 2017; 27:3652–3661.
18 Del Grande F, Delcogliano M, Guglielmi R, Raithel E, Stern SE, Papp DF, Candrian C, Fritz J. Fully automated 10-minute 3D CAIPIRINHA SPACE TSE MRI of the knee in adults. A multicenter, multireader, multifield-strength validation study. Invest Radiol 2018; 53:689-697.
19 Breuer FA, Blaimer M, Heidemann RM, Mueller MF, Griswold MA, Jakob PM. Controlled aliasing in parallel imaging results in higher acceleration (CAIPIRINHA) for multi-slice imaging. Magn Reson Med 2005 Mar 1; 53(3):684-691.
20 Jaimes C, Kirsch KE, Gee MS. Fast, free-breathing and motion-minimized techniques for pediatric body magnetic resonance imaging. Pediatr Radiol 2018; 48:1197-1208.
21 Rofsky NM, Lee VS, Laub G, Pollack MA, Krinsky GA, Thomasson D, Ambrosino MM, Weinreb JC. Abdominal MR imaging with a volumetric interpolated breath-hold examination. Radiology 1999; 212:876-884.
22 Lee VS, Lavelle MT, Krinsky GA, Rofsky NM. Volumetric MR imaging of the liver and applications. Magn Reson Imaging Clin N Am 2001; 9(4):697-716.
23 Krinsky GA, Lee VS, Theise ND, Weinreb JC, Rofsky NM, Diflo T, Teperman LW. Hepatocellular carcinoma and dysplastic nodules in patinets with cirrhosis: prospective diagnosis with MR imaging and explanation correlation. Radiology 2001; 219(2):445-54.
24 Chandarana H, Block TK, Rosenkrantz AB, Lim RP, Kim D, Mossa DJ, Babb JS, Kiefer B, Lee VS. Free-breathing radial 3D fat-suppressed T1-weighted gradient echo sequence. A viable alternative for contrast-enhanced liver imaging in patients unable to suspend respiration. Invest Radiol 2011; 46:648-653.
25 Chandarana H, Block KT, Winfeld MJ, Lala SV, Mazori D, Giuffrida E, Babb JS, Milla SS. Free-breathing contrast-enhanced T1-weighted gradient-echo imaging with radial k-space sampling for paediatric abdominopelvic MRI. Eur Radiol 2014; 24:320-326.
26 Vasanawala SS, Iwadate Y, Church DG, Herfkens RJ, Brau AC. Navigated abdominal T1-W MRI permits free-breathing image acquisition with less motion artifact. Pediatr Radiol 2010; 40:340-344.
27 Young PM, Brau AC, Iwadate Y, Vasanawala S, Daniel BL, Tamrazi A, Herfkens RJ. Respiratory navigated free breathing 3D spoiled gradient-recalled echo sequence for contrast-enhanced examination of the liver: diagnostic utility and comparison with free breathing and breath-hold conventional examinations. Am J Roentgenol AJR 2010; 195:687-691.
28 Azevedo RM, Campos ROP, Ramalho M, Heredia V, Dale BM, Semelka RC. Free-breathing 3D T1-weighted gradient echo sequence with radial data sampling in abdominal MRI: preliminary observations AJR Am J Roentgenol 2011; 197:650-657.
29 Kim KW, Lee JM, Jeon YS, Kang SE, Baek JH, Han JK, Choi BI, Bang Y-J, Kiefer B, Block KT, Ji H, Bauer S, Chin K. Free-breathing dynamic contrast-enhanced MRI of the abdomen and chest using a radial gradient echo sequence with K-space weighted image contrast (KWIC). Eur Radiol 2013; 23:1352–1360.
30 Kaltenbach B, Roman A, Polkowski C, Gruber-Rouh T, Bauer RW, Hammerstingl R, Vogl TJ, Zangos S. Free-breathing dynamic liver examination using a radial 3D T1-weighted gradient echo sequence with moderate undersampling for patients with limited breath-holding capacity. Eur J Radiol 2017; 86:26-32.

Performance of Compressed Sensing Cardiac Cine Imaging in Children: Initial Experience

Davide Curione[1]; Paolo Ciliberti[2]; Dolores Ferrara[3]; Teresa Pia Santangelo[1]; Paolo Ciancarella[1]; Carmela Napolitano[1]; Aurelio Secinaro[1]

[1]Advanced Cardiovascular Imaging Unit – Imaging Department, Bambino Gesù Children's Hospital IRCCS, Rome, Italy
[2]Pediatric Cardiology and Cardiac Surgery Department, Bambino Gesù Children's Hospital IRCCS, Rome, Italy
[3]Department of Advanced Biomedical Sciences, Federico II University, Naples, Italy

Abstract

The aim of our study was to compare conventional segmented balanced steady-state free precession (bSSFP) and real-time Compressed Sensing (CS) cardiac cine imaging in a small group of pediatric patients[1]. 20 subjects with either cardiomyopathy or congenital heart disease treated with biventricular repair were included. Examinations were carried out on our MAGNETOM Aera 1.5T (Siemens Healthcare, Erlangen, Germany) using both retrospectively cardiac-gated Cartesian conventional bSSFP and real-time CS cardiac cine sequences with whole coverage of the ventricles in the short-axis plane. Quantification of ventricular volumes was performed in all cases by two clinical cardiac MRI specialists in consensus. They were blinded to patient diagnosis and type of sequence, and correlated values with phase-contrast flow measurements. CS cardiac cine imaging showed good diagnostic quality and performance. It had slightly lower spatial and temporal resolution but there were no significant differences between ventricular volumes compared to conventional bSSFP sequences. We believe that real-time CS cardiac cine definitely has potential for the pediatric population. However, more work is needed to assess its performance and overcome its current limitations.

Parameters	bSSFP	CS
TR/TE (ms)	2.92/1.21	2.66/1.1
Temporal resolution (ms)	37.44	39.90
FOV (mm)	340	360
Rectangular FOV (%)	75	75
Matrix	256 x 192	208 x 156
Spatial resolution (mm)	1.5 x 1.5 x 7	1.7 x 1.7 x 7
Flip angle (°)	73	55
Bandwidth (Hz/pixel)	930	962
GRAPPA	x2	–
CS	–	x9.9
Cardiac gating	Retrospective	ECG-triggered
Trajectory	Cartesian	Cartesian
Reconstructed cardiac phases	25	20
Number of slices	~15 (12–18)	~15 (12–18)
Breath-hold time (s)	~10 (6.8–13.5) / 2 slices	~20 (17–25)
Total SAX acquisition time (s)	~160 (130–190)	~20 (17–25)
Total reconstruction time (s)	~immediate	~120 (100–150)

Table 1: Sequence parameters.
bSSFP = balanced steady-state free precession; CS = Compressed Sensing; FOV = field of view; GRAPPA = generalized autocalibrating partially parallel acquisition; SAX = short axis; TE = echo time; TR = repetition time

Introduction

Compressed Sensing (CS) is a relatively novel magnetic resonance imaging (MRI) technique based on *k*-space incoherent subsampling paired with a noise-reduction algorithm employing sparse representation in a nonlinear iterative reconstruction process. The aim is to drastically speed up acquisition without significantly degrading image quality [1]. In recent years, CS has become increasingly popular in cardiac MRI. This is especially true for cine imaging in adults, where CS has shown itself to be accurate and reproducible, allowing for fast and reliable scanning even in difficult patients [2, 3]. Compared to conventional segmented balanced steady-state free precession (bSSFP) cine sequences, the major advantages of real-time CS cardiac cine are the decreased scan duration and the relative insensitivity to motion such as irregular heart rhythms and breathing [4]. These features account for most of its appeal in pediatric cases, where patient cooperation is often limited. Moreover, in contrast with classic real-time cine imaging using parallel imaging, CS cardiac cine yields higher spatial and temporal resolution, closer to that of conventional segmented bSSFP [5]. Nevertheless, the smaller anatomical structures and higher heart rates typically found in children can still be a concern. Additionally, congenital heart disease (CHD) can significantly subvert the usual cardiac anatomy and multiple lesions can exist simultaneously. This leads to complex ventricular geometry and flow-volume calculations, and therefore requires a high degree of definition and accuracy. A disadvantage of CS is the relatively long reconstruction times [3], which could impact exam planning and limit clinical implementation. However, recent experiences investigating CS in children and CHD are encouraging, showing feasibility and good agreement with conventional cine imaging [6]. In this context, we present results from our initial experience of how real-time CS cardiac cine performs in comparison with conventional segmented bSSFP cine in a small group of pediatric patients.

Methods

Between January and March 2019, we studied 20 patients who had either cardiomyopathy or CHD treated with biventricular repair and who were referred for cardiac MRI. Informed written consent for additional research scans was obtained from all individuals/guardians. All procedures were in accordance with the ethical standards of the responsible committee on human experimentation and with the Declaration of Helsinki and its later amendments.

All imaging was performed on a 1.5-Tesla MRI scanner (MAGNETOM Aera, Siemens Healthcare, Erlangen, Germany). We used the Body 18 matrix coil and the spine coil incorporated into the scan table. A vector electrocardiographic system was used for cardiac-gating. Ventricular volume assessment was performed with both conventional bSSFP and real-time CS cardiac cine sequences in the ventricular short-axis (SAX) plane using sufficient contiguous slices for gapless imaging to ensure whole coverage of both ventricles. Conventional bSSFP cine imaging involved a multi-slice retrospectively cardiac-gated Cartesian sequence, with two slices acquired during every breath-hold. Spatial resolution was 1.5 x 1.5 x 7 mm and temporal resolution was ~37 ms. Real-time CS cardiac cine imaging employed a multi-slice cardiac-gated Cartesian sequence, with the whole volume obtained during a single breath-hold or during free-breathing if breath-holding was not feasible. The acquisition duration was two R-R intervals per slice; the first heartbeat was a non-imaging "dummy" used to reach the steady state, and the second heartbeat was used for data acquisition. Spatial resolution was 1.7 x 1.7 x 7 mm (8 mm in two cases) and temporal resolution was ~40 ms. Full sequence parameters are shown in Table 1.

Quantification of ventricular volumes was performed in all cases by two clinical cardiac MRI specialists in consensus (FD with 6 months and CD with 5 years of experience, respectively), blinded to patient diagnosis and type of sequence, in a random order, and using a commercially available software (cvi[42], Circle Cardiovascular Imaging Inc., Calgary, Canada). The end-diastolic and end-systolic phases were identified for each ventricle through simultaneous visual inspection of all SAX cine images. The endocardial borders of all slices at end-diastole and end-systole were traced manually and included papillary muscles and trabeculation in the blood pool volume. End-diastolic volume (EDV), end-systolic volume (ESV), stroke volume (SV = EDV − ESV), and ejection fraction (EF = SV/EDV × 100) were calculated, correlating SV with aortic and pulmonary valve phase-contrast flow measurements.

Normally distributed continuous data were reported as mean ± standard deviation. Categorical variables were reported as numbers and percentages. Student's independent t-test was used to compare continuous variables. A p-value of less than 0.05 indicated a significant difference.

[1]MR scanning has not been established as safe for imaging fetuses and infants less than two years of age. The responsible physician must evaluate the benefits of the MR examination compared to those of other imaging procedures. Note: This disclaimer does not represent the opinion of the authors.

Results

The mean patient age was 14.57 ± 4.92 years (range: 7–21). 10 patients (50%) were male. 11 had CHD, while the rest had suspected or known cardiomyopathy. The mean heart rate was 80.89 ± 14.48 bpm (range: 55–110 bpm). Demographic details and diagnoses are provided in Table 2.

Our preliminary results showed that there were no statistically significant differences ($p > 0.05$) in EDV, ESV, SV, or EF for left ventricular and right ventricular measurements using either bSSFP or CS sequences. Although not significant, for CS there was a small tendency toward underestimation of all volumes (which was more evident for the RV), and toward overestimation of EF. Ventricular measurements obtained with both sequences are summarized in Table 3. Notably, mean reconstruction time was quite long for CS, with an approximate mean time of 120 ± 15 seconds (range: 100–150) to complete the whole volume.

Characteristics	Mean ± SD (range)
Male/Female	10/10
Age (years)	14.57 ± 4.92 (7–21)
Height (cm)	147.76 ± 17.21 (110–178)
Weight (kg)	48.4 ± 17.09 (26–72)
BSA (m^2)	1.46 ± 0.33 (0.9–2)
Heart rate (bpm)	80.89 ± 14.48 (55–110)
Cardiomyopathy	8
Aortic coarctation	3
Aortic stenosis	2
Tetralogy of Fallot (repaired)	2
Transposition of the great arteries (repaired)	2
Aortopathy	1
Congenitally corrected transposition of the great arteries	1
Myopericarditis	1

Table 2: Patient demographics and diagnoses.
BSA = body surface area; SD = standard deviation

Discussion

In our study, real-time CS cardiac cine imaging showed good diagnostic quality and performance, with slightly lower spatial and temporal resolution (Figs. 1, 2) but no significant differences between calculated ventricular volumes compared to conventional segmented bSSFP sequences. In some cases where irregular heart rhythm or difficulties in breath-holding caused mild motion artifacts on bSSFP images, free-breathing CS cardiac cine provided visually more robust images for volume quantification (Fig. 3). From a clinical point of view, reproducible ventricular quantification is paramount, irrespective of differences in image quality, as significant biases may impact clinical decision making [6, 7]. However, poorer edge definition and myocardial blood pool contrast still posed a major challenge for accurate ventricular segmentation with CS. This aspect might also vary depending on the type of CS sequence employed, with spiral *k*-space trajectories showing better reported results compared to Cartesian acquisition [3, 6]. However, we believe that this difficulty was substantially mitigated by the use of phase-contrast imaging to obtain stroke volume reference values. Although not specifically evaluated, our impression was that the straightforward analysis of CS images without phase-contrast correlation might not yield the same results, as minor but frequent adjustments were required to achieve values that were in accordance with flow measurements. End-diastolic volumes would probably be slightly underestimated and end-systolic volumes would

Measurements	bSSFP	CS	p
LV EDV (mL)	135.8 ± 48.1	133.2 ± 50.2	0.87
LV ESV (mL)	53.5 ± 24.9	52.7 ± 27.6	0.91
LV SV (mL)	82.5 ± 25.5	80.7 ± 25.3	0.82
LV EF (%)	61.6 ± 7.0	61.9 ± 7.4	0.9
RV EDV (mL)	140.2 ± 39.9	134.6 ± 37.3	0.6
RV ESV (mL)	59.5 ± 21.6	55.9 ± 19.6	0.58
RV SV (mL)	80.9 ± 21.2	74.3 ± 24.2	0.36
RV EF (%)	58.5 ± 6.4	59.1 ± 6.7	0.79

Table 3: Ventricular measurements obtained with bSSFP and CS cine imaging.
bSSFP = balanced steady-state free precession; CS = Compressed Sensing; EDV = end-diastolic volume; EF = ejection fraction; ESV = end-systolic volume; LV = left ventricular; RV = right ventricular; SV = stroke volume
Ventricular measurements are expressed as mean ± standard deviation.

probably be slightly overestimated otherwise, due to blood pool being excluded from the contours in diastole and to myocardial mass being included in systole, particularly for the right ventricle [6]. The decision to employ phase-contrast correspondence was made because we normally use it in our everyday clinical practice and it is frequently described in children and CHD [8]. Nevertheless, it is clearly a major limitation of our study. A further drawback of CS was the long total reconstruction time [3]. In some cases, it reached several minutes, even though images of the first few slices were generally visible after about 20 seconds. Regardless, while not unacceptable, this could be a significant obstacle to adopting CS in everyday clinical practice. Another limitation of our study is the small and heterogeneous population considered. The group contained both cardiomyopathies and CHD, and there were

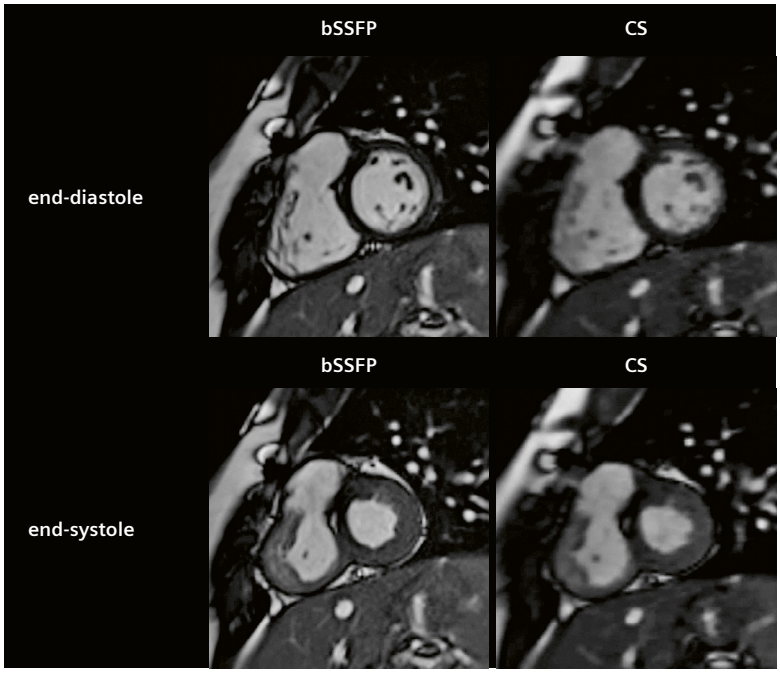

1 End-diastolic (top row) and end-systolic (bottom row) frames of conventional segmented balanced steady-state free precession (left column) and real-time Compressed Sensing cardiac cine sequences (right column) in a 13-year-old patient affected by tetralogy of Fallot treated with transannular patch and ventricular septal defect closure. The chemical shift artifact at the antero-basal interventricular septum corresponds to the area of ventricular septal defect repair.

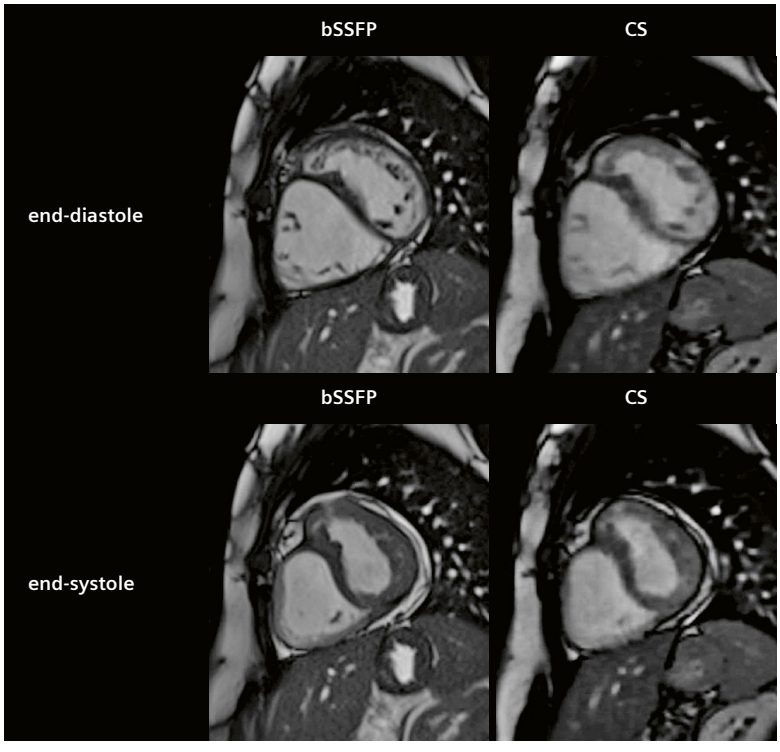

2 End-diastolic (top row) and end-systolic (bottom row) frames of conventional segmented balanced steady-state free precession (left column) and real-time Compressed Sensing (right column) cardiac cine sequences in a 15-year-old patient with congenitally corrected transposition of the great arteries. The anterior chamber is the subpulmonary left ventricle, which is dilated due to the presence of an ostium secundum interatrial defect. The posterior chamber is the hypertrophied systemic right ventricle.

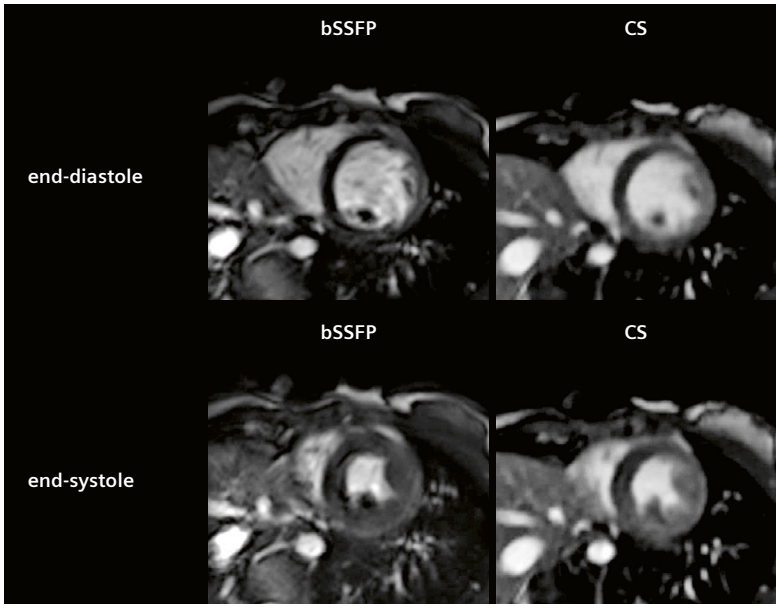

3 End-diastolic (top row) and end-systolic (bottom row) frames of conventional segmented balanced steady-state free precession (left column) and real-time Compressed Sensing (right column) cardiac cine sequences in a 9-year-old girl with sporadic ventricular ectopic beats and occasional difficulty performing breath-holds. Conventional bSSFP images show mild motion artifacts.

technical differences in two cases (slice thickness of 8 mm instead of 7 mm). Moreover, we did not calculate ventricular mass. Finally, the evaluation by two readers in consensus made it impossible to assess intra- and interobserver agreement. Future studies on larger and more homogeneous groups of patients could provide more robust results and evaluations of observer agreement.

In conclusion, we believe that CS definitely has potential for use in the pediatric population. However, more work is needed to assess its performance and to overcome its current limitations.

References

1 Lustig M, Donoho D, Pauly JM. Sparse MRI: the application of compressed sensing for rapid MR imaging. Magn Reson Med. 2007;58(6):1182–95.
2 Kido T, Kido T, Nakamura M, Watanabe K, Schmidt M, Forman C, et al. Compressed sensing real-time cine cardiovascular magnetic resonance: accurate assessment of left ventricular function in a single-breath-hold. J Cardiovasc Magn Reson. 2016;18(1):50.
3 Haji-Valizadeh H, Rahsepar AA, Collins JD, Bassett E, Isakova T, Block T, et al. Validation of highly accelerated real-time cardiac cine MRI with radial k-space sampling and compressed sensing in patients at 1.5T and 3T. Magn Reson Med. 2018;79(5):2745–51.
4 Goebel J, Nensa F, Schemuth HP, Maderwald S, Quick HH, Schlosser T, Nassenstein K. Real-time SPARSE-SENSE cine MR imaging in atrial fibrillation: a feasibility study. Acta Radiol. 2017;58(8):922–8.
5 Voit D, Zhang S, Unterberg-Buchwald C, Sohns JM, Lotz J, Frahm J. Real-time cardiovascular magnetic resonance at 1.5 T using balanced SSFP and 40 ms resolution. J Cardiovasc Magn Reson. 2013;15:79.
6 Steeden JA, Kowalik GT, Tann O, Hughes M, Mortensen KH, Muthurangu V. Real-time assessment of right and left ventricular volumes and function in children using high spatiotemporal resolution spiral bSSFP with compressed sensing. J Cardiovasc Magn Reson. 2018;20(1):79.
7 Oosterhof T, van Straten A, Vliegen HW, Meijboom FJ, van Dijk APJ, Spijkerboer AM, et al. Preoperative thresholds for pulmonary valve replacement in patients with corrected tetralogy of Fallot using cardiovascular magnetic resonance. Circulation. 2007;116(5):545–51.
8 Fratz S, Chung T, Greil GF, Samyn MM, Taylor AM, Valsangiacomo Buechel ER, et al. Guidelines and protocols for cardiovascular magnetic resonance in children and adults with congenital heart disease: SCMR expert consensus group on congenital heart disease. J Cardiovasc Magn Reson. 2013;15:51.

Contact

Aurelio Secinaro, M.D.
Bambino Gesù Children's Hospital IRCCS
Department of Imaging
Piazza Sant'Onofrio 4
00146 Rome
Italy
Phone: +39 06 68592790
Fax: +39 06 68594561
aurelio.secinaro@opbg.net


Aurelio Secinaro


Davide Curione

Robust, Efficient, and Comprehensive Pediatric Imaging with BioMatrix Technology and High-End Applications

Johan Dehem, M.D.

VZW Jan Yperman, Ypres, Belgium

In the world of social media, the relationship between pediatrics[1] and MRI would be: "It's complicated." On the one hand, MRI is a completely radiation-free technique, which makes it an excellent *primum non nocere* tool. MRI is also a tool that, more than transfontanellar ultrasound or CT, excels in providing comprehensive diagnostic information. On the other hand, MRI can suffer from some "childish behavior". Keeping a toddler busy with toys in the waiting room is one thing, but having the same toddler immobilized completely for some time can be challenging with CT, let alone with MRI.

Many pediatric procedures therefore happen with a little help from our friends in the anesthesia department. Scheduling tasks and logistics becomes more complex, since you need anesthesia on site, but having the young patient securely ventilated and monitored throughout the exam is reassuring and only right. Parents trust their children to us, and we must live up to that duty and responsibility. For very young children[1] with a smaller head size, we use the dedicated pediatric head coil, which results in a high signal-to-noise ratio, even in these small children. It comes with a cradle into which patient is put immediately after anesthesia. The colleagues just love to transport the little one to the magnet in the cradle, which is then slid into the head coil.

It is a great relief to have the baby safe in the cradle instead of limp (anesthetized) in your arms. This picture shows our very first patient in the cradle. My colleague Leen did the anesthesia and she was delighted with the ease of use of this slide-cradle. A keen observer might see

1 **(1A)** The cradle allows safe, swift and easy transportation from the preparation room to the MRI room. **(1B)** Anesthetized, ventilated child (larynx mask) in the cradle, waiting in the preparation room of the MRI suite for transport to the MRI room. Notice the yellow earplug in the left ear.

[1] *MR scanning has not been established as safe for imaging fetuses and infants less than two years of age. The responsible physician must evaluate the benefits of the MR examination compared to those of other imaging procedures. Note: This disclaimer does not represent the opinion of the authors.*

the (fluorescent) earplug in the left ear. In keeping with the principle of *primum non nocere*, we do everything we can to protect our patients' hearing – including running quiet sequences. It is no coincidence that the dedicated pediatric coil is a head coil, since most indications in pediatric MRI are brain exams. However, the cradle is also ideal for combining with the Ultra Flex coil (small or large), which can be wrapped around the baby in the cradle to examine the abdomen, for instance.

Let's now have a look at some cases: In this four-year-old boy investigated for encopresis and enuresis, an altered Babinski was noted on clinical exam. A brain MRI was ordered to exclude brain lesion, and a spine MRI was ordered to exclude tethered cord and Chiari malformation. Brain (Fig. 2) and spine (Fig. 3) exams were acquired in one session. The patient was safely in the cradle, and the dedicated head coil was combined with the BioMatrix 32-channel spine coil embedded in the patient table.

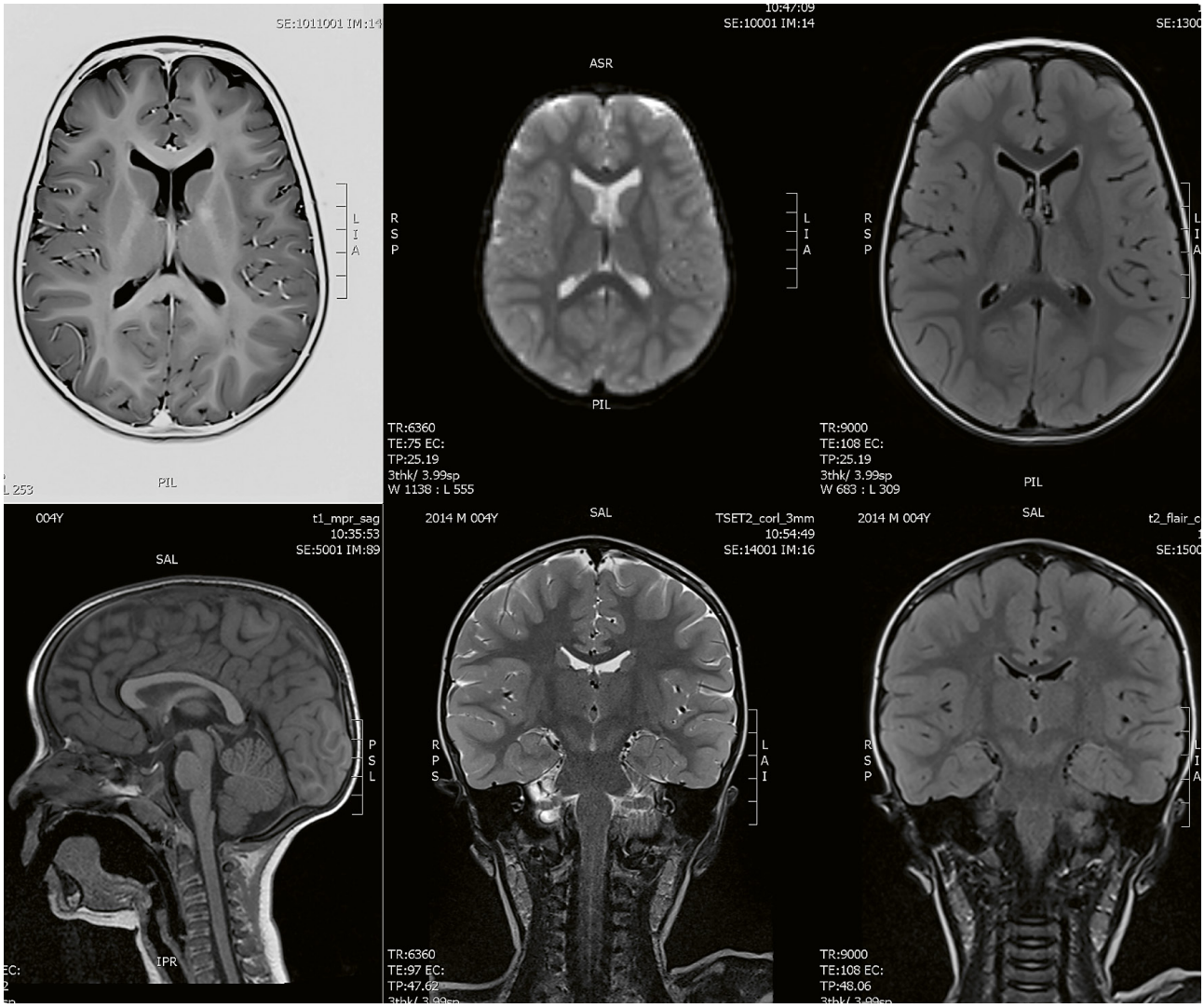

2 3 mm slice thickness T1 inversion recovery, quiet diffusion b_0 image and axial FLAIR (top row), 3D MPRAGE sagittal, and 3 mm coronal T2 and T2 FLAIR (bottom row); high signal from the dedicated pediatric coil that even fits this four-year-old.

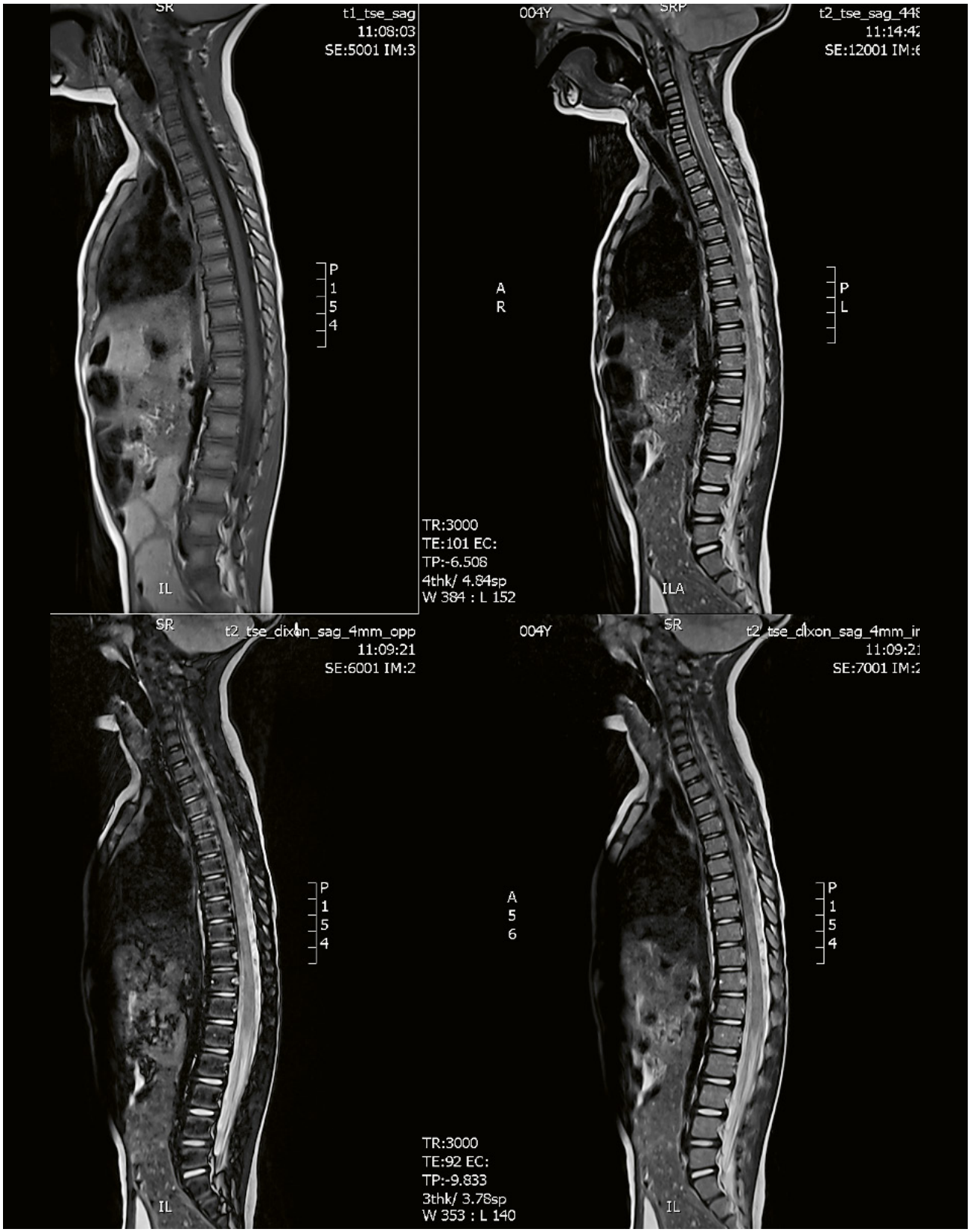

3 Same patient as in Figure 2, examined in the same session using the 32-channel spine coil in the 1.5T MAGNETOM Sola; 3 mm slice thickness (sagittal T1 and T2 TSE, FOV 30 cm; top row) and T2 TSE Dixon technique, FOV 30 cm, 3 mm slice thickness in phase and opposed phase (bottom row) effectively ruling out cord anomalies.

This one-week-old baby[1] has a sacral dimple and rather large skin tag. This raises the suspicion of closed spinal dysraphism, which is confirmed on MRI (Figs. 4–6) with associated myelolipoma and cord tethering. Since motor innervation of lower limbs is clinically normal, the neurosurgeon decided to postpone intervention. Intervention will become necessary when the cord tethering causes motor dysfunction, later on during growth of the spinal canal. Meanwhile, the baby is under close surveillance by the pediatrician. No associated brain lesions (Fig. 7) were demonstrated, and there was no Chiari II malformation.

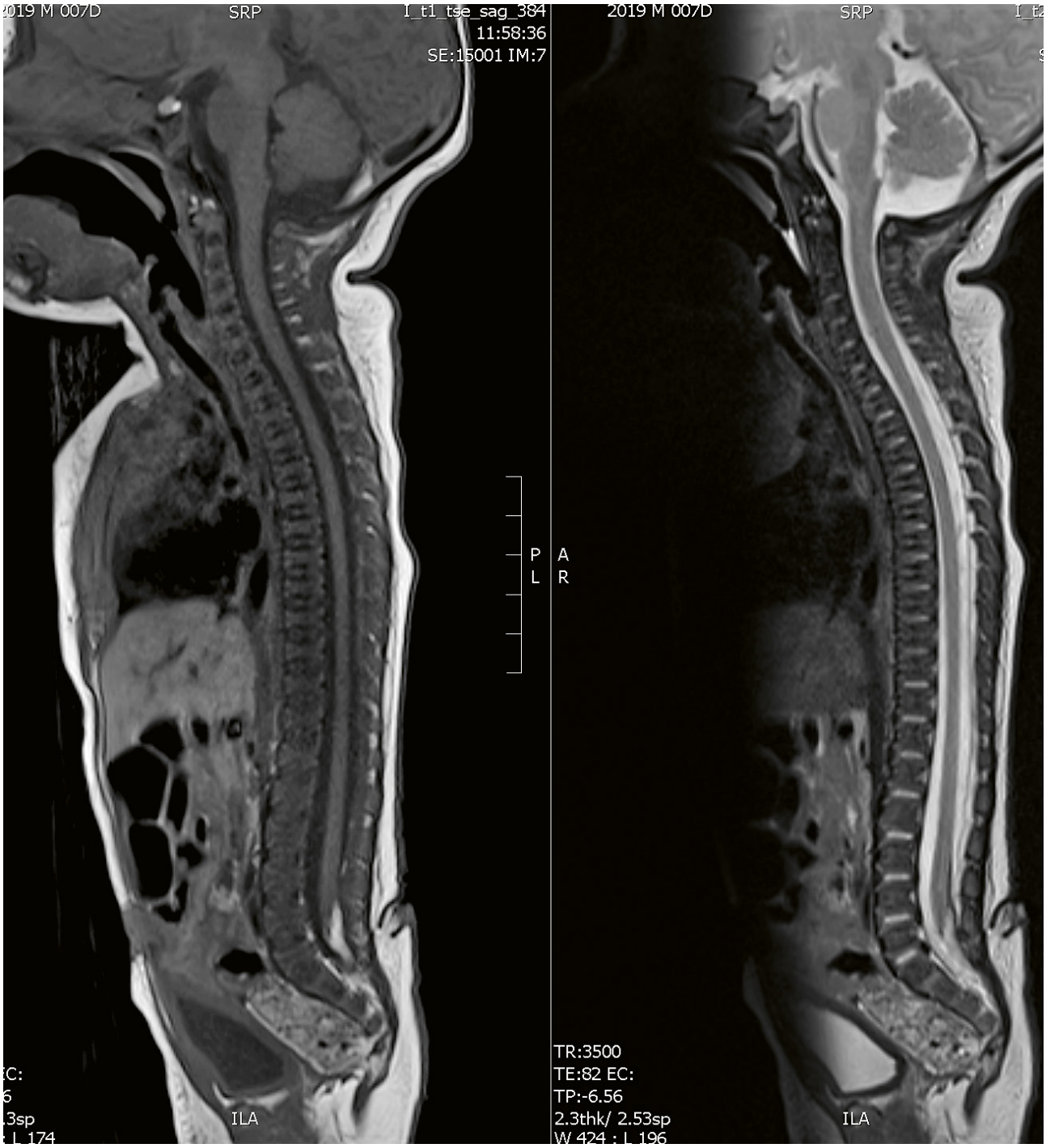

4 Sagittal T1 and T2 TSE 2.3 mm whole-spine images demonstrating the dimple, skin tag, and tethered cord with associated myelolipoma.

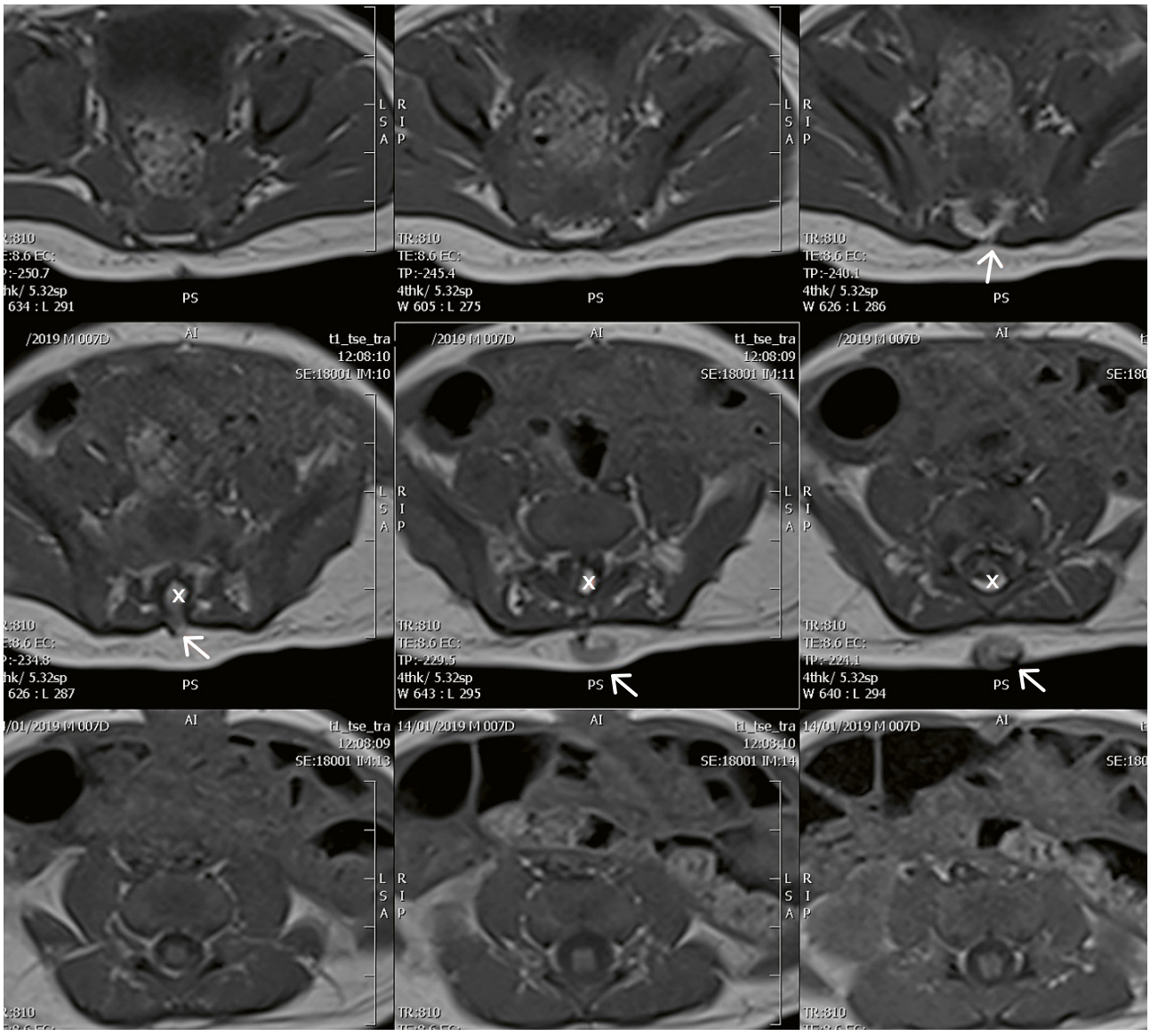

5 Axial T1 demonstrating dysraphism, dimple, and skin tag (arrow); white cross indicates myelolipoma.

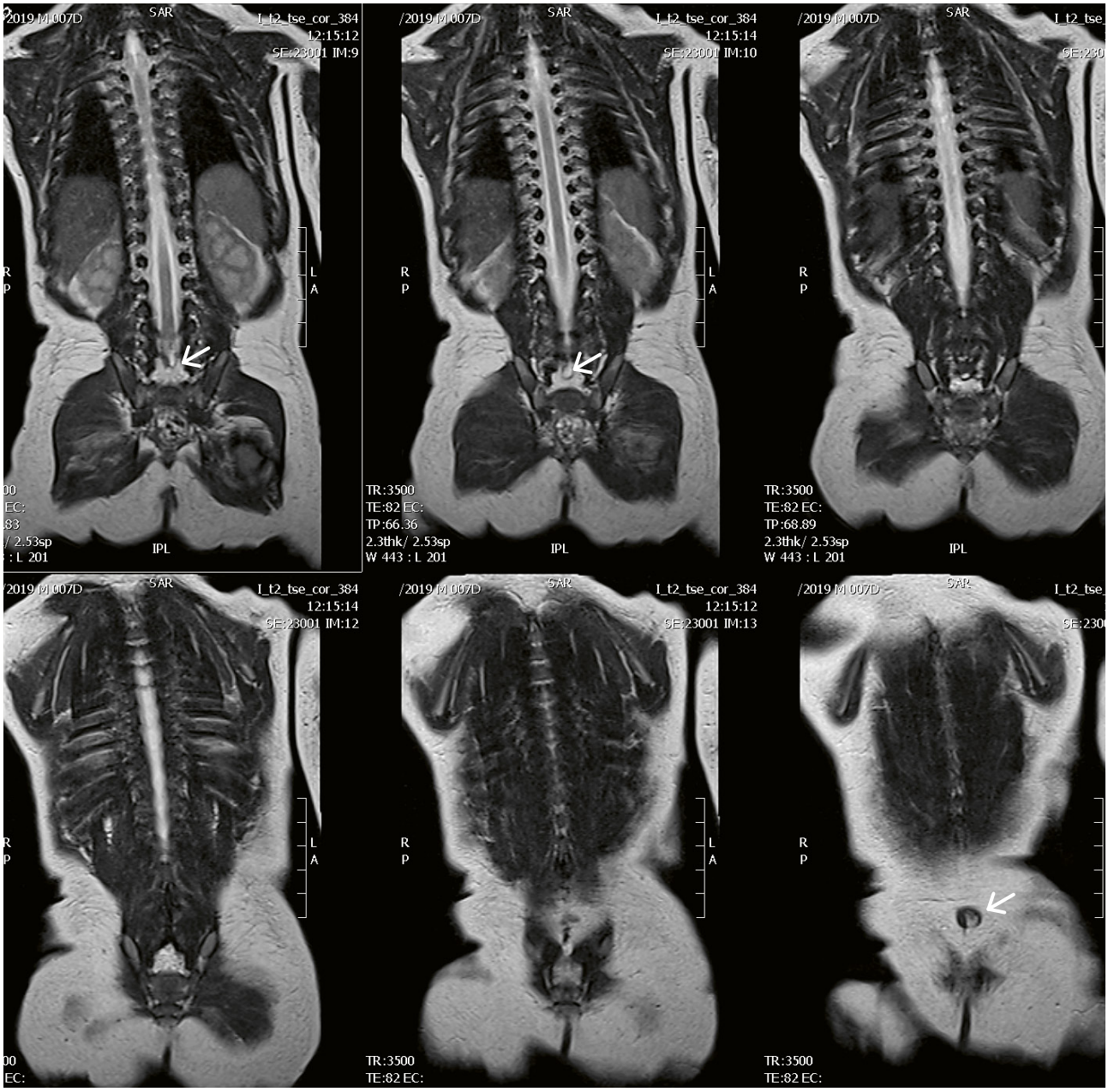

6 Coronal T2 TSE demonstrating dimple and skin tag (arrow), and myelolipoma (arrow).

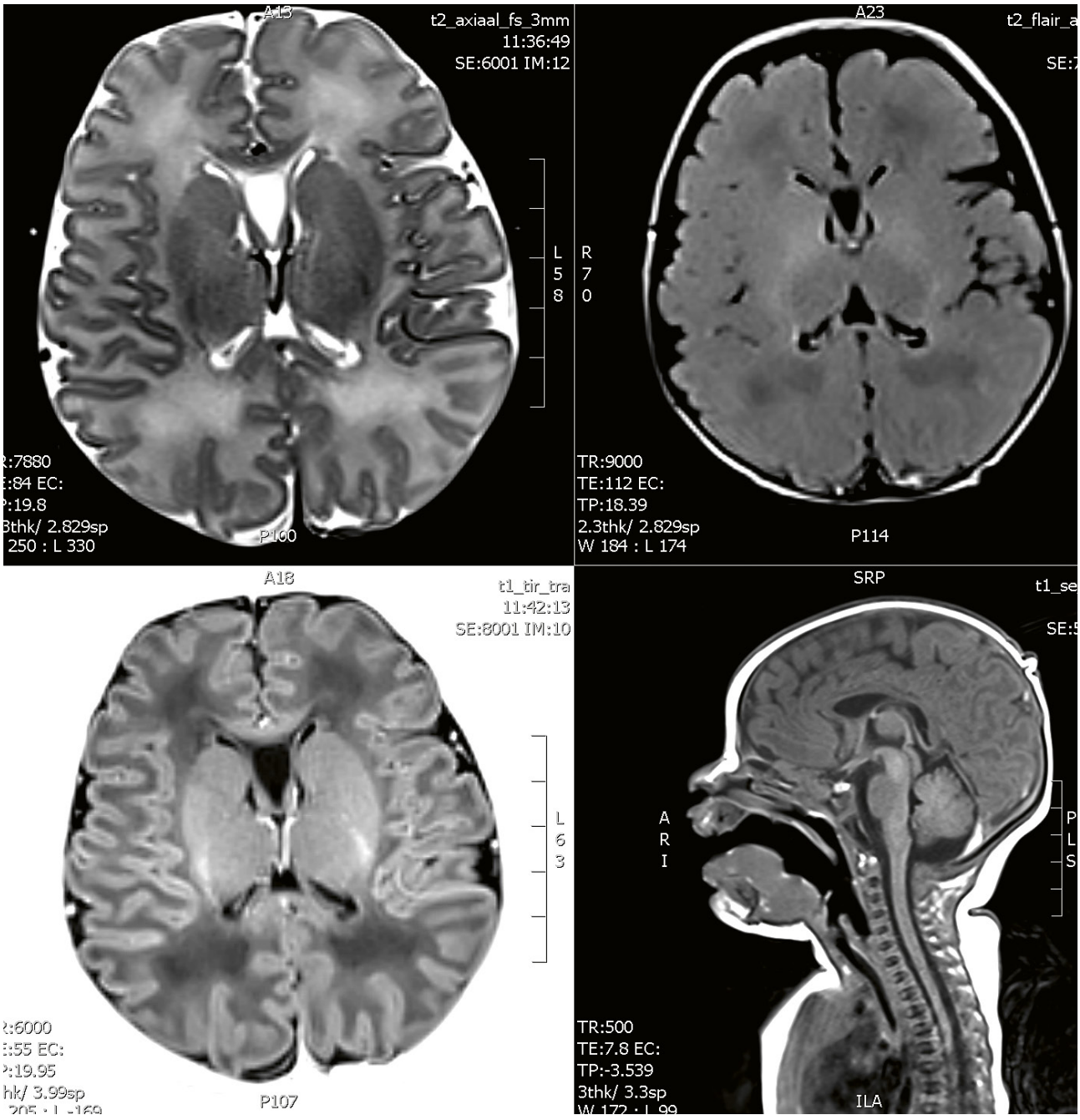

7 T2 axial fatsat and axial FLAIR with 3 mm slice thickness (top row); T1 inversion recovery axial 3 mm, T1 TSE sagittal 3 mm (bottom row); no associated brain lesions, no Chiari malformation.

Delayed neurological development in this 13-month-old baby[1] with genodermatosis (duplication proximal chromosome 6 (+/- 20 MB) (6q13q15 regio)) prompted a request for a brain MRI to exclude brain anomalies.

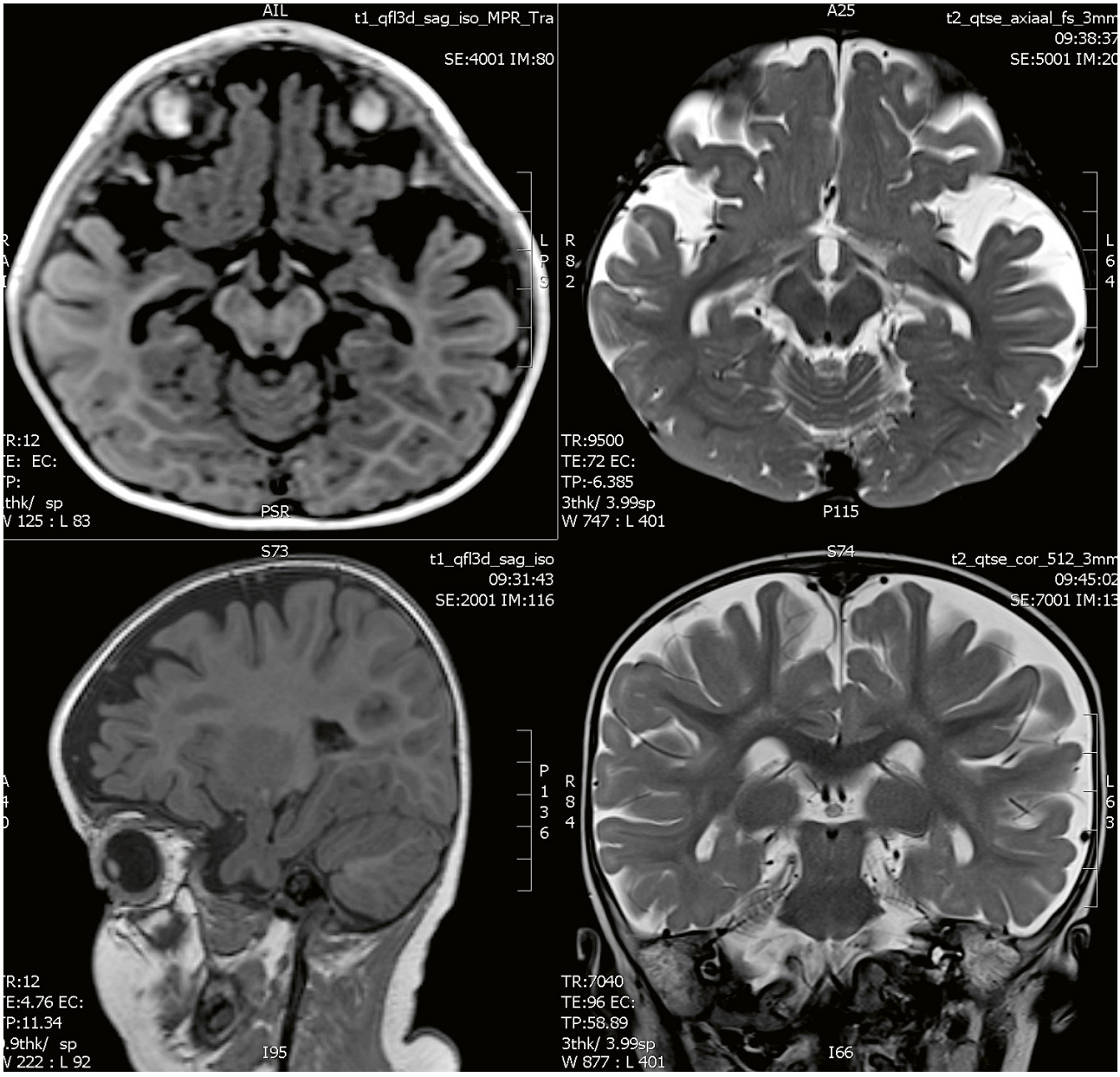

8 Quiet T2 TSE coronal and axial (right column) acquisition and quiet T1 FLASH 3D (left column) with sagittal acquisition and coronal reconstruction; besides benign enlargement of the subarachnoid spaces in infancy, a clear brachycephalic appearance is notable; age-correlated normal myelination; notice the high signal in 2D TSE images with 3 mm slice thickness and in the 0.9 isotropic T1 images in the dedicated pediatric head coil.

This four-year-old toddler experienced a witnessed seizure. Since clinical examination, EEG, and MRI were normal, no medication was started.

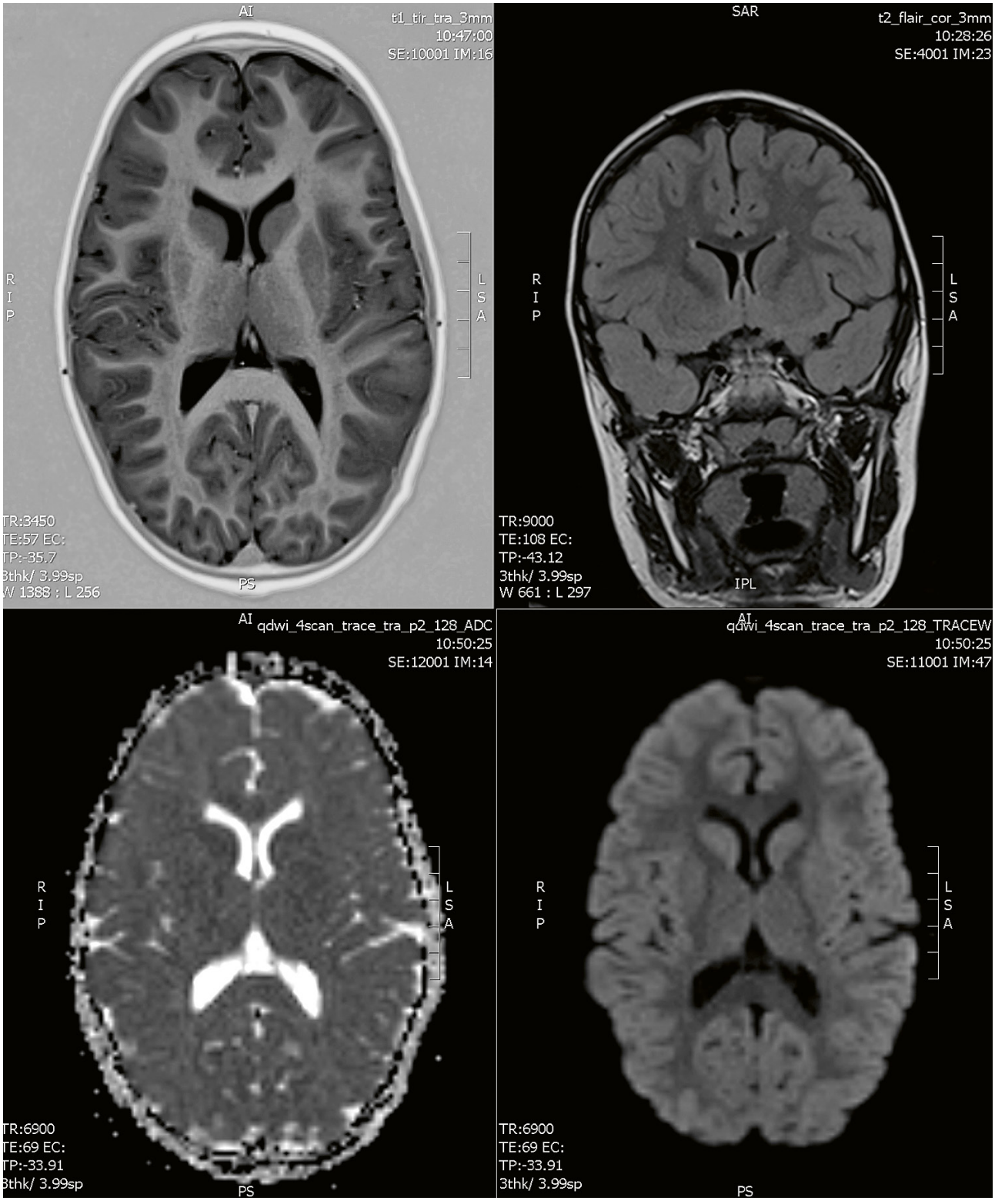

9 3 mm slices, axial T1 inversion recovery and coronal T2 FLAIR (top row), and axial quiet diffusion and ADC map (bottom row).

Repeated feverish convulsions were seen in this three-year-old. EEG was normal, but the last episode was atypical with lateralization.

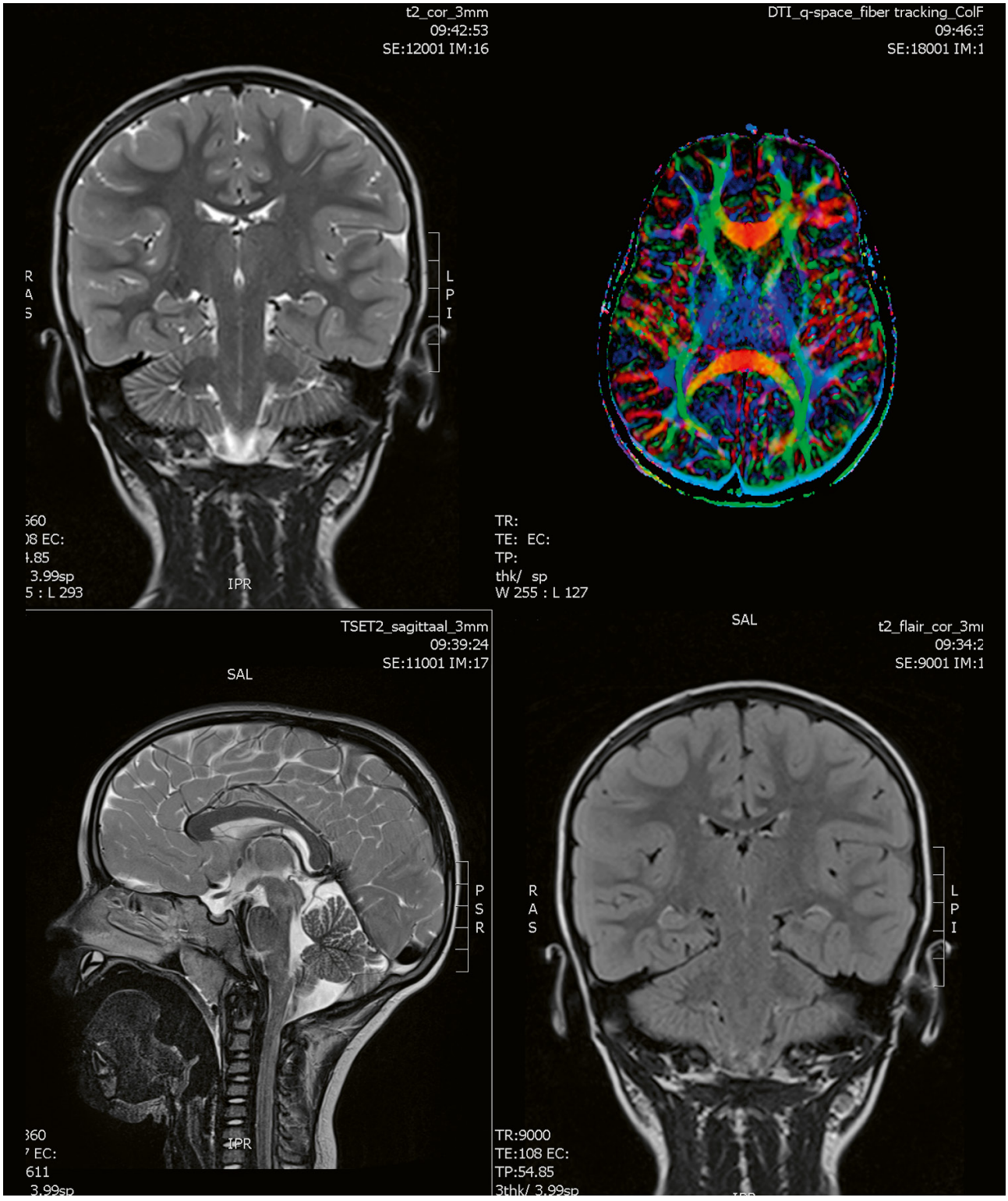

10 Coronal 3 mm quiet T2 TSE, and DTI q-space fiber tracking (top row); 3 mm quiet T2 sagittal and 3 mm coronal FLAIR (bottom row); no underlying anomaly.

This four-year-old suffered from excessive headaches and vomiting.

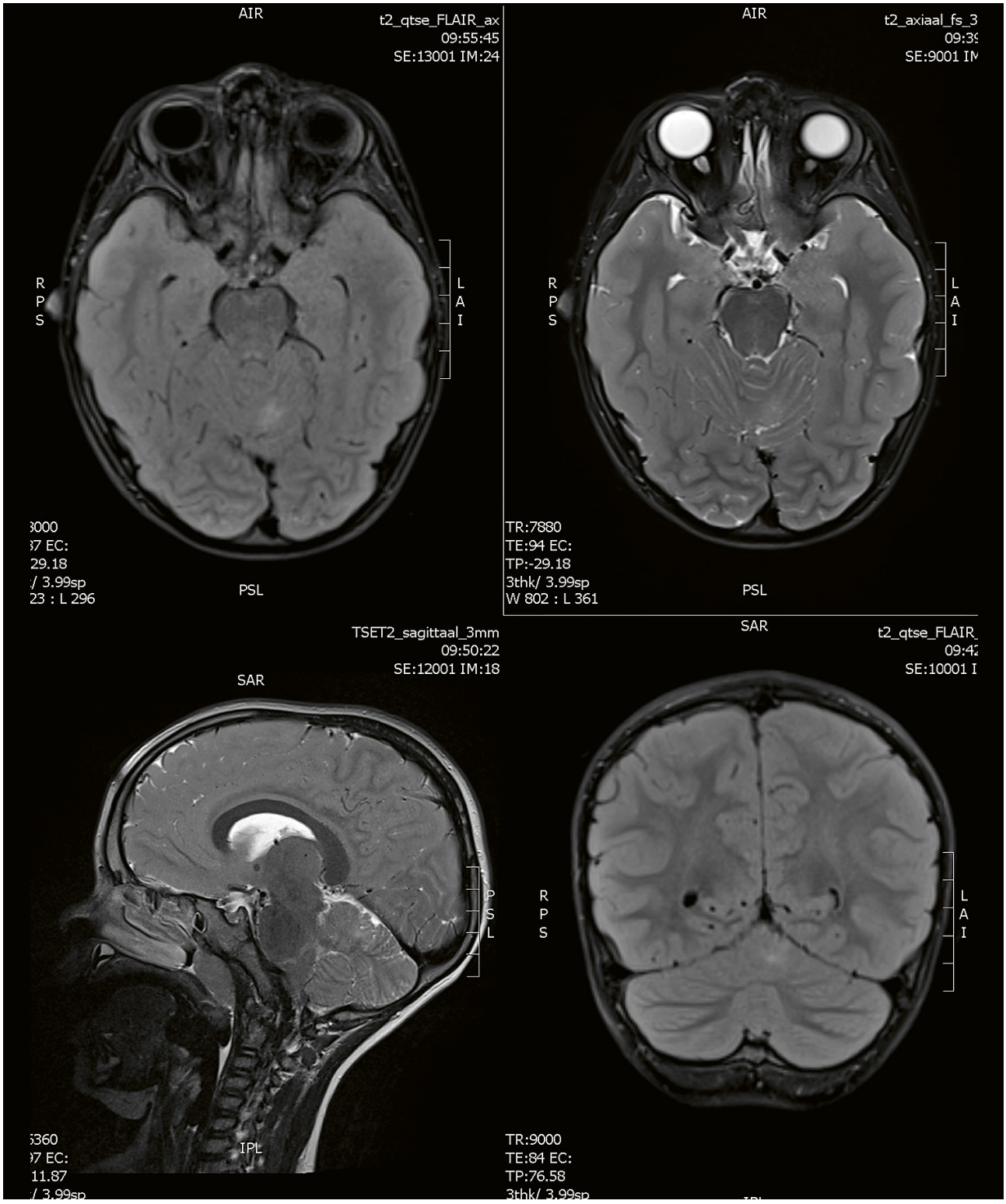

11 3 mm axial FLAIR and T2 TSE quiet sequence, 3 mm (top row) and sagittal T2 TSE and coronal FLAIR 3 mm quiet sequence (bottom row) demonstrate small T2 and FLAIR hyperintense cerebellar mass-like cortical and subcortical deformation in the vermis, suggestive of focal microgyria.

This three-year-old, ex-premature (32 weeks, chorioamnionitis) patient had Grade I bilateral germinal matrix bleeding (GMH) and delayed development.

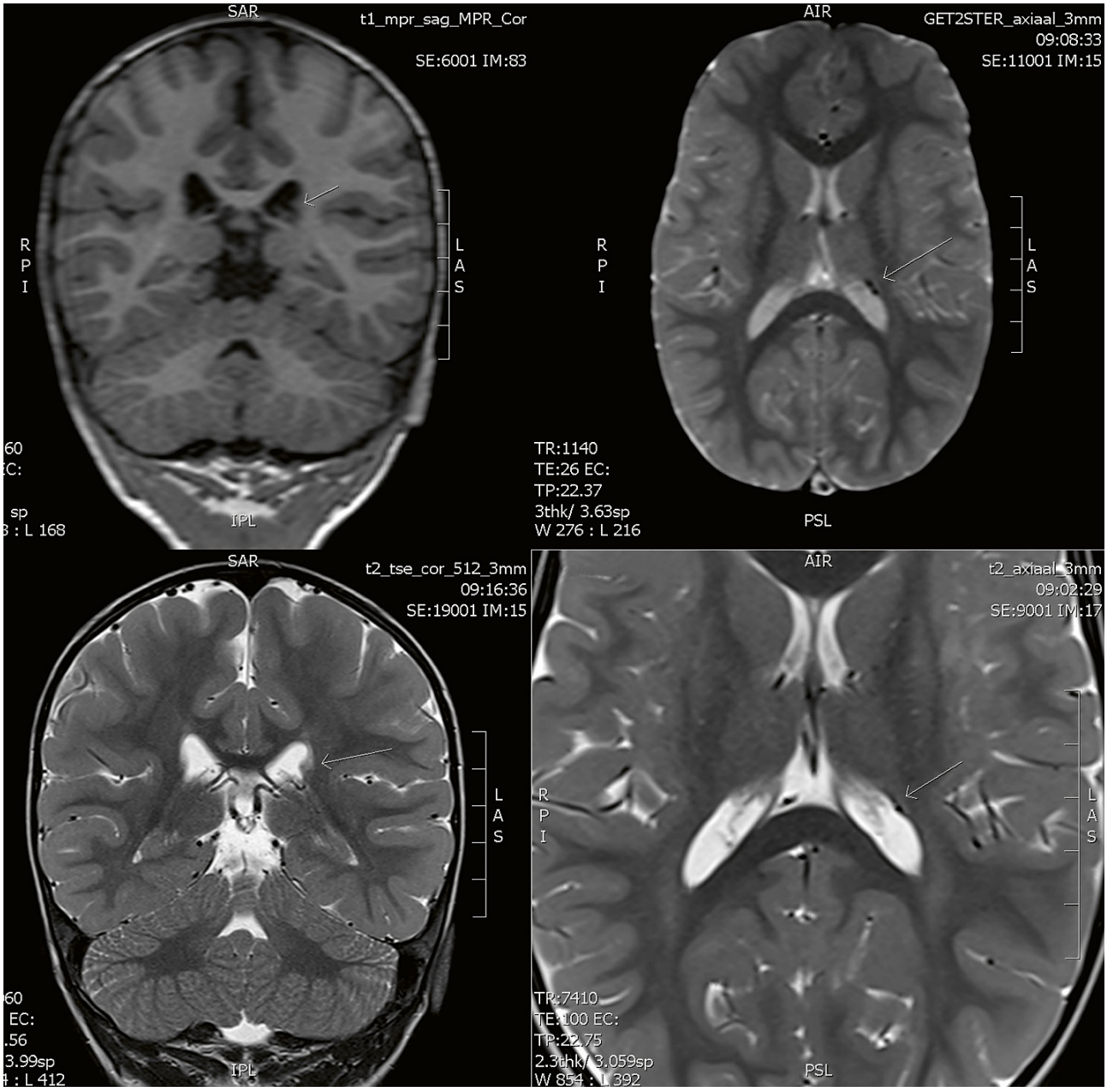

12 3D MPRAGE coronal reformat, 3 mm axial T2*(top row) and coronal T2 TSE quiet sequence, 3 mm (bottom row), and zoomed-in 3 mm axial T2 TSE sequences (bottom row) demonstrate small T2 and more obvious T2* hypointense spots that reflect the known Grade 1 GMH.

This 19-month-old baby[1] with cryptorchidism underwent orchiopexy on the left side and laparoscopic procedure/search for suspected (previous ultrasound) intra-abdominal right testis below the kidney. Laparoscopy failed to prove suspected intra-abdominal testis. MRI was ordered to search for intra-abdominal testis.

Since the breath-holding technique is not an option for this patient, we used the StarVIBE sequence, running pre- and post-contrast images covering kidneys to groin. Inplane resolution was 1 mm and slice thickness was 1.1 mm. Acquisition time was 3 minutes and 45 seconds, and it was a free-breathing acquisition.

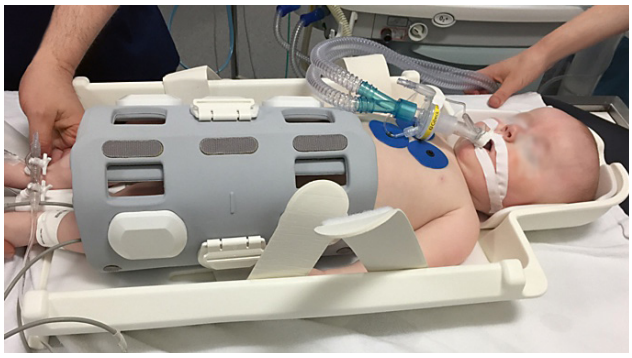

13 As a technical note: In the cradle one can easily wrap and fix the ultraflex coil for abdominal or pelvic examinations.

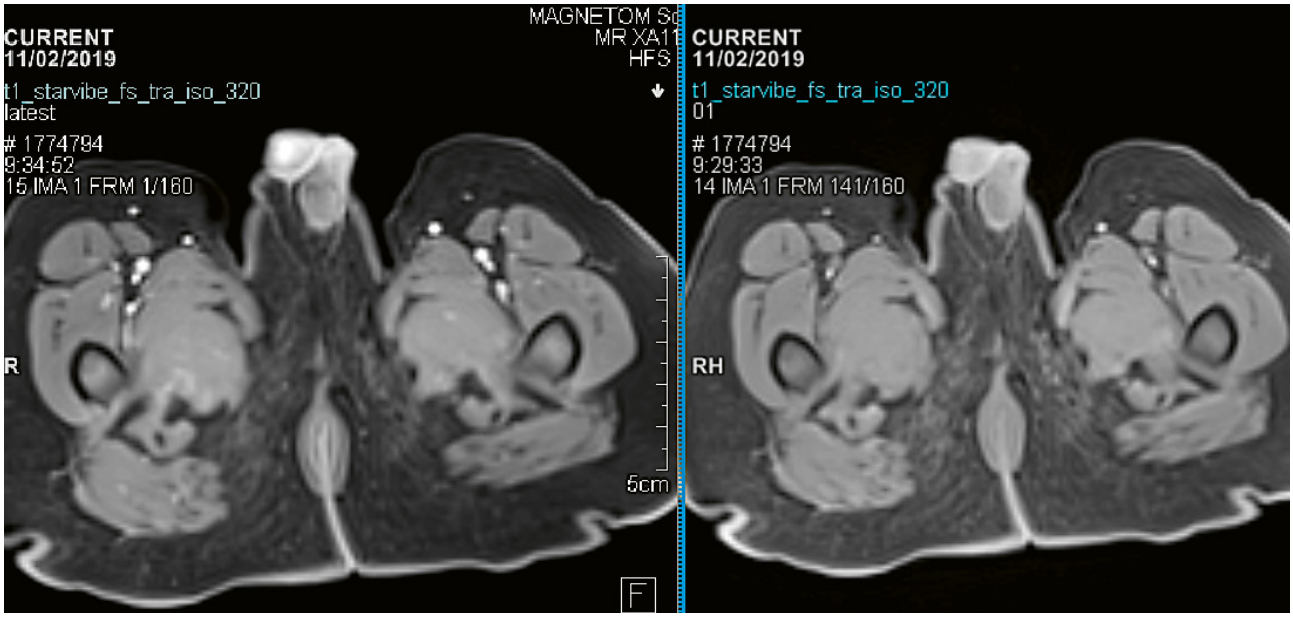

14 Axial StarVIBE with and without contrast, 1.2 mm slices; left testis *in situ* after orchiopexy.

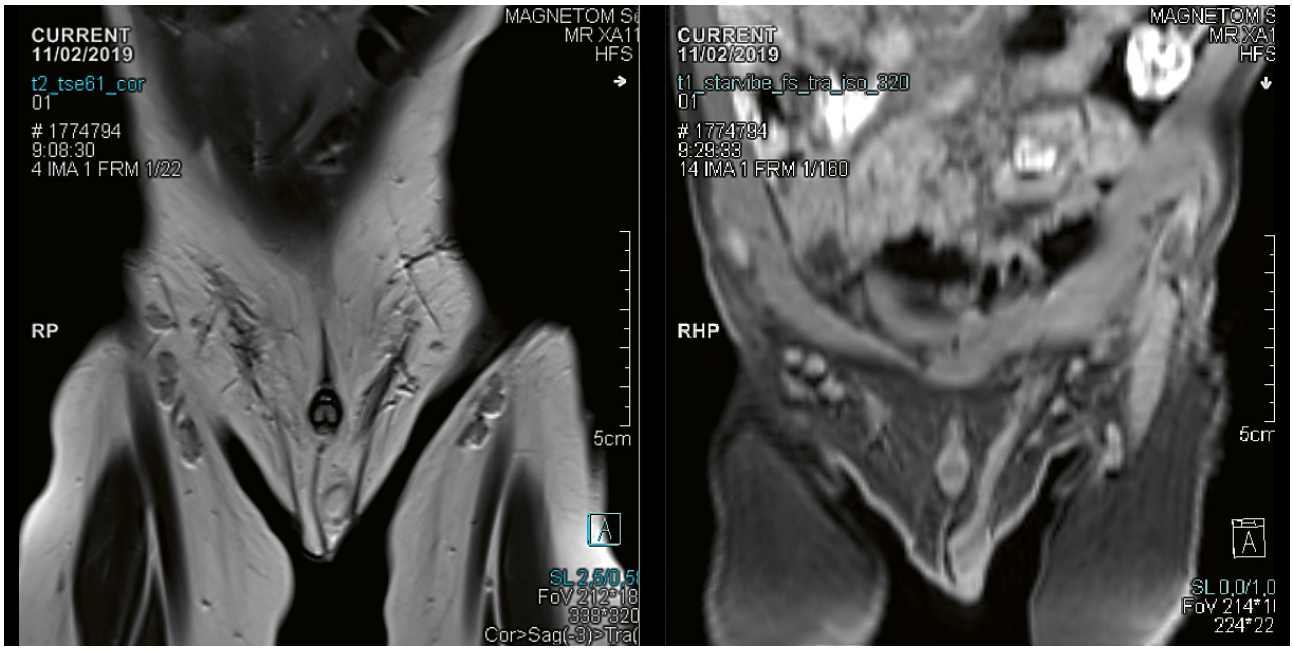

15 Coronal T2 TSE, inplane resolution 0.6 mm, slice thickness 2.5 mm, and coronal reconstructed T1 StarVIBE acquisition demonstrate scarring and fibrosis from laparoscopic access ports, and presence of testis and spermatic cord on the left side, with an empty scrotal sac and inguinal canal on the right side.

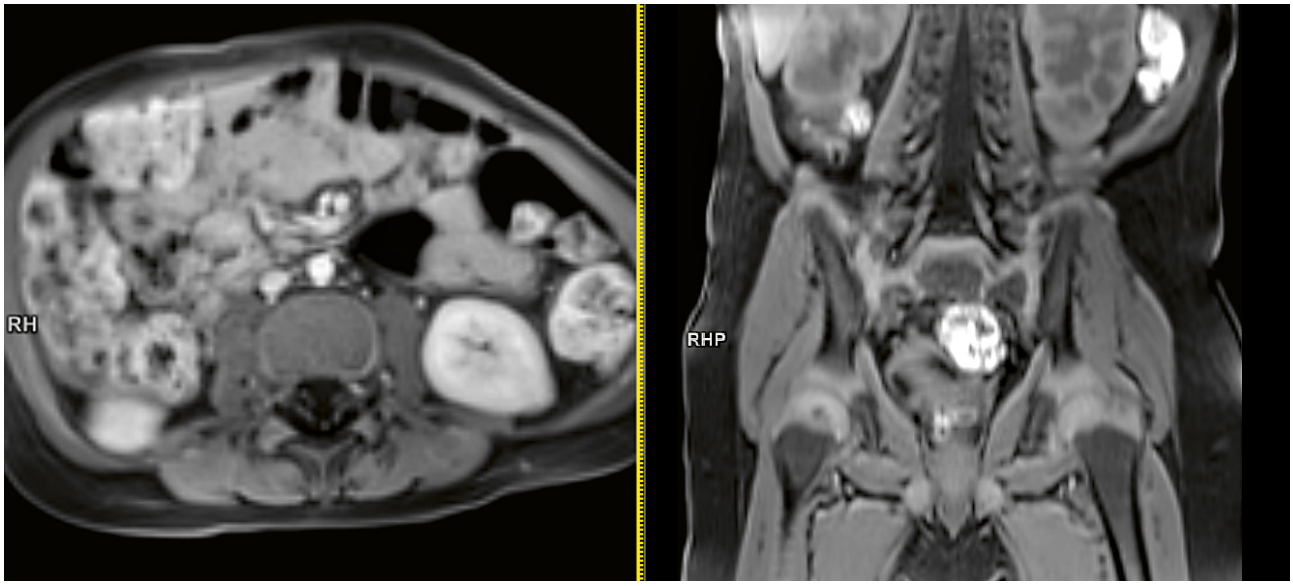

16 Axial T1 StarVIBE 1 mm slice and coronal reconstructed T1 StarVIBE: no intra-abdominal testis just below the right kidney, as was initially suggested on the first ultrasound.

In conclusion, MAGNETOM Sola and the pediatric coil team up very well to provide pediatric patients with the care they are entitled to.

Contact

Johan Dehem, M.D.
Jan Yperman Ziekenhuis
Briekestraat 12
8900 Ypres
Belgium
Phone: +32 57 35 74 00
johan.dehem@yperman.net

Small Structures Big Challenges: Fetal Cardiac Magnetic Resonance Imaging

Veronica Bianchi[1]; Jérôme Yerly[1,2]; Jerome Chaptinel[1]; Yvan Mivelaz[3]; Milan Prsa[3]; Leonor Alamo[1]; Chantal Rohner[1]; Jean-Baptiste Ledoux[1,2]; Davide Piccini[1,5]; Chris Roy[1]; Matthias Stuber[1,2]

[1] Department of Radiology, University Hospital (CHUV) and University of Lausanne (UNIL), Lausanne, Switzerland
[2] Center for Biomedical Imaging (CIBM), Lausanne, Switzerland
[3] Department of Pediatrics, University Hospital (CHUV) and University of Lausanne (UNIL), Lausanne, Switzerland
[4] Department of Gynecology-Obstetrics, University Hospital (CHUV) and University of Lausanne (UNIL), Lausanne, Switzerland
[5] Advanced Clinical Imaging Technology, Siemens Healthineers, Lausanne, Switzerland

Introduction

Congenital heart disease (CHD) is the most common birth defect affecting nearly 1% of pregnancies in Europe [1, 2]. Gestational screening has greatly improved antenatal diagnosis of heart malformations and several prenatal interventions now exist to treat CHD in utero, or soon after birth. The timing and type of treatment relies heavily on the ability to accurately visualize a given cardiac malformation. Echocardiography is the gold standard for fetal cardiac imaging [3]. This imaging technique is safe and non-invasive but, despite the progress made in the field of fetal ultrasonography, its quality varies in the presence of maternal obesity, oligohydramnios, multiple gestations, or imaging during late gestation, among other conditions [4]. Since its early applications [5], cardiac magnetic resonance imaging (MRI) has been increasingly investigated for fetal[1] heart imaging in the last decade and has now become an active area of research. A growing number of studies are exploring its applicability in the evaluation of cardiac morphology and function for both normal and abnormal hearts [6–13]. Despite encouraging advances, there remain significant challenges for fetal cardiac MRI, including the small size and the high rate of the fetal heart, the absence of a conventional fetal cardiac gating signal, and the numerous sources of motion artifacts, such as gross fetal movement, and maternal respiration [4]. However, if these challenges can be addressed, it has been shown that MRI has the potential to provide complementary information to echocardiography, improve our ability to monitor CHD diagnosed *in* utero, and better help guide treatments and decision making.

The aim of this project was to develop an MR image acquisition and reconstruction framework that can overcome the aforementioned challenges and visualize the fetal heart with high spatial and temporal resolution [8]. In this article, we describe such an approach, which combines maternal breath-hold, compressed sensing, and self-gating to produce high quality CINE images of the fetal heart. In addition, here we show preliminary results using our reconstruction framework to produce high quality CINE images of the fetal heart. For comparison, we include ultrasound images in the same orientation of those acquired with MR.

Image reconstruction framework

Our reconstruction framework for golden angle radial acquisitions is composed of three main steps. First, intermediate low-resolution images are reconstructed using compressed sensing. Second, an ECG-like self-gating signal is extracted from the intermediate images. Third, the acquired data are reordered into the identified cardiac phases (Fig. 1) [8].

Initially, low spatial and temporal resolution images are reconstructed with a sliding window approach using 15 radial readouts per window and 70% view-sharing, leading to a temporal resolution of 18.5 ms (Fig. 1B). Subsequently, the obtained images are analyzed off-line with a custom-built semi-automatic tool in MATLAB[2] (MathWorks, Natick, MA, USA). The gating signal that reproduces the contraction cycles of the fetal heart is computed by cross-correlating each intermediate frame to a diastolic and a systolic reference image, focusing on a region of interest circumscribed around the fetal heart (Fig. 1C). Finally, and owing to the characteristics that the golden angle acquisition scheme is providing us with,

[1] *Siemens Healthineers disclaimer does not represent the opinion of the authors: MR scanning has not been established as safe for imaging fetuses and infants less than two years of age. The responsible physician must evaluate the benefits of the MR examination compared to those of other imaging procedures.*

[2] *The information shown herein refers to products of 3rd party manufacturers and thus are in their regulatory responsibility. Please contact the 3rd party manufacturer for further information.*

the radial readouts are retrospectively binned into different cardiac phases (Fig. 1D) with a bin width of 25 ms and a view-sharing equal to 50%, improving the temporal resolution to 12.5 ms. Both intermediate and retro-gated images are reconstructed using an in-house script implementing a *k-t* sparse SENSE algorithm model [14].

Image acquisition and analysis

To validate the proposed framework, six pregnant patients (gestational age 29.7 ± 2.1 weeks at the time of the MRI exam) with a suspicion of fetal non-cardiac pathology were recruited to undergo both MRI and fetal echocardiography. Written informed consent, according to the recommendations of the local ethics committee, was obtained from all subjects prior to examination.

MR acquisition was performed on a 1.5T clinical MR scanner (MAGNETOM Aera, Siemens Healthcare, Erlangen, Germany) with a 32-channel spine coil and an 18-channel body array coil for signal measurement. Data were collected under maternal breath-hold with a prototype radial golden angle bSSFP sequence (Fig. 1A) and acquisition parameters are summarized in Table 1 [8]. For each patient, three standard views (four-chamber, three-vessel and short-axis view), that are routinely targeted in the clinical fetal echocardiographic examination, were acquired (Fig. 2) in 20.1 s each. Echocardiographic images were acquired on a Voluson E8 Expert or Voluson E10 (GE Healthcare, Waukesha, WI, USA)

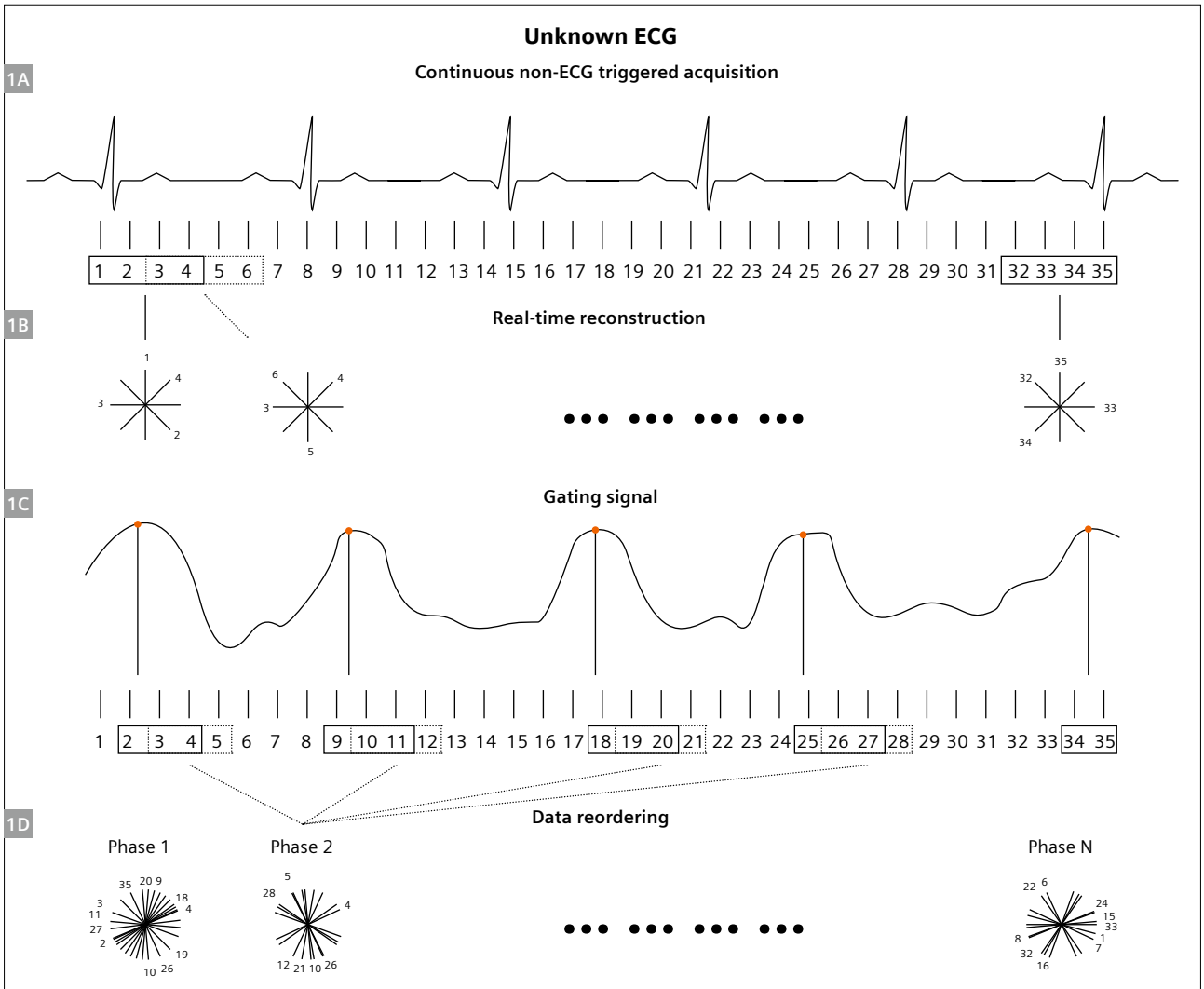

1 Schematic overview of the MRI acquisition and reconstruction framework. The data, acquired with a golden angle continuous acquisition technique **(1A)**, were reconstructed applying a sliding window binning **(1B)** and intermediate images were obtained. The low-resolution images were subsequently analyzed to extract an ECG-like gating signal that represents the contraction cycles of the fetal heart **(1C)**. The self-gating signal was then used to retrospectively bin the radial data in different cardiac phases during which they were acquired **(1D)**. *(Figure adapted from Chaptinel et al. [8], with permission according to https://creativecommons.org/licenses/by/4.0/).*

Parameter	Value
Field-of-view	260 x 260 mm²
Base resolution	256 x 256 pixels
Pixel size	1.0 x 1.0 mm²
Slice thickness	4.0 mm
TE/TR	1.99/4.1 ms
RF excitation angle	70°
Slices	3
Shot per slice	1
Radial readouts per slice	1600
Acquisition time per slice	6.7 s
Bandwidth	1028 Hz/pixel
Reconstructed temporal resolution	12.5 ms (shared phases)

Table 1: Values of the MR acquisition parameters.

with the RM6C 3D/4D curved array transducer with a frequency comprised in the range 1.0–7.0 MHz. Finally, MR and echocardiographic images were qualitatively and quantitatively compared to demonstrate the capability of both imaging techniques to visualize and measure heart structures. Two experienced pediatric cardiologists visually evaluated the quality of the images obtained with both modalities. Subsequently, they measured the diameter of aorta, main pulmonary artery, mitral valve annulus and tricuspid valve annulus using ClearCanvas (Synaptive Medical, Toronto, Canada) on both MR and echocardiographic images for each patient.

Results and discussion

MR images were successfully acquired on all patients. Figure 3 shows an example of fetal heart images in a 4-chamber (Fig. 3A), a short-axis (Fig. 3B) and a three vessel view (Fig. 3C) acquired in a 31-week-old fetus.
MR images (columns on the left) are visually compared to the images obtained with the gold standard, echocar-

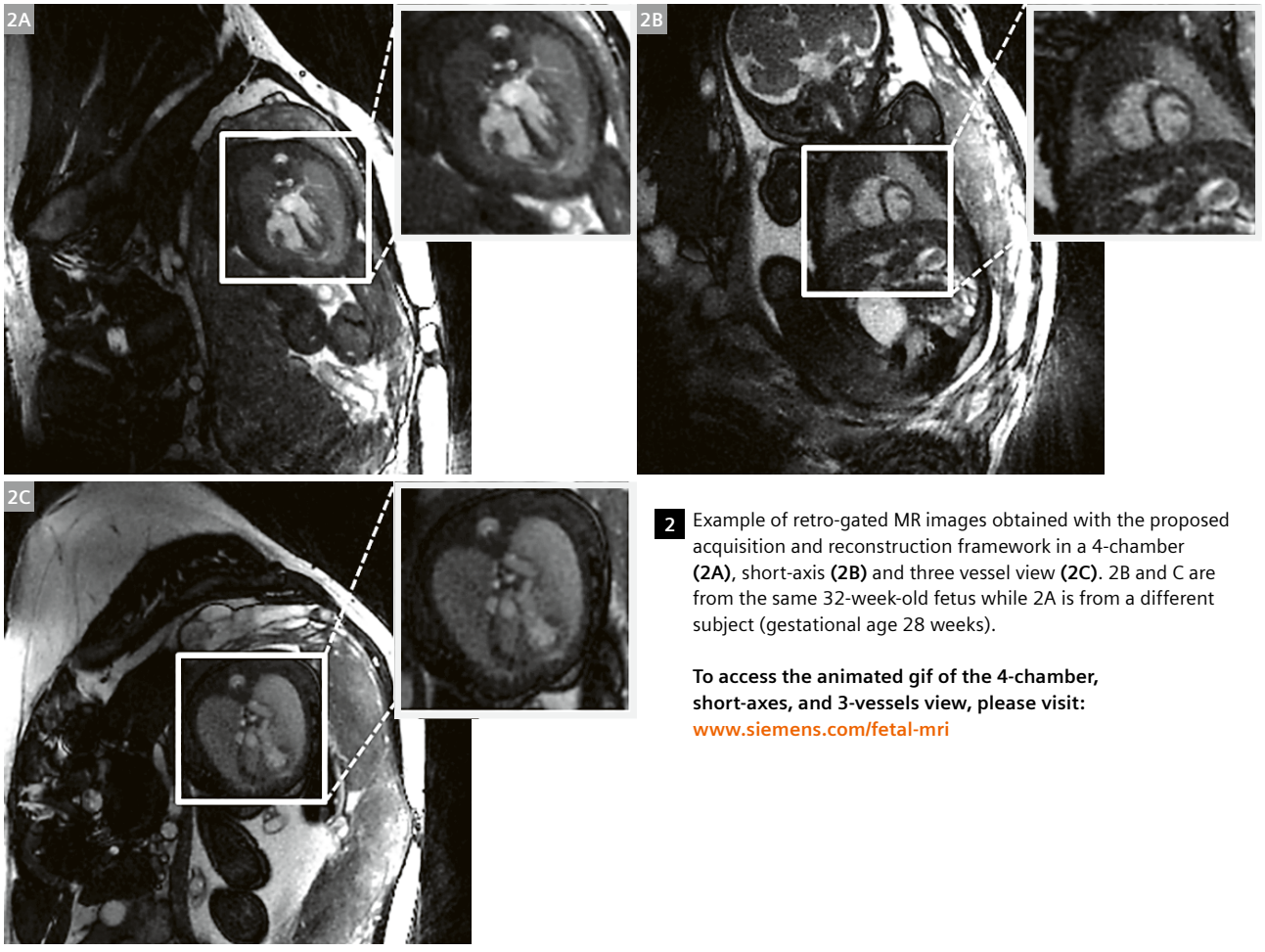

2 Example of retro-gated MR images obtained with the proposed acquisition and reconstruction framework in a 4-chamber **(2A)**, short-axis **(2B)** and three vessel view **(2C)**. 2B and C are from the same 32-week-old fetus while 2A is from a different subject (gestational age 28 weeks).

To access the animated gif of the 4-chamber, short-axes, and 3-vessels view, please visit:
www.siemens.com/fetal-mri

diography (column on the right). The two imaging techniques proved to be comparable in terms of qualitative visualization of cardiac structures. The overall MR image quality was considered satisfying to perform quantitative measurements for all patients except for one in which the mitral valve and the tricuspid valve were not clearly recognizable. Moreover, one patient was excluded from the quantitative comparison because the echocardiographic images were not compatible with the software used for the analysis. Therefore, the diameter of aorta and main pulmonary artery were measured in five patients, while instead mitral valve annulus and tricuspid valve annulus were measured on the images of four patients. As shown in Figure 4, the quantitative measurements performed on the MR images are in good agreement with the measurements by

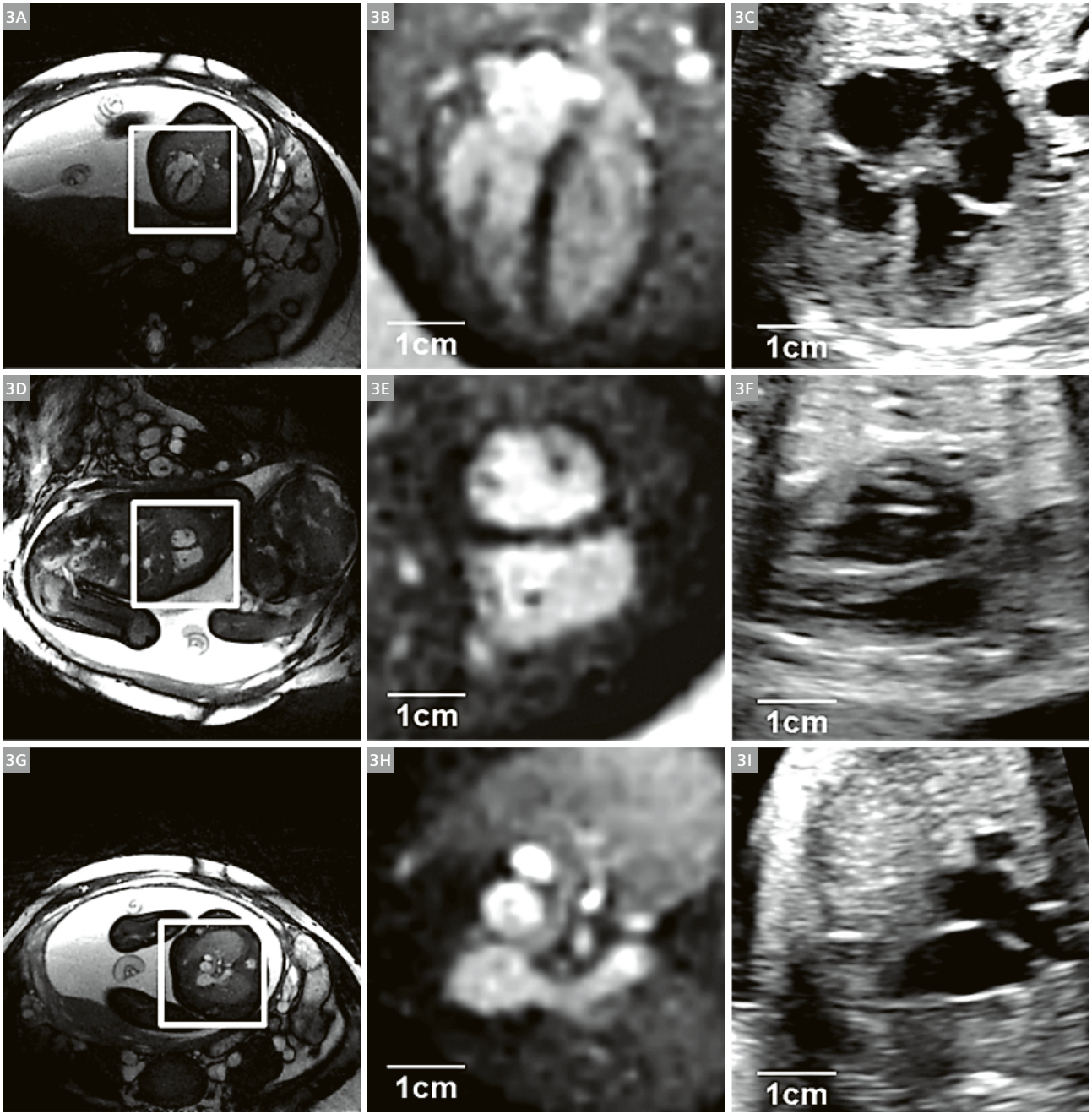

3 Comparison between MR and echo images in 4-chamber **(3A–C)**, short-axis **(3D–F)** and three vessel view **(3G–I)** from one of the patient. *(Figure adapted from Chaptinel et al. [8] with permission according to https://creativecommons.org/licenses/by/4.0/).*

echocardiography. This study demonstrated that MRI is a promising technique for acquiring high spatial and high temporal resolution images of the fetal heart, and that it is critically enabled by advanced acquisition and reconstruction schemes that have recently been developed. These include golden angle acquisition, self-gating that obviates the need for an ECG, and compressed sensing reconstruction. Preliminary results show the potential of our acquisition and reconstruction framework for the visualization and measurement of normal fetal cardiac structures. MRI could offer a reliable easily repeatable and safe complementary imaging modality for patients in whom echocardiography is inconclusive. Further study is now required to assess the diagnostic capability of fetal cardiac MRI in the presence of cardiac abnormalities.

4

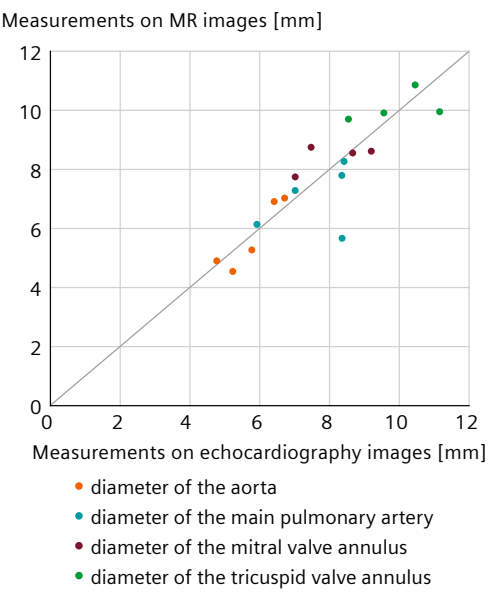

4 Comparison between quantitative measurements performed on MR and echocardiographic images of normal fetal hearts. The graph shows the average values of the measurements performed by two pediatric cardiologists on the best-quality image for each methodology. The diameter of aorta and main pulmonary artery were measured on five fetal patients, while the mitral valve annulus and the tricuspid valve annulus were quantified for four fetal patients.

Contact

Prof. Matthias Stuber
Center for BioMedical Imaging (CIBM)
Centre Hospitalier Universitaire Vaudois (CHUV)
Rue de Bugnon 46, BH 8.80
1011 Lausanne
Switzerland
Matthias.stuber@chuv.ch

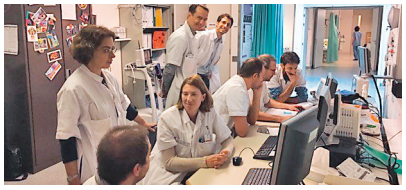

References:

1 Dolk H, Loane M, Garne E, for the European Surveillance of Congenital Anomalies (EUROCAT) Working Group. Congenital heart defects in Europe: prevalence and perinatal mortality, 2000 to 2005. Circulation 2011; 123:841–9.
2 EUROCAT Access Prevalence Tables. Available at: http://www.eurocatnetwork.eu/ACCESSPREVALENCEDATA/PrevalenceTables. Accessed September 11, 2018.
3 Donofrio MT, Moon-Grady AJ, Hornberger LK, et al. Diagnosis and treatment of fetal cardiac disease: A scientific statement from the american heart association. Circulation 2014; 129:2183–2242. doi: 10.1161/01.cir.0000437597.44550.5d.
4 Wielandner A, Mlczoch E, Prayer D, Berger-Kulemann V. Potential of magnetic resonance for imaging the fetal heart. Seminars in fetal & neonatal medicine 2013; 18(5):286-297.
5 Meyer-Wittkopf M, Cook A, McLennan A, Summers P, Sharland GK, Maxwell DJ. Evaluation of three-dimensional ultrasonography and magnetic resonance imaging in assessment of congenital heart anomalies in fetal cardiac specimens. Ultrasound Obstet Gynecol 1996; 8(5):303–8. doi: 10.1046/j.1469-0705.1996.08050303.x.
6 Votino C, Jani J, Damry N, Dessy H, Kang X, Cos T, Divano L, Foulon W, De Mey J, Cannie M. Magnetic resonance imaging in the normal fetal heart and in congenital heart disease. Ultrasound Obstet Gynecol 2012; 39(3):322-329. doi: 10.1002/uog.10061.
7 Manganaro L, Savelli S, Di Maurizio M, et al. Assessment of congenital heart disease (CHD): Is there a role for fetal magnetic resonance imaging (MRI)? Eur J Radiol 2009; 72:172-180. doi: 10.1016/j.ejrad.2008.06.016.
8 Chaptinel J, Yerly J, Mivelaz Y, Prsa M, Alamo L, Vial Y, Berchier G, Rohner C, Gudinchet F Stuber M. Fetal cardiac cine magnetic resonance imaging in utero. Sci Rep 2017; 7(1):15540. doi: 10.1038/s41598-017-15701-1.
9 Gorincour G, Bourliere-Najean B, Bonello B, Fraisse A, Philip N, Potier A, Kreitmann B, Petit P. Feasibility of fetal cardiac magnetic resonance imaging: preliminary experience. Ultrasound Obstet Gynecol 2007; 29:105-108. doi: 10.1002/uog.3924.
10 Tsuritani M, Morita Y, Miyoshi T, Kurosaki K, Yoshimatsu J. Fetal Cardiac Functional Assessment by Fetal Heart Magnetic Resonance Imaging. J Comput Assist Tomogr 2018; 00:00–00. doi: 10.1097/RCT.0000000000000781.
11 Roy CW, Seed M, Kingdom JC, Macgowan CK. Motion compensated cine CMR of the fetal heart using radial undersampling and compressed sensing. J Cardiovasc Magn Reson 2017;19:1–14. doi: 10.1186/s12968-017-0346-6.
12 Amerom JFP, Lloyd DFA, Murgasova K, et al. King's Research Portal Fetal Cardiac Cine Imaging Using Highly Accelerated Dynamic MRI with Retrospective Motion Correction and Outlier Rejection. doi: 10.1002/mrm.26686.
13 Haris K, Hedström E, Bidhult S, et al. Self-gated fetal cardiac MRI with tiny golden angle iGRASP: A feasibility study. J Magn Reson Imaging 2017 doi: 10.1002/jmri.25599.
14 Yerly J, Ginami G, Nordio G, Coristine AJ, Coppo S, Monney P, Stuber M. Coronary endothelial function assessment using self-gated cardiac cine MRI and k-t sparse SENSE. Magn Reson Med 2016; 76:1443–1454. doi: 10.1002/mrm.26050.

Why Siemens Healthineers?

At Siemens Healthineers, our purpose is to enable healthcare providers to increase value by empowering them on their journey toward expanding precision medicine, transforming care delivery, and improving patient experience, all supported by digitalizing healthcare.

An estimated 5 million patients globally benefit from our innovative technologies and services every day in the areas of diagnostic and therapeutic imaging, laboratory diagnostics and molecular medicine, as well as digital health and enterprise services.

We are a leading medical technology company with over 170 years of experience and 18,000 patents globally. With more than 48,000 dedicated colleagues in 75 countries, we will continue to innovate and shape the future of healthcare.

At Siemens Healthineers, our purpose is to enable healthcare providers to increase value by empowering them on their journey toward expanding precision medicine, transforming care delivery, and improving patient experience, all enabled by digitalizing healthcare.

An estimated 5 million patients globally benefit every day from our innovative technologies and services in the areas of diagnostic and therapeutic imaging, laboratory diagnostics, and molecular medicine, as well as digital health and enterprise services.

We are a leading medical technology company with over 170 years of experience and 18,000 patents globally. With more than 48,000 dedicated colleagues in 75 countries, we will continue to innovate and shape the future of healthcare.

The outcomes and statements provided by customers of Siemens Healthineers are unique to each customer's setting. Since there is no "typical" hospital and many variables exist (e.g., hospital size, case mix, and level of service/technology adoption), there can be no guarantee that others will achieve the same results.

On account of certain regional limitations of sales rights and service availability, we cannot guarantee that all products included in this brochure are available through the Siemens Healthineers sales organization worldwide. Availability and packaging may vary by country and is subject to change without prior notice. Some/All of the features and products described herein may not be available in the United States.

The information in this document contains general technical descriptions of specifications and options as well as standard and optional features, which do not always have to be present in individual cases.

Siemens Healthineers reserves the right to modify the design, packaging, specifications, and options described herein without prior notice. For the most current information, please contact your local sales representative from Siemens Healthineers.

Note: Any technical data contained in this document may vary within defined tolerances. Original images always lose a certain amount of detail when reproduced.

Siemens Healthineers Headquarters
Siemens Healthcare GmbH
Henkestr. 127
91052 Erlangen, Germany
Phone: +49 9131 84-0
siemens-healthineers.com

USA
Siemens Medical Solutions USA, Inc.
Healthcare
40 Liberty Boulevard
Malvern, PA 19355-9998, USA
Phone: +1-888-826-9702
siemens-healthineers.us

Published by Siemens Medical Solutions USA, Inc. · Order No. MR-19-2502 · Printed in USA · 09.2019 ·